5-2011

Atomistic Modeling of Hydrogen Storage in Nanostructured Carbons

Lujian Peng
Materials Science and Engineering Department, lpeng@utk.edu

To the Graduate Council:

I am submitting herewith a dissertation written by Lujian Peng entitled "Atomistic Modeling of Hydrogen Storage in Nanostructured Carbons." I have examined the final electronic copy of this dissertation for form and content and recommend that it be accepted in partial fulfillment of the requirements for the degree of Doctor of Philosophy, with a major in Materials Science and Engineering.

James R. Morris, Major Professor

We have read this dissertation and recommend its acceptance:

James R. Morris, Takeshi Egami, T. G. Nieh, Brian J. Edwards

Accepted for the Council:

Carolyn R. Hodges

Vice Provost and Dean of the Graduate School

(Original signatures are on file with official student records.)

Atomistic Modeling of Hydrogen Storage in Nanostructured Carbons

A Thesis Presented for the
Doctor of Philosophy
Degree
The University of Tennessee, Knoxville

Lujian Peng
May 2011

ACKNOWLEDGEMENTS

I would like to thank my advisor Dr. James R. Morris. This dissertation would not be possible without his guidance and support. I had a fruitful and enjoyable graduate school experience working with him. He is the best advisor I could ever have. I would also like to thank my collaborators: Dr. Cristian I. Contescu, Dr. Nidia C. Gallego, Dr. Takeshi Egami, Dr. Wojtek Dmowski. They provided invaluable experimental data and suggestions for this dissertation. I have learned a lot from the discussions with them. I also gained my first experimental experience due to the invitation from Dr. Cristian I. Contescu and Dr. Nidia C. Gallego. I also would like to give my thanks to my committee members: Dr. T. G. Nieh and Dr. Brian J. Edwards.

Finally, this dissertation is dedicated to my husband, Cong Zhou and my parents, Peng Shaosheng and Chen Kaihua. I am grateful to meet my husband in UTK, who always helps and motivates me in my hardest times. He provided the most important emotional support during pursuing this degree. My parents provided me endless love and support throughout my life. No words can express my gratitude to them.

ABSTRACT

Nanoporous carbons are among the widely studied and promising materials on hydrogen storage for on-board vehicles. However, the nature of nanoporous carbon structures, as well as the relationship between local structure and hydrogen adsorption are still unclear, and hinder the design of carbon materials for optimum hydrogen storage. This dissertation presents a systematic modeling effort of hydrogen storage in nanoporous carbon materials. Tight binding molecular dynamics simulations are utilized to simulate the amorphous carbons over a wide range of density. The resulting structures are in good agreement with experimental data of ultra-microporous carbon (UMC), a wood-based activated carbon, as indicated by a comparison of the microstructure at atomic level, pair distribution function, and pore size distribution. To estimate gas adsorption in complex geometries, an efficient numerical algorithm (based on a continuum gas adsorption model) is developed for calculating the gas uptake at room temperature and moderate pressures. This algorithm is a classical approximation of the quantum mechanical model by Patchkovskii et al.[1] and proven to be much faster than other commonly used methods. The gas adsorption calculations in carbon structures from tight-binding simulations demonstrate both a promising hydrogen storage capacity (1.33 wt% at 298K and 5 MPa) and a reasonable heat of adsorption (12-21 kJ/mol). To our knowledge, this is the first work to directly calculate hydrogen adsorption capacity in amorphous carbon. This work demonstrates that increasing the heat of adsorption does not necessarily increase the hydrogen uptake. In fact, the available adsorption volume is as important as the isosteric heat of adsorption for hydrogen storage in nanoporous carbons.

TABLE OF CONTENTS

Chapter Page

CHAPTER I 1
Introduction 1
CHAPTER II 7
Literature Review 7
2.1 Hydrogen Storage Materials 7
2.2 Amorphous Carbon Structure Modeling 17
2.3 Gas Adsorption Calculation Methods 22
CHAPTER III 27
Continuum Model of Gas Adsorption 27
3.1 Theory 27
3.2 H_2 Adsorption in Expanded Graphite Model 32
3.3 Applications in Other Systems 45
3.4 Method Limitations 61
3.5 Conclusion 69
CHAPTER IV 71
Amorphous Carbon by Tight Binding Simulation 71
4.1 Tight Binding Simulation Program Development 72
4.2 Amorphous Carbon Structure Analysis 82
4.3 Conclusion 102
CHAPTER V 103
Hydrogen Adsorption in Amorphous Carbons 103
CHAPTER VI 114
Summary and Future Work 114
LIST OF REFERENCES 121
Vita 127

LIST OF TABLES

Table Page

Table 1.1 Table 1.1 Technical targets of on-board hydrogen storage for light-duty vehicles 3
Table 3.1 Results for hydrogen adsorption in amorphous carbons 53
Table 3.2 The values of K_{eq} as a function of box size, calculated using the approach of Patchkovskii, and the comparisons between K_{eq} and $\exp(-E_{ads}/k_BT)$ at T=298K. E_{ads} is set as -0.10 eV 68
Table 4.1 Coefficients of the polynomial functions $t_s(r-r_1)$, $t_\varphi(r-d_1)$, and f(x) 76
Table 4.2 The mean coordination N as a function of carbon bulk density for different quenching rate (0.1 and 0.5 K/fs) 92

LIST OF FIGURES

Figure Page

Figure 3.1 (upper) The adsorption energy of a single H2 molecule between two expanded graphene sheets calculated using the Wang et al. and Patchkovskii et al. potentials, respectively. (bottom) H2 density profile between two expanded graphene sheets, calculated using the Patchkovskii et al. potential at 298K and 5MPa. 34
Figure 3.3 Virial graphs for the adsorption of hydrogen between two graphite layers with 6 Å spacing at four temperatures. (260 K to 350 K)..... 40
Figure 3.4 The variation of A_0 with $1/T$ for hydrogen adsorption between two graphite layers with 6 Å spacing..... 41
Figure 3.5 The variation of isosteric heat (q_{st}) with hydrogen uptake between two graphite layers with 6 Å spacing at different temperatures. (250 K to 333 K)..... 44
Figure 3.6 A portion of the simulated amorphous carbon structure (gray) with density of 1.25 g/cm3 and the positions with adsorption energy less than –0.1 eV/molecule. The positions are colored by the adsorption energies from red (high energy) to blue (low energy). 49
Figure 3.7 The total H_2 adsorption (top) and available adsorption volume (bottom) in amorphous carbons as a function of carbon density at 298K and 5 MPa. 52
Figure 3.8 Eight optimal structures for a single hydrogen molecule adsorbing on ZnO sheet [99]. The left panels are the top view, and the right panels are the side views. Binding energy and the distance between the plane and the center of H_2 are denoted in the figure..... 56
Figure 3.9 The desorption energy curve of one hydrogen molecule desorbed from ZnO sheet [99]..... 58
Figure 3.10 The density contours for several fractions of the de Broglie density $\rho_0 \equiv 1/\Lambda^3$ (which sets the density scale at which quantum effects are expected to become important)..... 65
Figure 4.1 The potential energy per atom calculated as function of nearest neighbor distance in linear chain, graphite, diamond and simple cubic carbon. 77
Figure 4.2 Performance speed up vs. number of processors in ScaLAPACK compared to LAPACK in matrix of size 8196x8196. 81
Figure 4.3 Atomistic pictures of the amorphous carbon structures with density of 0.6 - 2.4 g/cm3..... 85
Figure 4.4 The pair distribution functions of simulations (a)-(f) included in Figure 4.3. The experimental data (red) is from the X-ray diffraction of UMC.[126] 88
Figure 4.5 The portion of 1-fold, 2-fold, 3-fold, and 4-fold bonded atoms as a function of bulk density for temperatures near T =300K with (a) quenching rate of 0.1 K/fs and (b) quenching rate of 0.5 K/fs..... 90
Figure 4.6 The averaged potential energy as a function of bulk density for temperatures near T=300K. 93
Figure 4.7 The potential energy as a function of fraction of three-fold bonded atoms in the simulations. 95

Figure 4.8 (a) Pore size distribution function of simulated structures with bulk density of 1.8g/cm3(red) compared experimental measurement of UMC 97
Figure 4.9 (a) Illustration of isolated pores in amorphous carbon structures. 99
Figure 4.10 Skeletal density as a function of bulk density with different quenching rates (black triangles: 0.1K/fs; red circles: 0.5K/fs). 101
Figure 5.1 Demonstration of adsorption sites in amorphous carbon structures..... 107
Figure 5.2 (a) Total hydrogen uptake, (b) available adsorption volume, and (d) excess adsorption as a function of carbon bulk density at T=298K and P=5MPa 108

CHAPTER I

INTRODUCTION

The current energy economy, based on fossil fuels, is not sustainable because the supplies of crude oil, coal, and natural gas are not replenished as they are consumed. Hydrogen, as one of the most abundant elements on earth, contains about three times the energy density per mass of petroleum. Delivering energy using hydrogen would reduce the dependence on fossil fuels and decrease pollution to the environment. Hydrogen has been promoted as a potential fuel for automotive power and as an alternative, non-toxic energy storage method. A future economy based on hydrogen is envisioned to be clean, flexible, and abundant. However, the development of a hydrogen economy depends on overcoming numerous scientific and technological obstacles, including hydrogen production, hydrogen storage and hydrogen usage. Based on the needs of transportation, hydrogen storage must meet the following requirements for effective hydrogen-powered vehicles: (i) favorable enthalpies of hydrogen adsorption and desorption; (ii) fast kinetics for adsorption and desorption; (iii) high gravimetric and volumetric densities; (iv) long cycle life time for hydrogen absorption/desorption; (v) high mechanical strength and durability; (vi) safety under normal use, and acceptable risk under abnormal conditions. In particular, the U.S. Department of Energy (DOE) has proposed specific performance targets for successful hydrogen storage technologies (Table 1). For example, to drive a regular vehicle for a range of 480 km, 4 kg hydrogen is needed. This amount of hydrogen occupies a volume of over 50,000 L at ambient conditions. For 2015, the

Department of Energy (DOE) gravimetric target for hydrogen storage is 5.5 wt% and the volumetric target is 4.0 g/L at room temperature and pressures less than 12 bars. The storage efficiency is evaluated using the volume and weight of the entire storage system including tank, insulation, coolants etc. Possible approaches for hydrogen storage include liquefaction or compression of hydrogen gas, chemical storage by chemical or metal hydrides, and physisorption in solid materials. Although different approaches have different advantages and some of the requirements have been met, none of the current approaches satisfy all the DOE specifications for transportation applications.

Table 1.1 Technical targets of on-board hydrogen storage for light-duty vehicles (http://www1.eere.energy.gov/hydrogenandfuelcells/storage/pdfs/targets_onboard_hydro_storage.pdf).

Storage Parameter	Units	2010	2015	Ultimate
System Gravimetric Capacity				
Usable, specific-energy from H_2	kWh/kg	1.5	1.8	2.5
(net useful energy / max system mass) [a]	(kg H_2/kg system)	(0.045)	(0.055)	(0.075)
System Volumetric Capacity				
Usable energy density from H_2	kWh/L	0.9	1.3	2.3
(net useful energy / max system volume)	(kg H_2/L system)	(0.028)	(0.040)	(0.070)
Storage System Cost [b] (and fuel cost)[c]	$/kWh net ($/kg H_2) $/gge at pump	4* (133) 2-3	2* (67) 2-3	TBD* 2-3
Durability / Operability				
Operating ambient temperature [d]	°C	-30/50 (sun)	-40/60 (sun)	-40/60 (sun)
Min/max delivery temperature	°C	-40/85	-40/85	-40/85
Cycle life (1/4 tank to full) [e]	Cycles	1000	1500	1500
Cycle life variation [f]	% of mean (min) at % confidence	90/90	99/90	99/90
Min delivery pressure from storage system; FC = fuel cell, ICE = internal combustion engine	Atm (abs)	4FC / 35 ICE	3FC / 35 ICE	3FC / 35 ICE
Max delivery pressure from storage system [g]	Atm (abs)	100	100	100
Charging / Discharging Rates				
System fill time (for 5 kg H_2)	min (Kg H_2/min)	4.2 min (1.2 kg/min)	3.3 min (1.5 kg/min)	2.5 min (2.0 kg/min)
Minimum full flow rate	(g/s)/kW	0.02	0.02	0.02
Start time to full flow (20 °C) [h]	s	5	5	5
Start time to full flow (-20 °C) [h]	s	15	15	15
Transient response 10%-90% and 90% - 0% [i]	s	0.75	0.75	0.75
Fuel Purity (H_2 from storage) [j]	% H_2	99.99 (dry basis)		
Environmental Health & Safety				
Permeation and leakage [k]	Scc/h	Meets or exceeds applicable standards		
Toxicity	-			
Safety	-			
Loss of useable H_2 [L]	(g/h)/kg H_2 stored	0.1	0.05	0.05

*The storage system costs are currently under review and will be changed at a future date.
Useful constants: 0.2778kWh/MJ, ~33.3kWh/gal gasoline equivalent.

This dissertation aims to present a systematic study of hydrogen storage in nanoporous carbon materials. Carbon is among the most extensively investigated materials for hydrogen storage applications. However, there still remain many fundamental problems and scientific challenges. Especially, when the relevant dimension of materials controlling storage properties is on the scale of nanometers, unique properties have been discovered and have generated enormous interest in designing carbon nanostructures for energy storage. The confinement of gas molecules in nanoporous carbon materials significantly affects the thermodynamics and kinetics of adsorption. Carbon nanostructures have shown promise for effective hydrogen storage in the past decades. A realistic structural model of amorphous carbon and the underlying nature of hydrogen adsorption in nanometer-scale structures are two key issues for successful design of functional materials for improved hydrogen storage. Fundamental questions such as the effects of surface texture on hydrogen adsorption, the interaction strength between hydrogen and carbon, the diffusion of hydrogen in the disordered structure, and the characterization and modeling of carbon structures need to be answered to assist the breakthroughs in controlling hydrogen uptake and release. This current dissertation tackles the problems related to the structure and hydrogen physisorption in amorphous carbons. The structure of this dissertation is arranged as follows.

Chapter II provides a detailed literature review on current technologies for hydrogen storage, the available approaches for modeling amorphous carbon structures, and the popular methods for gas adsorption calculation. In the first section, concerning hydrogen storage materials, the primary interest is on several forms of carbon materials ranging

from amorphous activated carbon to ordered forms such as carbon nanotubes. This review shows that reversible hydrogen storage capacities of most materials are still less than 1 wt% at room temperature and moderate pressures, far from the DOE targets. The second section reviews various models for amorphous carbons that have been proposed, based on experimental data and computational simulations. Many open questions and discrepancies among theories and experiments are due to the difficulties of experimental characterization and the limitations of current computational capacities. For example, the local and the intermediate atomic arrangements are not clear. Furthermore, precursor materials and production processes affect the final amorphous carbon structures in unknown ways. In the third section concerning gas adsorption calculations, we demonstrate that currently available computational methods are either limited to the applications in simple pore shapes (slit pore and cylindrical geometry) or very computationally expensive. There is a need for more efficient methods for gas uptake calculations in more complex structures (e.g. amorphous carbon).

Chapter III introduces an efficient and accurate numerical method for gas adsorption calculations. We demonstrate that this method reproduces previous, more computationally intensive calculations in the expanded graphite model, yet is readily applicable to more complex geometries. We obtained values of isosteric heat of adsorption in the expanded graphite model that are consistent with experimental values in activated carbons. The limitations of this method are also carefully discussed.

Chapter IV describes the development of realistic models of amorphous carbon structures over a wide range of densities, using a tight binding potential and a quenching molecular dynamics method. High performance parallel tight binding molecular dynamics programs were developed for this purpose. We simulated a relatively large system size, at a lower quenching rate, compared to other similar simulations from the literature. The resulting structures are composed of curved and defective graphene sheets, consistent with microscopic configurations from the experiments. The final porous structures were characterized in terms of pore size distribution, pore connectivity, pair distribution function, and bonding distribution. We also calculated the experimental skeletal density of porous carbon which deviates from the simulation density at low carbon density limit.

Chapter V describes the theoretical hydrogen storage capacity in simulated nanoporous carbon structures at room temperature. The theoretical excess hydrogen uptake was calculated to be up to 1.33 wt% in carbon structures with bulk density of 0.8 g/cm^3 at 298 K and 5 MPa. The isosteric heat of adsorption was calculated between 12 kJ/mol and 21 kJ/mol, suggesting that amorphous carbon may be promising for hydrogen storage. Hydrogen uptake was shown to be correlated with the micropore volume in addition to the isosteric heat of adsorption. Especially, increasing the isosteric heat of adsorption does not necessary increases the hydrogen uptake, which contradicts normal assumptions.

Future work and perspectives are discussed in Chapter VI.

CHAPTER II

LITERATURE REVIEW

2.1 Hydrogen Storage Materials

In this section, we describe the current research into hydrogen storage methods as well as the fundamental problems needed to be solved before achieving the hydrogen storage goals. Safety is always the first priority in hydrogen transportation and utilization due to the high flammability and risk of leaking of hydrogen. Reducing the cost and making the price of hydrogen competitive with current fossil fuels is the key issue for achieving hydrogen economy. Nowadays storing hydrogen in a high pressure tank is the most mature technology but requires pressure much higher than 10,000 psi to compensate for the low energy density per volume of hydrogen gas at room temperature. The heavy compression devices and containers will quickly decrease the system's hydrogen gravimetric density of hydrogen storage. Research on strong, reliable and light weight materials for high pressure tanks is needed. The embrittlement of hydrogen to metals should also be considered to ensure the safe operation. Improvements of hydrogen storage have been made by combining high pressure and cryogenic technologies. At lower temperatures, more hydrogen can be stored as a liquid at a given volume, compared to being stored in gas phase. However, the biggest drawback is that a large amount of energy is lost during the compression and liquefaction of gas. The DOE targets

specifically require that hydrogen storage for on board vehicles should operate at near ambient conditions, ruling out the options using high pressure or cryogenic tanks. Thus, this review only focuses on hydrogen storage in solid materials by chemical adsorption and physisorption. Detailed discussions are provided concerning the present state of studies of hydrogen storage in carbon materials.

2.1.1 Metal hydrides

Metal hydrides are important materials for energy storage through chemical adsorption. They are usually classified into classical metal hydrides and light metal complex hydrides. Classical metal hydrides are intermetallics of AB_2, A_2B, AB, and AB_5 forms, where A is usually a lanthanide element and B is Ni, Co, Al, Mn, Fe, etc. The hydrogen is stored interstitially in the lattice of the heavy atoms. Classical metal hydrides suffers from high desorption temperatures and large weight penalties with hydrogen storage capacity mostly less than 2 wt%. The work of Bogdanovic and Schwickardi [2] have sparked significant research into light metal complex hydrides such as alanates, borohydrides and amides. Alanates containing $[AlH_4]^-$ have received much attention due to their commercial availability and high hydrogen gravimetric contents. For example, the hydrogen gravimetric density in $LiAlH_4$ is 10.54 wt% and $Mg(AlH_4)_2$ is 9.27 wt%. [3] It should be noted that these values are the amount of hydrogen stored, instead of the amount released by the materials. Usually, the reversibly stored hydrogen amount is less than the maximum capacity. Due to the endothermic nature of dehydrogenation reactions, a high temperature range (usually greater than 200^{o}C) is required for

dehydrogenation. Due to the strong chemical bonding between metals and hydrogen atoms, high kinetic barriers to dehydrogenation impede the potential applications of metal hydrides on practical hydrogen storage. Recently, $NaAlH_4$ has been most intensively studied for hydrogen storage and considered as a plausible candidate for practical transportation applications. Doping $NaAlH_4$ with titanium was found to significantly increase the kinetics of dehydrogenation and lower the first decomposition temperature to 150°C.[2, 4] Further research found that Sc-doped $NaAlH_4$ achieved faster kinetics of dehydrogenation. However, it is not practical to dope Sc for commercial hydrogen storage since Sc is expensive. Impurities in hydrogen gas, including O_2 and water, will dramatically hamper the reversibility of metal hydrides. Balde et al.[5] found that by decreasing the particle size of $NaAlH_4$ to 2-10 nm, the hydrogen desorption temperature was lowered to 70°C, and the activation energy was decreased to 58 kJ/mol. Although great developments have been obtained in metal hydrides research, they are still short of the DOE targets due to high dehydrogenation temperature, high reaction pressure, cycling stability, and relatively low gravimetric density.

2.2.2 Zeolites

Physisorption in solid materials is another important method for hydrogen storage. In contrast to chemical adsorption in metal hydrides, physisorption relies on weak dispersive forces which usually result in low hydrogen uptake at room temperature. Cryogenic conditions are usually employed to achieve considerable hydrogen uptake. Zeolites are important industrial applicable materials for gas separation and water purification. They are microporous aluminosilicate materials with high internal surface areas and open

channels with nanoscale diameters (less than 10 nm). Zeolites have been of interest for the physisorption of hydrogen both experimentally and theoretically. One of the major advantages of zeolites is that they are easy to prepare compared to novel nanomaterials such as carbon nanotubes. Over 170 different structures of zeolites have been discovered or synthesized. Early research focused on the high temperature and high pressure hydrogen adsorption behaviors in zeolites because the hydrogen molecules can enter certain zeolite cages under elevated temperatures and pressures. However, the amount of hydrogen trapped in zeolite cages is very low at these conditions. For example, CsA[6] can encapsulate 0.6wt% hydrogen when loading at 300 ^{o}C and 917 bar. Lower temperatures provide higher hydrogen uptake in zeolites. Due to the heavy atomic constituents in zeolites, the gravimetric density is still much lower than the DOE targets. It was reported that the zeolite Na-LEV had hydrogen storage capacity up to 2.07 wt% at 77K, 1.6 MPa.[7] For room temperature adsorption, Chung[8] reported 0.4 wt% hydrogen storage at 30 ^{o}C and 50 bar in the ultra stable Y (USY) zeolite. Many results suggested that the saturated value of hydrogen adsorption depended mainly on the BET surface area and pore volume of zeolites.[8] To improve the hydrogen storage capacity, the major challenge is how to enhance the energy of interaction of hydrogen with zeolites. This might be achieved by introducing guest materials into the frameworks[9].

2.3 Metal-organic framework materials

Metal-organic framework (MOF) materials have been proposed as a candidate for hydrogen storage in recent years and quickly evoked enormous enthusiasm amongst

researchers. MOF are crystalline materials that combine metal-organic complexes with organic linkers to create three dimensional porous structures. The pore size and connectivity can be designed and controlled by carefully selecting metal clusters and organic groups.[10] The surface areas of MOF materials are very large (up to 10400 m^2/g)[11] suggesting their applicability for gas adsorption. High hydrogen storage capacities were reported at cryogenic temperature and high pressure conditions. The adsorptions at ambient temperature are much lower due to the low adsorption enthalpy. For example, Rosi et. al[12] found the maximum hydrogen uptake in MOF-5 of composition $Zn_4O(BDC)_3$ was 4.5 wt% at 78K and 1.0 wt% at room temperature and pressure of 20bar. Kaye et al.[13] further reported a total hydrogen uptake up to 11.9 wt% in MOF-5 at 77 K and 170 bar and 1.4 wt% at room temperature and 90 bar. Theoretical[14-15] and experimental[12, 16] studies both indicated that the metal-oxide cluster was mainly responsible for the hydrogen adsorption while the organic linker played a secondary role. The measured adsorption enthalpy was between 4 to10 kJ/mol[17], consistent with theoretical calculations.[18-19] Enhancing the interaction between hydrogen molecules and exposed metal atoms such as Cu^{2+}, Ni^{2+}, Mn^{2+} is one of the most promising strategies to increase hydrogen uptake at room temperature. A high isosteric heat of hydrogen adsorption of 12.3 kJ/mol was reported in $Zn_3(BDC)_3$[Cu(pyen)] containing unsaturated Cu^{2+}.[20] The current challenge is to develop synthetic methods to create a high concentration of dispersed coordinative unsaturated metal centers in the frameworks. Another method to increase hydrogen adsorption is to control the pore size and surface area of MOF materials. Very large pore sizes are detrimental to both the volumetric and gravimetric densities since the hydrogen molecules in the center of large

pores are mainly compressed by high external pressure instead of adsorbed by the potential energy of pore walls. Appropriately sized small pores will adsorb hydrogen more strongly and induce more surface areas. A spillover mechanism was proposed to explain the improved storage capacity of the mixture of MOFs and Pt/C catalyst.[21] However, many fundamental problems of spillover need to be understood before further materials design can follow this direction. Significant advances in MOF research are still needed to meet the DOE targets for hydrogen storage.

2.4 Carbon Materials

Carbon materials have been intensively studied for hydrogen storage due to their light weight, high surface area, and tunable pore size. Nanoporous carbons are also of great interest in other applications such as gas separation, catalysts, supercapacitors and anode in Li ion batteries. Different types of carbon structures have been investigated for hydrogen adsorption, including graphite nanofibers, single walled and multi-walled carbon nanotubes, fullerenes, and activated carbons. Early work reported an extraordinarily high hydrogen uptake up to 67 wt% at room temperature and spawned numerous similar studies.[22-25] Unfortunately, most of these values were controversial and irreproducible. Later studies revealed that the remarkable values of hydrogen uptake were due to the experimental errors or impurities in the H_2 gas. Recent studies from experiments and theories have reported scattered adsorption values for different carbon structures.

Graphite nanofibers (GNF) are a type of engineered material consisting stacks of graphene plates. GNFs have different distinct microstructures including tubular, platelet and herringbone structures, depending on the angle between the direction of the nanofiber axis and the vector normal to the graphite plates. The distance between graphene plates is the same (3.37Å) as in conventional graphite. The unique structures of GNF provide relatively high surface area and active interaction sites on the edge of the fibers. Chambers et al.[22] reported 67 wt% hydrogen uptake in GNF at room temperature and 11.35 MPa. Such a high value would require five layers of hydrogen molecules between two graphite sheets with a nearest neighbor distance of 0.98 Å.[26] More careful experiments showed that the hydrogen adsorption in GNFs at room temperature was typically very low (<0.3 wt%).[27] Theoretical calculations predicted the hydrogen adsorption between graphite sheets could be up to 3 wt% at room temperature, but only after the interlayer spacing was expanded to 7 Å. [1, 28-30]

Carbon nanotubes are formed from rolled graphite sheets with diameters from 0.7 nm up to several nm and lengths of 10-100 micrometers. The tubes formed by a single graphite sheet are called single walled carbon nanotubes (SWNT), while those consisting of multiple graphite sheets are called multi-walled carbon nanotubes (MWNT). Carbon nanotubes tend to form closed-packed bundles and the intertube distance is close to 3.34 Å. The measured surface areas were measured from 37 to 1190 m^2/g.[27, 31] Compared to open flat graphite sheets, the curvature of carbon nanotubes increase the attractive forces to hydrogen molecules due to the overlap of potential from the opposite walls.[32] It has been shown that the hydrogen molecules were likely adsorbed in the internal channel

between nanotubes and the groove of nanotube bundles.[33] Chen et al. [24] reported up to 20 wt% hydrogen adsorption in Li and K doped nanotubes at room temperature and 1 atm, which was later proven to be due to the water present in the hydrogen gas. Much lower experimental values were reported ranging between 0.3 to 2.4 wt% in SWNT and MWNT at room temperature and 10 MPa.[31, 34-35] Zuttel et al. [31] used an electrochemical method to measure the hydrogen desorption capacity in SWNT and found the desorption capacity linearly correlated to the BET specific surface area. At cryogenic temperatures, a much higher hydrogen adsorption was observed.[35-36] For example, Ning et al.[37] reported a hydrogen uptake of 2.27 wt% at 77K and 10.3 MPa in MWNTs with very high purity. Using highly purified SWNTs, Ye et al. obtained more than 8 wt% hydrogen uptake at 80 K and less than 120 bar.[36] In theoretical calculations, Kowalczyk et al. used grand canonical Monte Carlo simulations to model the hydrogen storage in various nanoporous carbons at room temperature and 77 K.[38] They obtained 1.4 wt% at 77K and 1 atm in SWNTs. They attributed the discrepancy between simulations and experiments to the polydispersity of the diameters of the nanotubes in experiments and the impurities in the real bundles of SWNT. Deng et al.[39] employed grand canonical Monte Carlo simulations with a first principle derived force field to calculate the H_2 storage in Li-doped pillared graphene and SWNT. Up to 6.5 wt% reversible hydrogen adsorption was reported in graphene sheets at 20 bars and room temperature. A hydrogen storage capacity of 6.0 wt% and 61.7 kg/m^3 was found in SWNT according to their calculations at room temperature and 50 bars, close to the DOE targets. More recent work by Dimitrakakis et al.[40] constructed novel 3-D structures with parallel graphenes which were stabilized by carbon nanotubes placed vertically to the graphene planes. These structures

were doped with Li cations for enhancement of hydrogen storage. By the first principle calculations and GCMC simulations, the hydrogen adsorption is close to 7 wt% at room temperature and 100 bars, achieving DOE targets. Despite the high adsorption values from simulations, most experimental results are still much lower than DOE targets. One reason of the discrepancy is that different experimental groups used the carbon nanotube samples with different. Another reason is the difficulty for theory to reliably determine the adsorption potential. Progresses need to be made in many directions in the future, including in experiment, concept, and simulation.

Fullerenes are a class of carbon molecules where carbon atoms arranged into 12 pentagonal faces and 2 or more hexagonal faces. Similar to carbon nanotubes, fullerenes are composed of graphene sheets with hexagonal rings but they also contain pentagons or heptagons to form non-planar structures. Fullerenes can take the form of hollow spheres, ellipsoid or tube. Spherical fullerenes are called buckyballs with common structures of C_{60}, C_{70} et al. Fullerenes are produced by slowly condensing the vaporized mixture of carbon and inert gas without metal catalysts. The chemical and physical properties of fullerenes have been popular topics for the past two decades, including hydrogen storage applications. The hydrogen is usually chemically adsorbed to fullerenes. $C_{60}H_{36}$ is the most abundant hydrofulleride and is of interest as high capacity hydrogen storage material. Theoretically calculations[41] showed that the heat of formation of $C_{60}H_{36}$ was lower than that of C_{60}, indicating that $C_{60}H_{36}$ was more thermodynamically favored. Peera et al.[41] studied the dehydrogenation behavior of $C_{60}H_{36}$ and found hydrogen could be thermally removed at 500 ^{o}C. Komatsu et al.[42] introduced a molecular surgical

process to synthesize C_{60} encapsulating molecular hydrogen inside. This can be viewed as new method to store and deliver hydrogen. However, the endohedral fullerene is very stable and the encapsulated H_2 does not escape even when heated at 500 ^{o}C for 10 min.

Activated carbon is a form of carbon with amorphous structures and very large surface area available for adsorption and chemical reactions. Activated carbons are produced from raw materials such as coal, coconut shells, wood, peat, and petroleum based residues. These carbon-rich organic precursors are processed by dry distillation followed by thermal or chemical treatments to increase the pore volume and surface area. Their surface area can be larger than 3300 m^2/g. The pore sizes in activated carbons are usually categorized by micropores (<20 Å), mesopores (20 - 500 Å), and macropores (>500Å). The raw materials and processing methods both affect the pore size distribution. In general, the macropoores and mesopores do not play a large role in gas adsorption. It is the micropours structure in activated carbon that is effective for adsorption. The hydrogen storage capacities of activated carbon reported by different measurements are rather consistent[43-45], and the data is less varied than those for carbon nanotubes. The general trend is that the hydrogen adsorption increases with increasing pressure and decreasing temperature. The hydrogen storage capacity has been correlated with surface area as well as the micropore volume.[35, 46] Jorda-Beneyto et al.[46] carried out hydrogen adsorption measurements at high pressures in various activated carbons. The best values of total uptake at 298K were 3.2wt% for 20MPa and 6.8wt% for 50MPa. By comparing the hydrogen storage capacities of various carbon materials, including activated carbon, SWNT and graphite carbon nanofibers, Xu et al. [27] reported that the highest hydrogen

adsorption was 0.67 wt% at 303K, 10MPa and 5.7 wt% at 77K, 3 MPa in a super activated carbon. Burress et al.[47] reported the hydrogen storage capacity up to 1.8 wt% at room temperature, 80 bar and 9.1 wt% at 77K, 50bar in corncob-based nanoporous carbons. By applying the Langmuir isotherm model, Burress et al.[47] obtained good agreements between hydrogen adsorption experiments and calculations while assuming localized adsorption at 77K and mobile adsorption at 303K. The hydrogen binding energies were calculated to be between 4.8 kJ/mol and 8.0 kJ/mol by fitting the experimental data with a simple two binding energy model. Recently, Bhat et al.[48] reported high levels of hydrogen uptake of 0.8 wt% in a type of activated carbon (ultramicroporous carbons (UMC)) at 25 ^{o}C and 2 MPa. The current state of study shows the promise of activated carbon for hydrogen storage. Further improvements in storage capacity and fast adsorption/desorption kinetics will depend on the optimization of activated carbon synthesis and the fundamental understanding of the nature of interaction with hydrogen.

2.2 Amorphous Carbon Structure Modeling

This section reviews the available approaches for modeling amorphous carbon structures. Porous carbons are broadly divided into two groups, graphitizing and non-graphitizing carbons. Graphitizing carbons are characterized by high abundance of aromatic rings per plate with large domain of orientational order. They are weak adsorbents due to the low

degree of microporosity in the structures. Upon heat treatment, graphitizing carbon usually transform to graphite. The activated carbons that we are interested in this dissertation belong to the non-graphitizing carbon category, meaning that they can not be turned to graphite at high temperature. Non-graphitizing carbons exhibit much higher microporous volume and defective carbon plates with smaller regions of orientational order.[49]. Carbonization and activation are two main process steps for preparing activated carbons from organic precursors. Carbonization first converts the raw materials into carbon-containing residues through pyrolysis or destructive distillation. Activation process further enhances the microporosity in these materials by burning away smaller carbon sheets through pyrolysis in a strongly oxidizing environment.[50-51] Depending on the hydrocarbon precursors and the manner of preparation, the type of bonding, hydrogen content, and microporosity of the resulting activated carbon will be different. The local structural details are very important to the properties of activated carbons. For example, in amorphous carbon the atoms are bonded to each other by the hybridization of the outermost s and p orbitals forming sp^3, sp^2, and sp^1 bondings. The carbon density and mechanical properties such as hardness are related to the ratio of different types of bonds and microstructures. However, it is difficult to fully reveal the detailed microstructures of amorphous carbon materials by using traditional structural characterization techniques due to the amorphous nature of activated carbons. Franklin[52] first proposed a simple model that the non-graphitizing carbon consisted of graphite like layers interconnected by non-organized carbons. High resolution scanning transmission electron microscopy and wide-angle X-ray diffractions have revealed small graphene layers and very little correlation between those parallel graphenes sheets.[53] The presence of curvature and the

non-hexagonal rings in the amorphous carbon structures suggest that more sophisticated models are needed. Adsorption studies in activated carbons further indicate very high surface areas and narrow pore size distributions in these structures. It is still a major challenge to construct microstructures of amorphous carbons purely based on experimental information. A realistic model of nanoporous carbon and a fundamental understanding on how the structure texture affects the gas adsorption are of most importance for developing carbon materials for optimum hydrogen storage.

As computer technology is developing quickly, computational simulation has became very important in areas such as engineering, physics, chemistry, biology and materials science. Different modeling approaches have been established for describing the structures of porous carbon materials. The earliest and most commonly used model is the idealized expanded graphite model which consists of two parallel infinite graphene sheets. The main parameter of this model is the distance between the two graphene sheets designed to represent the pore width. The biggest advantage of expanded the graphite model is that it allows a completely theoretical calculation of adsorption and fundamental understanding of confined fluids in micropores. However, this simple model is not suitable to capture the complexity of pore geometry, pore connectivity, the pore size distribution, and the activated adsorption sites on the boundary edges in activated carbon materials. Other simple models keep graphene sheets as the basic building blocks for the structure and allow the graphene sheets to be randomly arranged or even twisted to form ribbon-like networks. However, these models can not explain the stability of non-graphitizing carbons at very high temperature.[49] More models including

collection of fullerene-like fragment have been proposed[54-55] in order to be consistent with the experimental observations. [56]

More advanced methods including reconstruction methods and direct simulation technique have been proposed for better descriptions of activated carbons. Reconstruction methods such as reverse Monte Carlo (RMC) have been used to generate the amorphous carbon structures by fitting the experimental structure factor data from X-ray or neutron diffraction. Starting with randomly placed aromatic carbon plates, Thomson and Gubbins[57] used RMC to generate a model for real carbon structures and analyzed the structural properties as well as the nitrogen adsorption behavior. Further constrained reverse Monte Carlo methods were developed to fix the problems of unrealistic features and nonunique structures in RMC method.[58-59] Jain et al.[59] introduced the hybrid reverse Monte Carlo method (HRMC) which contains an energy constrains term to model saccharose cokes. Hydrogen atoms were taken into account in their models and a very high fraction of two-folded carbon atoms were reported. Using the same scheme, Palmer et al.[60] developed a detailed atomistic model for a widely used industrial adsorbent bituminous coal-based carbon (BPL) with true density of 2.23 g/cm^3. Highly heterogeneous structures with large proportion of five, six- and seven-member rings were observed in these the models. The biggest concern about reverse Monte Carlo methods is that these methods heavily depend on the initial structures, density and the accuracy of experimental inputs.

Mimetic techniques aim to simulate the synthesis process of activated carbons, thus require the detailed knowledge of the chemical reactions. Activated carbon contains smaller amount of hydrogen, oxygen, sulfur and nitrogen, depending on the chemistry of the precursors. It is very difficult to simulate the complete experimental procedure due to the heavy computational demand which is well beyond current supercomputer capacities. Gelb and Gubbins [61] developed a realistic model for porous Vycor glasses by quenching a binary Lennard-Jones system and removing one phase after phase separation. Using lattice Monte Carlo simulations, Bhattacharya and Gubbins [62] mimicked the synthesis of mesostructured cellular foam (MCF) consisting of large spherical cells with diameter larger than 100Å. These approaches can provide good representations of porous materials at the mesoscale. However, for activated carbons the structural details at the atomic scale are more important to hydrogen adsorption and more difficult to probe experimentally and theoretically. More complex simulation systems containing various hydrogen contents were tried to mimic the process by which the amorphous carbons are produced. Kumar et al.[63] used polymer chains as the initial structures in Monte Carlo simulations to model the experimental preparation of nanoporous carbons by pyrolysis from polyfurfuryl alcohol. The paper by Godwin et al.[64] is the first work that cooled the molten carbon hydrogen mixture with benzene and ethane precursors to get amorphous hydrogenated amorphous carbon. They employed a tight binding model and investigated the effects of different molecular precursors to the final amorphous structures. Iarlori et al.[65] used more accurate first principle calculations to generate a structural model for a hydrogenated amorphous carbon film with low H content. Houska et al.[66] using ab initio calculations simulated the process of plasma-enhanced chemical vapor deposition

(PECVD) from hydro-carbon-containing gases. They investigated hydrogenated amorphous carbon structures, especially the role of unbonded H_2 in amorphous carbon formation. Most of the above work was limited by the computational power. Only small number of molecules (usually less than 150 atoms) were considered in the simulations, limiting the size of the structural features.

2.3 Gas Adsorption Calculation Methods

According to the International Union of Pure and Applied Chemistry (IUPAC) classification, pores are classified as macropores for pore widths larger than 500 Å, mesopores for the pores ranging from 20 to 500 Å and micropores for pores smaller than 20 Å. The mechanism of pore filling in micropores is very different than that in larger pores due to the strong adsorbent-adsorbant interaction in micropores. The filling of micropores usually occurs at very low relative pressures. In order to interpret the gas adsorption isotherm from experiments and the confined gas behavior, methods including density functional theory (DFT), Monte Carlo (MC) simulation, molecular dynamics (MD) simulation, and Patchkovskii et al.'s quantum mechanical method were developed and frequently used in gas adsorption calculations. This section provides a quick review of the above methods.

Density functional theory (DFT) is a statistical thermodynamic approach that calculates the local fluid density in the presence of a spatial varying external force. The density

profile is determined by minimizing the grand potential functional using a numerical iteration scheme. Once the local density is obtained, other thermodynamic properties such as adsorption isotherm and heat of adsorption can be calculated. Seaton et al.[67] was the first to use the DFT method to determine the pore size distribution over both the micropore and mesopore size range. Gubbins[68] modeled simple spherical molecules in carbon slit pore based on the nonlocal mean-field density functional theory (NLMFT). The interaction parameters were chosen to represent methane or ethylene as the adsorbed gases. By comparing with GCMC calculations in the same carbon structure, quantitatively accurate agreements were obtained by density functional theory except for the smallest pore size. The mixture of methane-ethane adsorption in carbon slit pores was also studied by using density functional theory and a Lennard-Jones mixture.[69] To simulate inhomogeneous adsorbent systems, Rocken and Tarazona[70] constructed a periodic wall potential that causes fluid attraction and repulsion altering along the wall and studied the gas adsorption properties by density functional theory. The calculations of spherical gas molecules adsorption in slit pores and cylindrical models have provided useful information for extracting the pore size distribution from experimental adsorption isotherms. The calculation of DFT becomes much more difficult for more complex pore geometries or nonspherical molecules. Until now most of the DFT studies have not gone beyond simple planar or cylindrical pores.

The Grand Canonical Monte Carlo (GCMC) simulation method is considered as the standard algorithm for study of adsorption and wetting phenomena of fluids in solids. This method simulates an open system with fixed temperature, volume, and chemical

potential. This corresponds to experimental conditions where the adsorbed gas is equilibrated with a large gas reservoir. GCMC creates a series of configurations which, in equilibrium, correspond to a grand canonical distribution and are controlled by numerous trials of particle insertion, deletion, and replacement. These trials are accepted or rejected based on the temperature and the chemical potential change. The physical parameters of interest such as gas adsorption amount, potential energy, and isosteric heat of adsorption can be determined by averaging the values or evaluating the fluctuations over the Markov chain. GCMC has been intensively used to estimate the hydrogen adsorption in various carbon materials including carbon nanotubes[38, 71-72], slit pores[28, 72], doped graphite sheets [39], and more complex nanoporous structures[38] for a wide range of temperatures and pressures. At sufficiently low temperatures, the gas molecule can no longer be treated as classical particle when confined to a small pore because the de Broglie wavelength is comparable to the pore size. To consider the quantum effects at low temperature, Wang and Johnson[73] derived and employed the path integral hybrid Monte Carlo method to calculate the adsorption isotherm of hydrogen on the graphite basal plane and in graphite slit pores. Significant quantum effects were observed while comparing quantum and classical simulations at 20 K. They attributed the difference between quantum and classical calculations to the larger effective diameter of quantum molecules. Further investigations in single wall carbon nanotubes[74] demonstrated that the quantum effects were important even at 298K for hydrogen adsorption in nanotube interstices. More investigations showed that the quantum nature of hydrogen at low temperature caused the suppression of the critical temperature [75] and molecular sieving between D_2 and H_2 [76].

Molecular dynamics simulation is a more intuitive method compared to GCMC and DFT. Molecular dynamics can model gas diffusion and adsorption/desorption in solids. However, this method is less frequently used due to the lengthy simulation process. Burress used molecular dynamics simulations to calculate the hydrogen adsorption isotherm in the simple slit pore model for various temperatures and number of gas molecules.[47] A series of extensive molecular dynamics simulations[77-81] were performed for hydrogen adsorption in single walled carbon nanotubes. Good agreements with experiments were obtained on the heat of adsorption. It was shown that H_2 tended to adsorb in the outside of carbon nanotube bundle at low H_2 loading and inside the tubes at higher H_2 loading. The results also showed high H_2 mobility in carbon nanotubes.

Patchkovskii et al.[1] proposed a numerical method to evaluate hydrogen adsorption with the consideration of quantum effects. In this method, the canonical partition functions of free gas (bulk gas in the reservoir) and the adsorbed gas are obtained by equation (2.1)

$$q = \sum_i \exp\left(-\frac{\varepsilon_i}{kT}\right) \tag{2.1}$$

Where q is the canonical partition function, ε_i is the energy level, k is the Boltzmann constant, T is the temperature. The energy levels ε_i are determined by solving the one-particle Schrodinger equation of gas molecule motion in the adsorbing potential or free space for adsorbed gas and free gas, respectively. The effective internal gas pressure P_{int} is calculated by

$$P_{\text{int}} = K_{eq} P_{ext} = \frac{q_{ads}}{q_{free}} P_{ext} \qquad (2.2)$$

Where K_{eq} is defined as the equilibrium constant, P_{ext} is the external pressure, q_{ads} and q_{free} are the canonical partition functions for free gas and adsorbed gas, respectively. The stored hydrogen density is estimated from an experimental equation of state. The volumetric and mass weight density can be calculated accordingly. Their calculations suggest that the DOE specification can be achieved by physisorption in graphite-based system. The maximum hydrogen adsorption occurred in graphene systems with interlayer spacing between 6-7 Å at different temperatures and pressures. Using a better empirical equation of states for hydrogen gas and ab initio calculation of the interaction potential between hydrogen and adsorbents, Cabria et al.[82] applied Patchkovskii's. method to carbon and BN slit pore models. However, solving the Schrodinger equation of single particle in a complex potential surface such as the adsorption potential in amorphous carbons will be difficult and limit the application of this method.

CHAPTER III

CONTINUUM MODEL OF GAS ADSORPTION

In this chapter we introduce a continuum model for calculating the equilibrium gas adsorption in porous solids, given the gas equation of state (EOS) and assuming that the interaction between the gas and solid is known. By comparing our calculations in the expanded graphite model with previous more computational expensive methods, we successfully demonstrate the accuracy and efficiency of this numerical model. We further apply this model to predict hydrogen storage in amorphous carbon structures and ZnO sheet at room temperature. The amorphous carbon structures were generated by empirical Tersoff potential. We are well aware of the limitations of Tersoff potentials in modeling low density carbons. Therefore, in Chapter IV we will utilize a more accurate tight-binding method to simulate amorphous carbon structures and calculate the gas adsorption in Chapter V. In the end of current chapter, we carefully discuss the limitations of this continuum model including quantum effects of adsorbed gas at room temperature.

3.1 Theory

In an ideal gas, the chemical potential (μ) at temperature T and pressure P is given by

$$\mu^{ideal}(T,P) = \mu_0(T,P_0) + k_B T \ln(P/P_0) \tag{3.1}$$

where k_B is the Boltzmann constant, P_0 is a standard or a reference pressure, which is ordinarily taken to be 1 atm.[83] To describe the chemical potential of a real gas in the same form, the fugacity *f(T,P)*, with the units of pressure, was introduced as one of the parameters that define the grand canonical ensemble in statistical mechanics.

$$\mu^{real}(T,P) = \mu_0(T,P_0) + k_B T \ln(f(T,P)/P_0) \tag{3.2}$$

The fugacity coefficient *f/P* is unity for an ideal gas but increases with pressure (at room temperature and over the pressures considered here) in a nonideal H_2 gas. The deviation is expected to be less than 4% at room temperature with pressures lower than 1000 atm.[84] Thus, at room temperatures and moderate pressures, the chemical potential of H_2 gas can be reasonably estimated by the pressure *P* and temperature *T* according to Eq. (3.1).

For equilibrium adsorption, the chemical potential of the external free gas (μ_{ext}) should be equal to that of the adsorbed gas (μ_{int}). Considering that the adsorbed gas is under the adsorbent force fields, we have,

$$\mu_{ext}(T,P_{ext}) = \mu_{\text{int}}(T,P_{ext}) = \mu^{gas}(T,P_{\text{int}}) + E_{ads} \tag{3.3}$$

where P_{ext} is the external pressure measured in the laboratory, P_{int} is the effective internal pressure (the pressure of the adsorbed phase), E_{ads} is the local adsorption potential and $\mu^{gas}(T,P_{int})$ is described by $\mu^{ideal}(T,P_{\text{int}})$ as in Eq. (3.1). By using equations (3.1) and

(3.3), we obtained the effective internal pressure P_{int} as a function of the external pressure P_{ext} and the local adsorption potential E_{ads}:

$$P_{\text{int}} = P_{ext} \exp(-E_{ads} / k_B T) \tag{3.4}$$

This is the key equation for our approach, allowing us to calculate the local pressure in the system as a function of the external gas temperature and pressure. Note that the internal pressure P_{int} varies with the position of H_2 in the system because the adsorption potential E_{ads} changes with the surrounding environment. The local density of molecules (ρ) attracted by this potential is related to the temperature and the local internal pressure according to the gas equation of state (EOS). As shown below, the absorbed densities are locally high enough to require a treatment beyond an ideal gas approximation.

The empirical equation of state (EOS) for hydrogen used in our calculations is from Mills *et al.*[85] This is for a direct comparison with previous Patchkovskii *et al.* calculations where Mills EOS was used. The Mills EOS is expressed as following:

$$\begin{aligned} V = {} & (36.716 + 0.0033003T - 22.479T^{-1/2})P^{-1/3} + (-17.174 - 0.021393T)P^{-2/3} \\ & + (-8.9886 + 0.11001T + 69.233T^{-1/2} - 31.395T^{-1})P^{-1} \end{aligned} \tag{3.5}$$

Where V is the volume of H_2 given in cm^3/mole, P is the pressure given in kbar, and T is the temperature in K. The valid range of Mills EOS is 2<P<20 kbar and 75<T<307K. The EOS was fitted to measurements of the longitudinal sound velocity of hydrogen. The sum S of n sets of experimental points was minimized during the parameter fitting

process: $S = \sum_n [V_{\exp} - V(P,T)]^2 + \sum_n [(1/u_{\exp}) - g(P,T)]^2$, where $V_{\exp}$ is the experimental gas volume, $V(P,T)$ is given in Eq. (3.5), $u_{\exp}$ is the experimental longitudinal sound velocity, $g(P,T) = \frac{1}{u} = \frac{M^{1/2}}{V}[-(\frac{\partial V}{\partial P})_T - \frac{T[(\partial V/\partial T)_P]^2}{C_P}]^{1/2}$, C_P is the heat capacity at constant pressure. The special form of Eq. (3.5) was favored by Mills *et al.* because: (1) its signs of the constants are exactly in the sequence reported by Benedict[86] where the same form was used to fit N_2 data over a similar range of T. (2)The calculated heat capacity at constant pressure was extrapolated to 1 kbar and in good agreement with data reported in the literature. (3) Eq(3.5) remains regular when extrapolated to very high pressures and temperatures. (4) The standard error is not significant when Eq. (3.5) is compared with experimental data.

Using the temperature, the local pressure, and the Mills EOS, we can calculate the local density of the adsorbed fluid. The total adsorption is calculated by integrating the local density over the structure. This method is valid under the conditions that the empirical EOS is valid and the quantum effects are not important. At sufficiently low temperatures or high densities, significant quantum effects are expected due to the hydrogen molecule's low mass, particularly for nanoscale confinements comparable to the thermal de Broglie wavelength. This will be discussed in more detail later in this chapter.

The interaction of nonpolar H_2 molecules with graphitic systems is mainly caused by London dispersion. For direct comparisons with previous work,[1, 28] two different

empirical pairwise potentials were used to describe the C-H_2 interaction. Wang *et al.*[87] proposed a Lennard-Jones form potential by fitting the energy spectra of H_2 physisorbed by planar graphite:

$$u(r) = 4\varepsilon[(\sigma / r)^{12} - (\sigma / r)^{6}] \tag{3.6}$$

where ε=3.69 meV/molecule (0.356 kJ/mol) and σ=2.97 Å, r is the distance between the mass center of the H_2 molecule and the carbon atom. Patchkovskii *et al.*[1] chose the following form,

$$u(r) = Ae^{-\alpha r} + C_6 r^{-6} \tag{3.7}$$

and fitted the parameters according to quantum chemical calculations for an H_2-coronene model system. They obtained A=1099.52 eV/molecule, C_6=-17.3640 eV·Å^6/molecule and α=3.5763 Å^{-1}. In both the Wang and Patchkovskii models, the H_2 molecule was treated as a simple spherical particle without a rotational degree of freedom. The C-H_2 binding energy from Patchkovskii *et al.* potential is 1.8 meV stronger than that of Wang *et al.*[28] This difference has been shown to have a significant effect on H_2 adsorption[28] and is also demonstrated in the next section.

3.2 H_2 Adsorption in Expanded Graphite Model

3.2.1 Comparison of adsorption with other methods

Hydrogen adsorption between graphite layers have been studied by different approaches.[1, 28, 87] In this section we compare our results of the hydrogen adsorption in expanded graphite with the results from other methods. The upper figure of Fig. 3.1 shows the adsorption potential of a single H_2 molecule between two expanded graphene sheets using the Wang *et al.* (Eq. (3.6)) and the Patchkovskii *et al.* (Eq. (3.7)) potentials, respectively. Different colors indicate different interlayer spacing (*d*). The solid curves calculated using the Patchkovskii *et al.* potential are always lower than the dashed curves calculated using the Wang *et al.* potential, due to the more favorable interaction of Patchkovskii *et al.* potential. For three different interlayer spacing (*d* = 6 Å, 7 Å, 8 Å), both models show that as *d* increases, the binding energy becomes weaker and a broader potential well is observed. At smaller distances, the binding energy again decreases, as the repulsive parts of the potentials become dominant. Both potentials have positive interactions when the C-H_2 distance is less than 3 Å. The binding energy is enhanced near *d* = 6 Å due to the combined adsorption potentials from both sides of the slit-shaped pore. For *d* = 6 Å, the lowest potential energy from the Patchkovskii *et al* potential is about -0.15 eV/molecule (-14.5 kJ/mol) which is close to the suitable energy range for practical H_2 storage. However, the potential well is much steeper and narrower for *d* = 6 Å than for larger interlayer spacings, limiting the available adsorption space. The bottom figure of Fig. 3.1 shows the number density (molecules/Å^{-3}) of adsorbed H_2 at 298K, 5 MPa as a function of the position between two graphene layers using the Patchkovskii *et*

al. potential. This has been calculated by applying Eq. (3.4), and using the Mills EOS (Eq. (3.5)). The shapes of the density curves clearly reflect those of the energy curves. The total adsorption amount is proportional to the area below the density curves. As can be seen in Figure 3.2, the absorption is similar for both d=6 Å and d=7 Å, despite the difference in the binding energies.

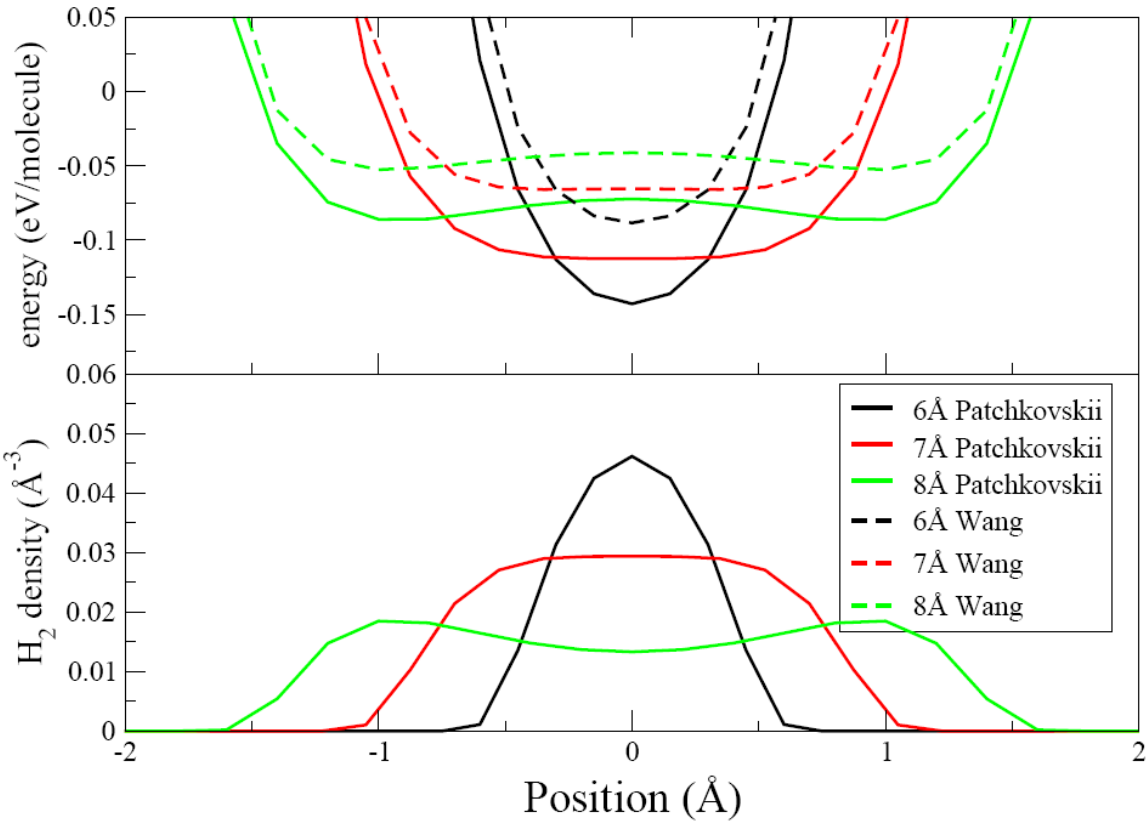

Figure 3.1 (upper) The adsorption energy of a single H2 molecule between two expanded graphene sheets calculated using the Wang et al. and Patchkovskii et al. potentials, respectively. (bottom) H2 density profile between two expanded graphene sheets, calculated using the Patchkovskii et al. potential at 298K and 5MPa.

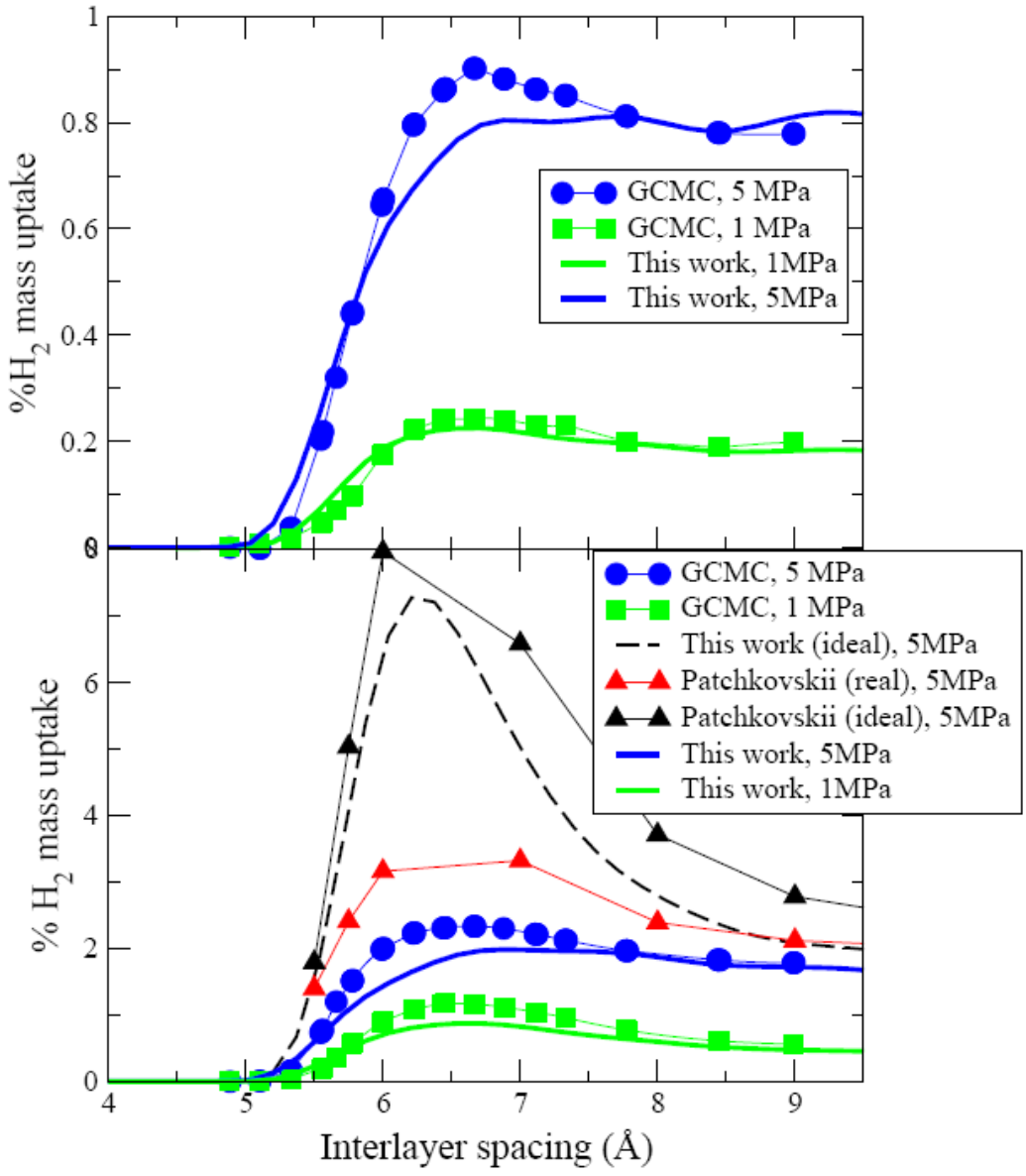

Figure 3.2 Hydrogen adsorption as a function of graphite interlayer spacing at 298K for 1 MPa and 5 MPa using Wang et al. (top) and Patchkovskii et al. potentials (bottom), respectively. Ideal gas and non-ideal gas descriptions are applied. The GCMC results are from Aga et al.28 and Patchovskii results are from Patchovskii et al.1. Details are given in the text.

Figure 3.2 shows the percentage of hydrogen mass uptake as a function of graphite interlayer spacing (*d*) at 298 K and two different pressures (1 MPa and 5 MPa). The data are from GCMC calculations[28], the calculations of Patchkovskii *et al.,*[1] and our calculations, respectively. Patchkovskii *et al.* solved the one-particle Schrodinger equation for an H_2 molecule in the potential of graphite sheets; from this, the eigenstates are used to determine the partition function and adsorption of the system. Our method has the advantage of avoiding either the quantum mechanical calculations or time consuming GCMC simulations. The accuracy of this method is demonstrated below.

If the C-H_2 interaction is modeled by Eq. (3.6) from Wang *et al.* (upper graph), our maximum mass uptakes predicted by the nonideal gas approximation are 0.24% and 0.80% for 1 MPa (green solid curve) and 5 MPa (blue solid curve), respectively, in close agreement with the GCMC calculations. If the Patchkovskii *et al.* potential (Eq. (3.7)) is used (bottom graph), the maximum uptakes predicted by the nonideal gas approximation are 0.87% and 1.98% for 1 MPa (green solid curve) and 5 MPa (blue solid curve), respectively. The corresponding values from GCMC (circles and squares) are also close to our values, respectively. Compared to GCMC and our results, Patchkovskii *et al*. obtained slightly higher adsorptions at 5 MPa (red triangles). The H_2 EOS used by Patchkovskii *et al.* was the Mills EOS, the same as the one used in our work. At the temperature of 298K and the external pressure of 5 MPa, the highest effective internal pressure P_{int} is calculated as close to 1000 MPa when using the Patchkovskii *et al.* potential. This will highly compress H_2 molecules and induce a very dense fluid. To

demonstrate the importance of the nonideality of H_2 gas at high pressures, the ideal gas EOS is also applied and the results are presented in the same figure. The black triangles are from Patchkovskii *et al*. and the black solid curve is from our calculations. Again, the results compare well. The ideal gas calculations overestimated the maximum adsorption by a factor of 2.5 to 3.5, compared to a more realistic EOS. The significant consistency between the previous work and our calculations using various EOS demonstrates the validity and accuracy of our method.

The above studies show that there is essentially no uptake for graphite layers with interlayer spacing less than 5 Å due to insufficient space for adsorption. The uptake is highest for a interlayer spacing close to 6.5 Å. At this spacing, the strongest binding is lower than that at a spacing of 6 Å, but the uptake is more, due to a larger volume available for adsorption. There is a competition between the large pore volume required to enhance hydrogen storage capacity and the resulting decrease in the adsorbate-adsorbent interaction energy in wider pores. Thus, tuning the geometry to increase the adsorption energy may not give the maximum uptake. In experiments, it was revealed that micropores larger than 7 Å were not effective to adsorb H_2 at room temperature, in agreement with the calculations.[43, 88]

3.2.2 Heat of adsorption

The isosteric heat of adsorption q_{st} is defined as the differential change of energy that occurs when an infinitesimal number of molecules are adsorbed at constant pressure and

temperature. In this section, we calculate q_{st} at zero coverage limit by virial equation analysis. A more rigorous numerical analysis is applied to calculate the isosteric heat at higher adsorptions; in the low adsorption limit, these two calculations are consistent. The C-H_2 interaction is modeled by Eq. (3.7) of Patchkovskii *et al.* for the isosteric heat calculations.

The virial equation can be written in the form

$$\ln(n/P) = A_0 + A_1 n + A_2 n^2 + \ldots \tag{3.8}$$

where n is the hydrogen mole uptake per gram of carbon in the unit of mol/g , P is the external pressure in the unit of Pa. We show relevant plots at four different temperatures in Figure 3.3 for the expanded graphite structure with an interlayer spacing of 6 Å. As can be seen, the adsorption can be fit to Eq. (3.8) adequately using only the A_0 and A_1 terms. The intercept and the slope of the plots give the first and second coefficients. A_1 is a function of adsorbate-adsorbate interactions. A_0 reflects the adsorbate-adsorbent interaction, and is related to the Henry's law constant K_H by the equation K_H=exp(A_0):

$$A_0 = -q^0 / RT \tag{3.9}$$

where q^0 is the isosteric heat at zero adsorption, and R is the gas constant. The value of q^0 can be obtained by a graph of A_0 vs. $1/T$ (Fig. 3.4). This gives a value of 15.6 kJ/mol, close to the experimental value of 17.8 kJ/mol of ultramicroporous carbon (UMC).[48] The UMC has a high pore volume, with more than half of total pore volume in narrow

micropores (<0.7 nm). This supports the idea that the graphene sheets can be treated as a rough approximation for real, more complex carbon structures.

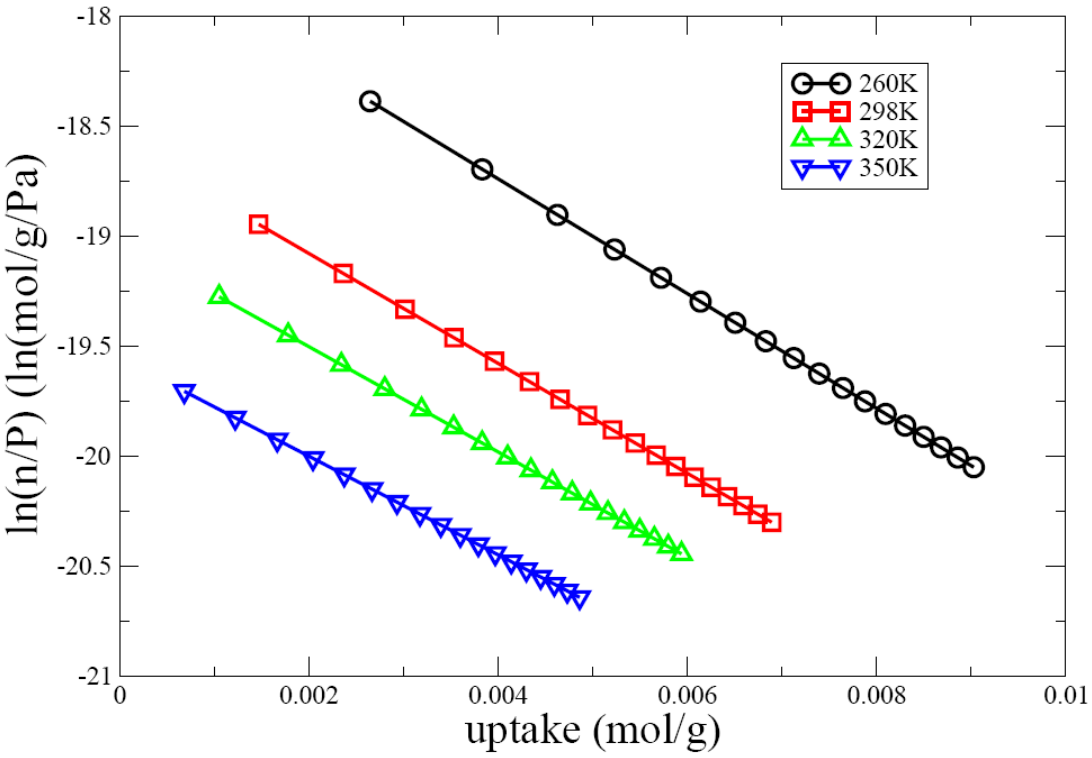

Figure 3.3 Virial graphs for the adsorption of hydrogen between two graphite layers with 6 Å spacing at four temperatures. (260 K to 350 K)

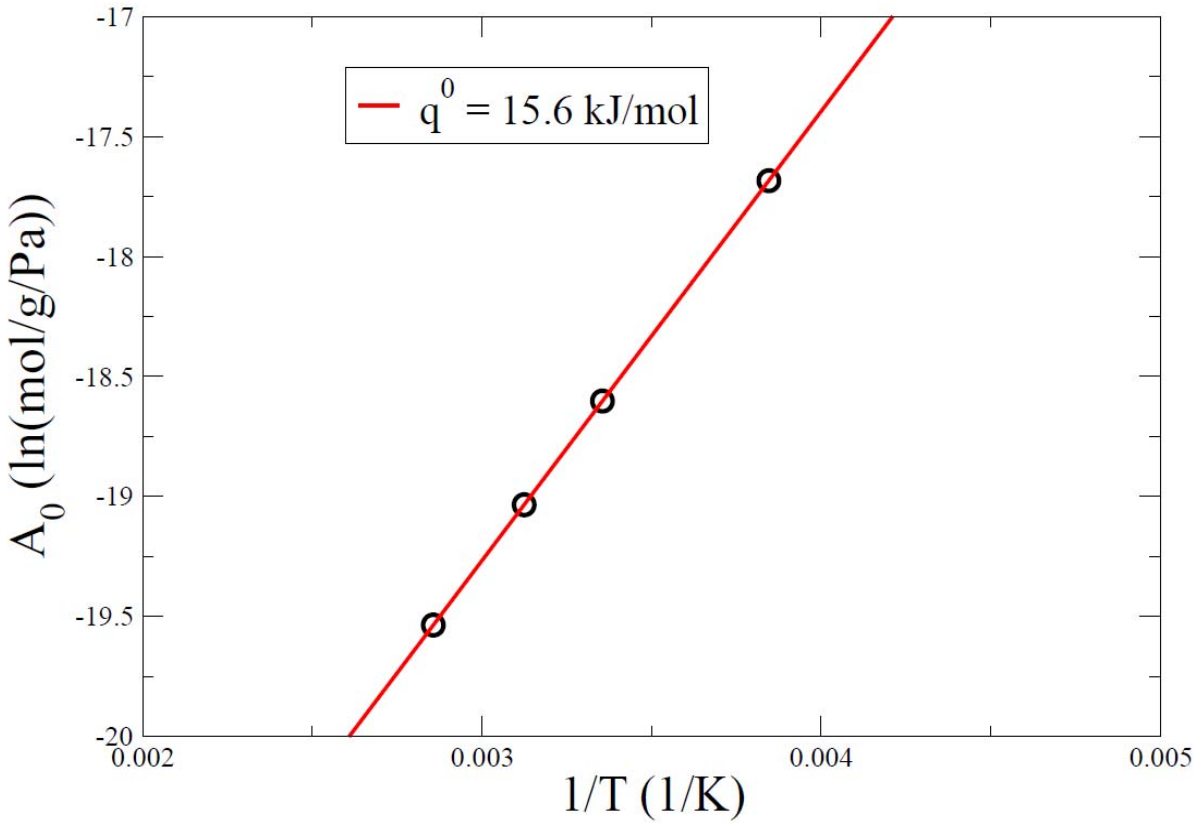

Figure 3.4 The variation of A_0 with $1/T$ for hydrogen adsorption between two graphite layers with 6 Å spacing.

We calculate the isosteric heat of adsorption at higher adsorption directly by the Clausius-Clapeyron equation:

$$q_{st} = RT^2 \left(\frac{d(\ln P)}{dT} \right)_N \tag{3.10}$$

where N is the total adsorbed hydrogen amount. This equation neglects the adsorbed phase molar volume relative to the molar volume of the external gas, and assumes the bulk (external) gas is ideal, which are reasonable at the pressures and temperatures studied here. The differentiation in Eq. (3.10) is evaluated numerically using the Mills EOS, where the density of gas is a function of the internal pressure and temperature. Note that the internal pressure also depends on the temperature and adsorption potential through Eq. (3.4). Figure 3.5 shows the isosteric heat as a function of hydrogen uptake at different temperatures in the expanded graphite model with the interlayer spacing of 6 Å. Due to the interactions between adsorbates, the isosteric heat decreases as the uptake increases. The average adsorption energy is defined as the total potential energy divided by the total adsorption amount. We evaluate the average adsorption energy by weighting the local potential by the local hydrogen uptake. The average adsorption energy decreases as the uptake increases, indicating that at equilibrium the hydrogen gas fills up the spaces with the strongest interactions first. In the zero coverage limit, the isosteric heat is estimated as 15~16 kJ/mol according to Fig. 3.5. This is in good agreement between the isosteric heats of adsorption calculated above, thereby confirming the validity of the calculations. At low uptake, the isosteric heat varies with temperature due to the work that the system has done to its surroundings when small amount of molecules

are adsorbed. The work done by the system is proportional to the temperature for the ideal gas or the nonideal gas at low uptake.

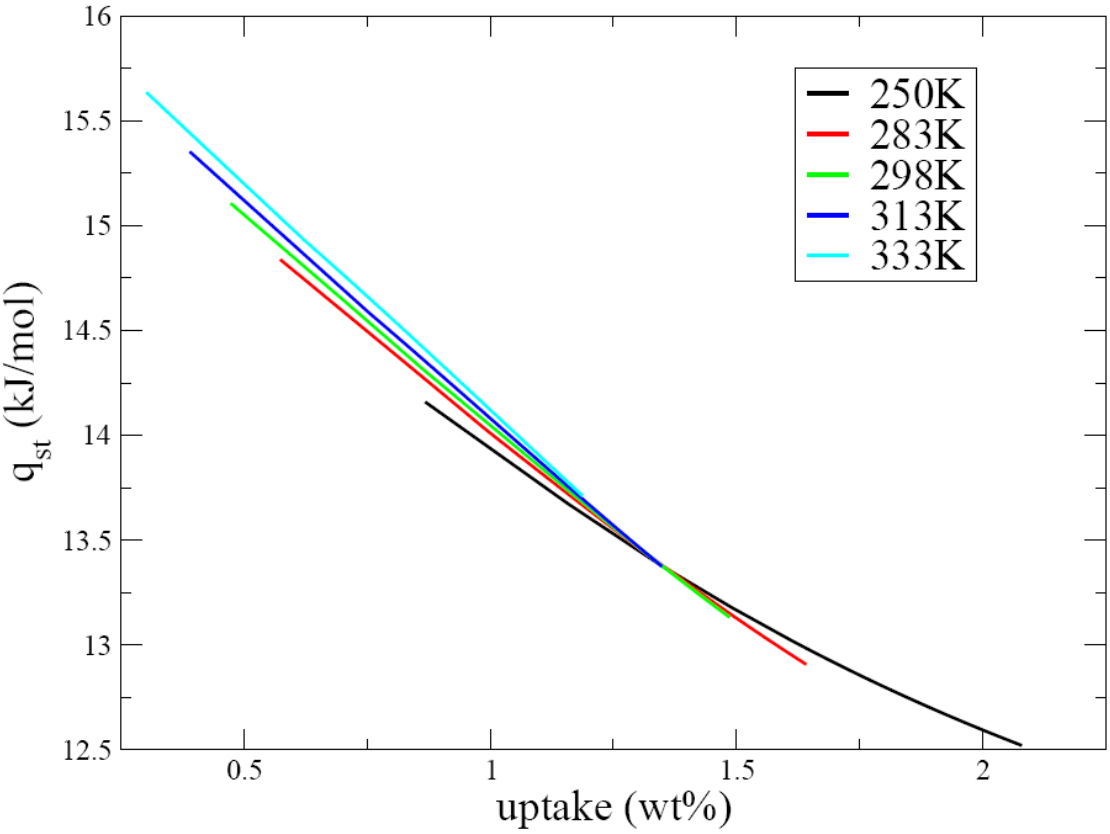

Figure 3.5 The variation of isosteric heat (q_{st}) with hydrogen uptake between two graphite layers with 6 Å spacing at different temperatures. (250 K to 333 K)

3.3 Applications in Other Systems

As mentioned in Chapter II, nanoporous carbons such as activated carbons, carbon nanotubes and graphite nanofibers are of particular interest due to their high surface areas and tunable pore sizes through chemical activation and finely selected precursors. The experimental results of hydrogen storage in nanoporous carbons[35, 89-90] are widely varying due to different samples, preparation methods, experimental errors such as impurities in the samples, low purity hydrogen, and different methods to estimate the hydrogen adsorption capacity. Simulation studies have provided more consistent results in graphite nanofibers and carbon nanotubes, demonstrating very low (<1 wt%) hydrogen adsorption capacity at room temperature and 10 MPa.[30, 91] However, these previous theoretical adsorption calculations only consider simple pore geometries.

Recently, high levels of hydrogen uptake (0.8 wt %) at ambient temperature (25 ^{o}C) and moderate pressures (2 MPa) was observed in ultramicroporous carbon.[48] Although alkali metal doping was argued to contribute to the large uptake by polarization-enhanced physisorption, we are interested in the theoretical maximum hydrogen uptake in pure amorphous carbons. By applying our continuum adsorption method we make the first prediction of the hydrogen storage capacity in amorphous carbon structures at room temperature. In this section, the amorphous carbon structures are modeled by the well-established empirical Tersoff potential [92] for quick and large scale simulations. We further extend our continuum adsorption model in other solid-gas system (ZnO-H_2 system). ZnO sheet has the planar graphene-like structure. The slightly charged Zn and

O atoms are demonstrated to bind hydrogen molecule with strong adsorption energy. In this section, with the cooperation with researchers in University of Science and Technology of China (USTC), we predict the hydrogen adsorption on ZnO sheet at room temperature.

3.3.1 Hydrogen Adsorption in Tersoff Amorphous Carbons

The Tersoff potential[92-93] is a bond order potential containing up to three body interaction and has been widely used in covalent systems (e.g. carbon, silicon, and germanium). The system potential E is written as,

$$E = \sum_i E_i = \frac{1}{2}\sum_{i \neq j} V_{ij} = \frac{1}{2}\sum_{i \neq j} f_c(r_{ij})\left[a_{ij} f_R(r_{ij}) + b_{ij} f_A(r_{ij})\right] \tag{3.11}$$

Where E_i is the potential energy of atom i, V_{ij} is the bonding energy between atom i and j, r_{ij} is the distance between atom i and j. The indices i and j run over the atoms of the system. f_A and f_R are the attractive and repulsive pair potential, respectively, and f_C is the smooth cutoff function, to limit the range of the potential.

$$f_R(r) = Ae^{(-\lambda_1 r)} \tag{3.12}$$

$$f_A(r) = -Be^{(-\lambda_2 r)} \tag{3.13}$$

$$f_C(r) = \begin{cases} 1, & r < R - D \\ \frac{1}{2} - \frac{1}{2}\sin(\frac{\pi}{2}(r - R)/D), & R - D < r < R + D \\ 0, & r > R + D \end{cases} \tag{3.14}$$

Where $f_c(r)$ has continuous value for all *r*, and goes from 1 to 0 in a small range around *R*. *R* is usually fitted to include only the first-neighbor shell for most structures of interest. b_{ij} has the following form.

$$b_{ij} = (1+\beta^n \xi_{ij}^n)^{-1/2n} \tag{3.15}$$

$$\zeta_{ij} = \sum f_c(r_{ik}) g(\theta_{ijk}) \exp\left[\lambda_3^3 (r_{ij} - r_{ik})^3\right] \tag{3.16}$$

$$g(\theta) = 1 + c^2/d^2 - c^2/\left[d^2 + (h - \cos\theta)^2\right] \tag{3.17}$$

Where θ_{ijk} is the bond angle between bonds *ij* and *ik*. a_{ij} is expressed as following.

$$a_{ij} = (1+a^n \eta_{ij}^n)^{-1/2n} \tag{3.18}$$

$$\eta_{ij} = \sum_{k \neq i,j} f_c(r_{ik}) \exp[\lambda_3^3 (r_{ij} - r_{ik})^3] \tag{3.19}$$

For carbon, the fitted parameters are $A = 1393.6eV$, $B = 346.7eV$, $\lambda_1 = 3.4879 \overset{0}{A}^{-1}$, $\lambda_2 = 2.2119 \overset{0}{A}$, $\beta = 1.5724 \times 10^{-7}$, $n = 0.72851$, $c = 38049$, $d = 4.3484$, $h = -0.57058$, $R = 1.95 \overset{0}{A}$, and $D = 0.15 \overset{0}{A}$. For simplicity, the parameters α and λ_3 have been set to be zero.

To model the amorphous carbon structures, we equilibrated liquid carbon at 6000 K for more than 10^5 time steps (1.75×10^{-10} s) before quenching the structures to 300 K while keeping the carbon density constant. The MD time step was 1.75×10^{-15} s. A relatively

low quenching rate (5.7 K/ps) was used to simulate the quenching experiments while keeping the computation time affordable. The temperature was simply controlled by rescaling the velocity of atoms. 4000 atoms were utilized in our simulations with the periodic boundary condition. The final structure was divided into a 100×100×100 grid. The adsorption energy was calculated using the Patchkovskii *et al.* potential (Eq. (3.7)) for every individual point on the grid. Figure 3.6 shows a portion of the simulated carbon structure (gray) with a density of 1.25 g/cm^3. The positions with strong local adsorption energies (lower than -0.1 eV/molecule) are shown in the same figure, and colored by the energy from red (high value) to blue (low value). Graphitic segments are observed in the simulations, in agreement with the diffraction experiments from activated carbons and tight binding molecular dynamics simulations in low density carbons.[94-96] According to the relationship between local adsorption energy and the hydrogen density as expressed in Eq. (3.4) and (3.5), Figure 3.6 demonstrates that hydrogen molecules are likely to aggregate inside narrow pores instead of wide open areas, consistent with the experimental results that narrow micropores are preferential adsorption sites.[35] The total hydrogen uptake at 298 K, 5 MPa was calculated as 0.55 wt% for this structure, close to the highest values reported for activated carbons under the same temperature and pressure conditions [46].

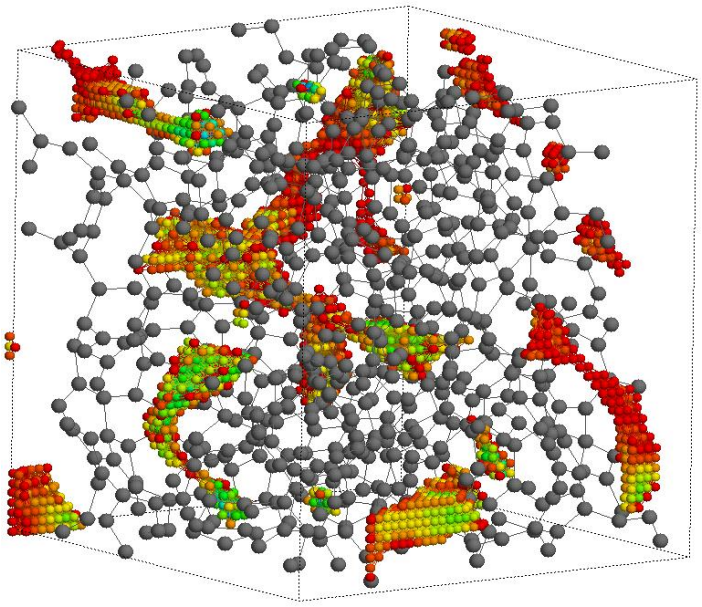

Figure 3.6 A portion of the simulated amorphous carbon structure (gray) with density of 1.25 g/cm3 and the positions with adsorption energy less than –0.1 eV/molecule. The positions are colored by the adsorption energies from red (high energy) to blue (low energy).

Figure 3.7 and Table 3.1 summarize the calculation results in amorphous carbons. The simulated carbon density was calculated according to the mass of the carbon atoms and the volume of the unit cell. For each carbon density, we performed at least three independent molecular dynamics simulations and adsorption calculations. We define the space that favors physisorption (adsorption energy < 0.0 eV/molecule) as the available space for hydrogen adsorption. The available space decreases as the carbon density increases, from an average of 29% for 1.25 g/cm^3 to 2.4% for 1.8 g/cm^3, due to less open structures and more four-fold bonds at higher carbon densities. The total hydrogen mass uptake w_{total} decreases as well, showing that the storage is roughly proportional to the available volume (Figure 3,7). The average total uptake changes from 0.48 wt% for a carbon density of 1.25 g/cm^3 to 0.15 wt% for 1.8 g/cm^3. There is no uptake for structures with densities larger than or equal to 2.5 g/cm^3 according to the calculations.

To better evaluate the effects of adsorption energy, we calculated the excess adsorption w_{excess} by subtracting the total uptake w_{total} by the mass of gas molecules that would have occupied the same "available" volume neglecting the attractive adsorbent-adsorbate interaction. Additionally, we evaluated the volumetric efficiency by comparing the total amount of gas (w_{total}) adsorbed in carbon structures and the amount of gas in an empty tank (w_0) with the same total volume at the same *(T,P)* conditions. Table 3.1 shows that the average excess adsorption (w_{excess}) and the volumetric efficiency (w_{total}/w_0) are similar for carbon structures with density of 1.25 g/cm^3 and 1.55 g/cm^3, regardless of the large difference in their available volumes. This fact indicates a stronger adsorbent-adsorbate interaction in the carbon structures with density of 1.55 g/cm^3, and again reveals the

competition between optimizing the volume available to adsorption and optimizing the heat of adsorption for high uptake. Note that the carbon structures with density of 1.80 g/cm^3 have a smaller capacity than an empty tank for hydrogen storage. The isosteric heat of adsorption in the low pressure limit at 298 K changes from ~14 kJ/mol for the carbon density of 1.25 g/cm^3 to ~18 kJ/mol for 1.8 g/cm^3 (Table 3.1). This is similar to what is seen in the overlap of adsorption potential of graphite layers as in Figure 3.1: for large separations, a narrower slit implies a stronger interaction. Similar to the case for expanded carbon, the isosteric heat q_{st} decreases as uptake increases (not shown in the Fig. 3.7 or Table 3.1), indicating the heterogeneity of adsorption potential energy and the strong interactions between hydrogen molecules.

It should be noted that the carbon density reported here was calculated directly using the mass of carbon atoms and the volume of the unit cell. The density in simulation is different from the "skeletal" density referred in experiments, where the spaces accessible to helium are excluded from the density calculation. For better comparisons, the simulation density should be converted to the "skeletal" density in experiments, or vice-versa. Further discussions will be presented in Chapter IV.

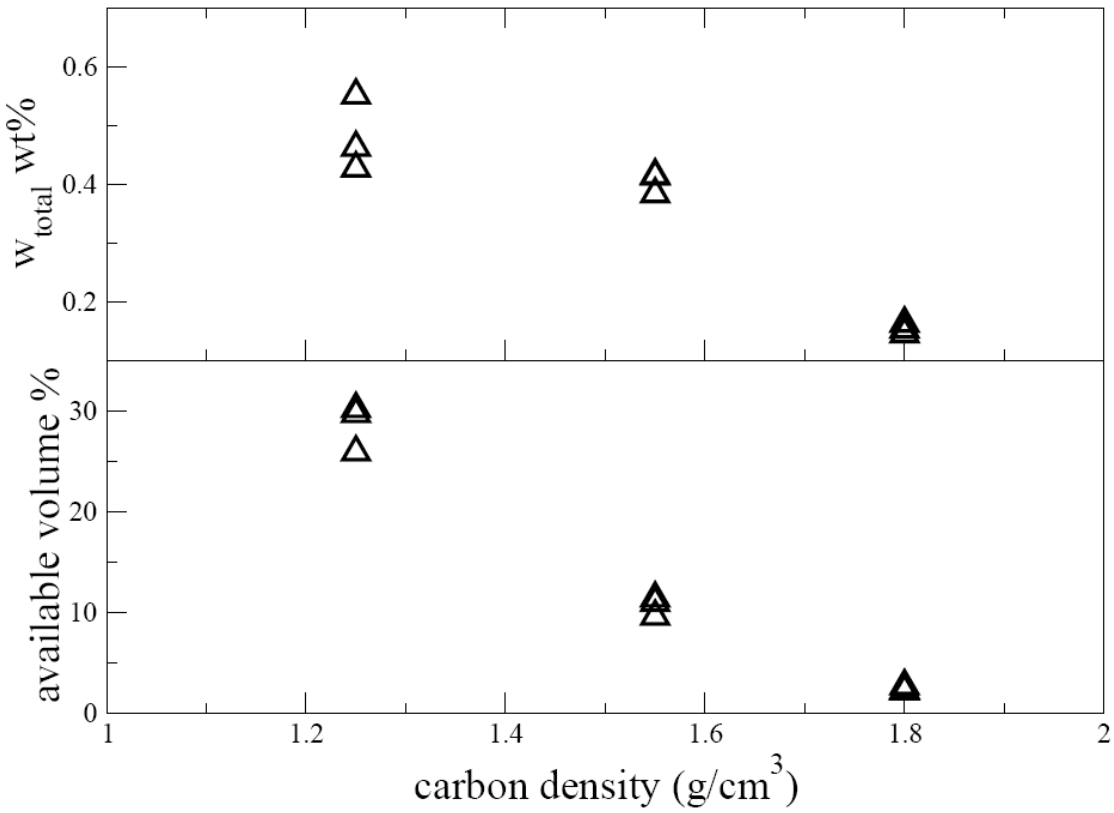

Figure 3.7 The total H_2 adsorption (top) and available adsorption volume (bottom) in amorphous carbons as a function of carbon density at 298K and 5 MPa.

Table 3.1 Results for hydrogen adsorption in amorphous carbons (T=298K, P=5MPa) including total adsorption (w_{total}), excess adsorption (w_{excess}), ratio of hydrogen gas in carbon structures to that in an empty tank (w_{total} /w_0), available volume, and isosteric heat at zero uptake limit (q_{st}). w_0 is the mass of gas contained in an empty tank with the same total volume at the same pressure and temperature condition. The results are average over at least three independent calculations.

carbon density (g/cm^3)	w_{total} (wt%)	w_{excess} (wt%)	w_{total} /w_0	available volume (%)	q_{st} (kJ/mol)
1.25	0.48	0.39	1.50	28.6	14.4
1.55	0.40	0.37	1.54	10.8	15.8
1.80	0.154	0.153	0.69	2.4	18.0

3.3.2 Hydrogen Adsorption on ZnO sheet

A planar graphene-like configuration of ZnO was recently predicted and experimentally synthesized.[97-98] The ZnO sheet has the planar honeycomb lattice configuration with alternating zinc and oxygen atoms. Since there is an electronegativity difference between the zinc and oxygen atoms, there is a charge transfer from oxygen to zinc (leaving a negative charge on the oxygen and positive charge on the zinc). Our collaborators from University of Science and Technology of China (USTC) employed the density functional theory (DFT) with the local density approximation (LDA) to calculate the adsorption energy of hydrogen on ZnO sheet. In their calculations[99], the DFT implemented in the SIESTA package[100-102] was employed for the structural optimization and total energy calculations. The norm conserving pseudopotentials generated using the Troullier-Martins[103] scheme were used to described the interaction of valence electrons, which were expressed in a fully separable form developed by Kleinman and Bylander.[104-105] Double-ζ basis sets plus polarization orbitals (DZP) were utilized for Zn and O atoms and double-ζ basis set (DZ) was for H atoms, respectively. The local density approximation (LDA) with the exchange-correlation potential in form of Perdew-Zunger (PZ)[106] was adopted. A supercell consisting of 5×5 unit cells of perfect ZnO sheet was taken into account to simulate an infinite ZnO sheet, in which a vacuum region of 20 Å perpendicular to the plan of the sheet was employed. Such a large vacuum region was to avoid the interaction between images caused from the periodic boundary condition. The Brillouin zone was sampled with using a $6\times6\times1$ Monkhorst-Pack grid. The conjugate gradient (CG) algorithm was adopted to fully relax the structures until the residual force

acting on each atom is no more than 0.02 eV/ Å. The optimal length of the Zn-O bond for the perfect sheet in the calculations was found to be 1.90 Å, which was slightly shorter than the corresponding one in the ZnO bulk.[107]

They have relaxed two isolated hydrogen atoms on the planar ZnO sheet and found that one hydrogen molecule adsorbing on the sheet was more stable than the two isolated hydrogen atoms on the sheet. The adsorption behaviors of individual hydrogen molecule were studied by placing individual hydrogen molecules on different sites of the planar ZnO sheet. Eight different configurations were considered: the H-H bond is (I) perpendicular to the plane on the top of an O atom, (II) perpendicular to the plane on the top of a Zn atom, (III) perpendicular to the plan above the center of Zn-O bond, (IV) parallel to the Zn-O bond, (V) perpendicular to the Zn-O bond, (VI) parallel to a diagonal line of a hexagon, or (VIII) rotated by 30^{o} with respect to the case VII. The strongest binding energy was found to be -0.131 eV/molecule when the hydrogen molecule was perpendicular to the plane on the top of an O atom. In fact, the binding energies for all the sites tested were calculated between 0.1 to 0.2 eV/H_2, within the desired energy range of hydrogen storage. Detailed binding energies are presented in Table 3.2. Figure 3.8 shows the configurations and binding energies of single hydrogen molecules adsorbed on different sites after relaxation. The hydrogen storage capacity of a single ZnO sheet can be up to 4.7wt% while each O atom adsorbs two hydrogen molecules on both side of the sheet. Figure 3.9 shows the adsorption energy curve of one hydrogen molecule desorbed from ZnO sheet.

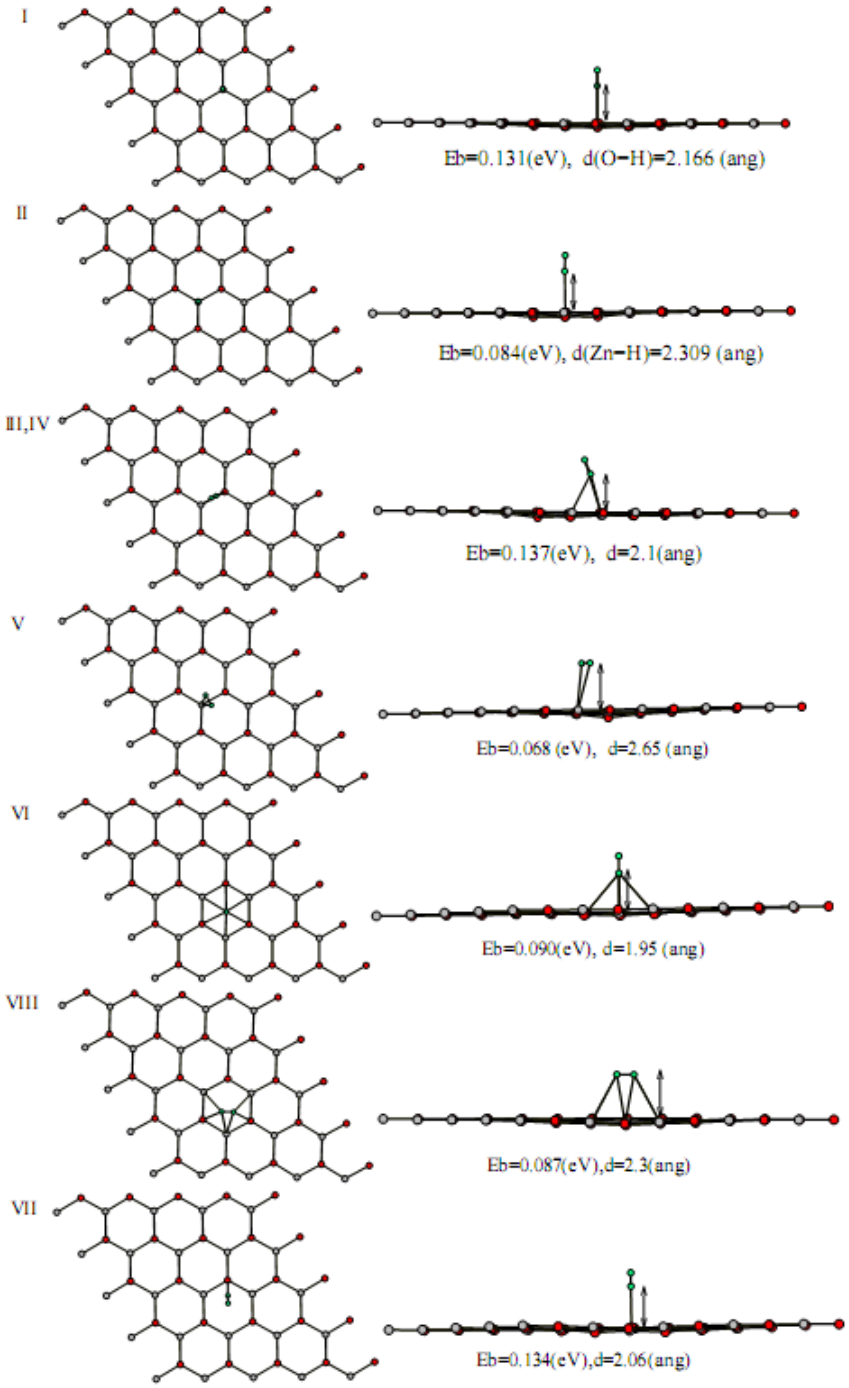

Figure 3.8 Eight optimal structures for a single hydrogen molecule adsorbing on ZnO sheet [99]. The left panels are the top view, and the right panels are the side views.

Binding energy and the distance between the plane and the center of H_2 are denoted in the figure.

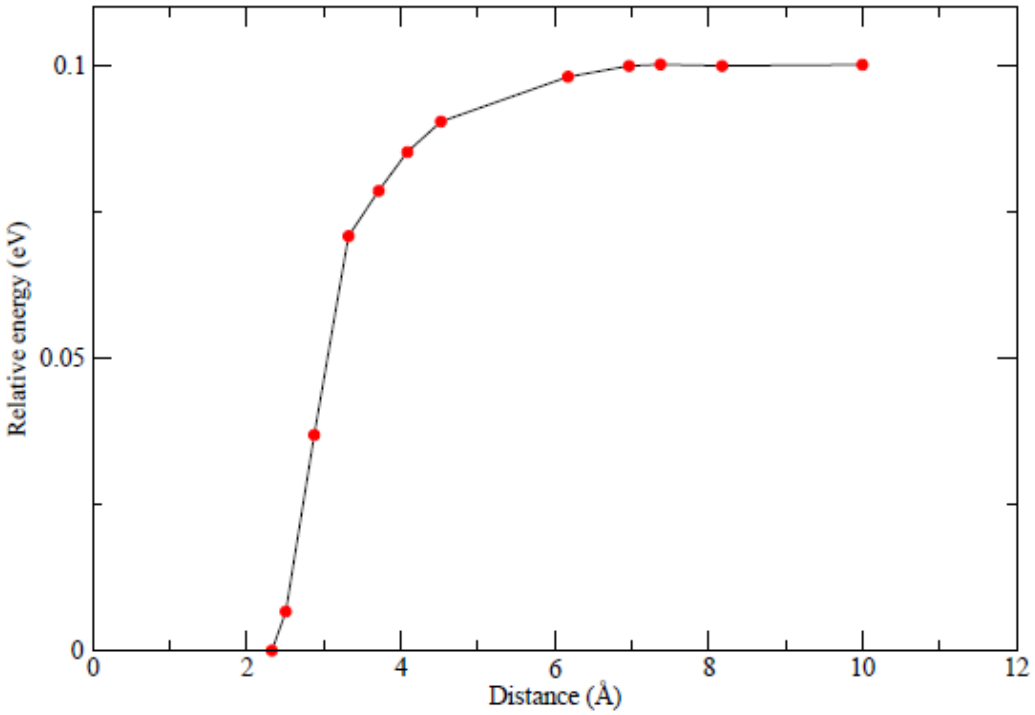

Figure 3.9 The desorption energy curve of one hydrogen molecule desorbed from ZnO sheet [99].

The above calculations of adsorption are performed at zero temperature. In fact, hydrogen uptake at room temperature and moderate pressure is of more practical interest. Because of this, we estimated the hydrogen uptake on single ZnO sheet at finite temperature and pressure through our continuum gas adsorption model. Ideally, the adsorption energy E_{ads} would be mapped out at all locations above the ZnO sheet, to provide a full H_2 density profile near the sheet. This would require a very large number of calculations, which is challenging for DFT calculations. To provide a simpler estimate, we assumed that the adsorption energies of different configurations vary with distance D from the ZnO sheet in a manner similar to Figure 3.8 scaled by their respective binding energies. We generated curves for different positions along the lattice by rescaling the energy curves of Figure 3.9 by a factor E/E_{min}. Here E is the binding energy from Figure 3.8, and E_{min} = 0.137 eV/molecule is the strongest binding energy.

The contribution of each different configuration to the total adsorption was evaluated as following. We considered four distinct types of adsorption sites in a ZnO unit cell. One was above an O atom (Figure 3.9, configuration I) with a binding energy of -0.131 eV. The second site was above a Zn atom (Figure 3.9, configuration II and V) with an average binding energy of -0.076 eV. The third one was above the middle of six-ring hollow, represented by configuration VI, VII, and VIII (Figure 3.9) with an average energy of -0.104 eV. The fourth site was above the Zn-O bond, as shown in configuration III and IV of Figure 3.9, with binding energy of -0.137 eV. The contribution of each type of adsorption sites was estimated by their weights in a unit cell. For example, there was one O atom, one Zn atom, one six-ring, and three Zn-O bonds.

Thus, the contribution was 1/6, 1/6, 1/6, 1/2 for O atom, Zn atom, six member ring, and Zn-O bond, respectively.

The total hydrogen uptake was integrated up to distances of 10 Å. For both sides of the sheet, the total uptake was calculated to be in the range 2.0-2.6 wt% at 298K, 5MPa, depending on the details of the assumed scaling behavior. Since the total uptake will continue to increase with the integration distance D, the excess uptake is a better parameter to evaluate the adsorption effects. The excess uptake was calculated by subtracting the total uptake by the mass of the gas that would have occupied the same volume without adsorbent-adsorbate interaction. For both sides of ZnO sheet, the excess uptake is 1.5 - 2.1 wt% at 298 K, 5 MPa. This suggests ZnO sheets are promising to meet the U.S. DOE target for hydrogen storage. Our previous work in Chapter III on the expanded graphite model showed that our method slightly but systematically underestimated the adsorption compared to more detailed methods, indicating a possibly higher adsorption capacity on ZnO than indicated here. It should be noted that in experiment, only one side of the ZnO sheet is accessible to hydrogen since the ZnO sheet was grown on Ag (111) substrate. The accuracy of van de Waals interaction calculated by DFT should be also carefully considered. Further discussions on van de Waals interaction potential calculation are presented in Chapter VI. Our encouraging adsorption results may motivate advanced experimental method developments in the future to synthesize free-standing ZnO membranes.

3.4 Method Limitations

As mentioned before, the validity of the EOS and the quantum effects of adsorbed hydrogen should be considered, especially for high pressures or low temperatures. In this section, we discuss the limitations of the present approach and provide some estimation on the quantum effects in this method.

First of all, the accuracy of the empirical C-H_2 potential is the most important limitation of this approach, since the hydrogen uptake is shown to be very sensitive to the selected potential in the expanded graphite model. The drawbacks to the simplified interactions here, and the difficulties of accurately calculating the van der Waals interaction using DFT approaches, are well known[108-109]. For example, the Patchkovskii potential used here does not accurately predict the corrugation of the H_2 adsorption energy on the coronene molecule, as noted in the original work.

Even assuming that the C-H_2 interaction is acceptably accurate, there are important points to note about the approach presented in this work. One of these is the limitations of the EOS. The valid range of Mills EOS used in this dissertation is 75-307K and 2,000-20,000 bar. We notice that the effective internal pressure in amorphous carbon can be very high in certain places, due to the large adsorption energies. For example, the strongest adsorption energy in one of our calculated structures with a density of 1.25 g/cm^3 is -0.21 eV/molecule, as calculated by using Patchkovskii *et al.* potential. The

corresponding internal pressure in that region is calculated as 17,000 MPa for an external pressure of 5 MPa and temperature of 298 K. This effective pressure is beyond the validity range of Mills equation of state and a better EOS should be applied. However, the contribution of these high density regions to the total H_2 adsorption is actually small, less than 10% over the total adsorption. In such cases, a rough estimation of adsorption can be still obtained by Mills EOS even though an accurate EOS for high pressures is required in future studies. At room temperature, the empirical Mills EOS is essentially equal to the ideal gas EOS at very low pressures. Further comparisons show that the Mills EOS followed Kammerlingh-Onnes empirical EOS up to 1000 bar.[110] Thus, we assume that the Mills EOS can be reasonably extended below 2000 bar at room temperatures. A more reliable equation of state for hydrogen below 2000 bar[82] will certainly increase the accuracy of the calculations but will not make a large difference. Due to the lack of details in reference[82], the improved equation of state is not used in the current work.

The thermal de Broglie wavelength (Λ) or de Broglie density ($\rho_0 \equiv 1/\Lambda^3$) provides a criterion to roughly determine the upper boundary of the regime with significant quantum effects. If the thermal de Broglie wavelength is much smaller than the inter-particle distance or the de Broglie density is much larger than the gas density, the gas can be considered as a classical gas. Otherwise, quantum effects will dominate and the gas should be treated carefully as a Bose or Fermi gas. The thermal de Broglie wavelength

$$\Lambda = \frac{h}{\sqrt{2\pi m k_B T}}, \tag{3.20}$$

where h is Planck's constant, m is the molecule mass and k_B is Boltzmann's constant, for an H_2 molecule at room temperature is calculated to be close to Λ=0.7 Å, corresponding to a number density of 3.0 $Å^{-3}$. Our calculations showed that the number densities of adsorbed H_2 in amorphous carbons are much less than 0.1 $Å^{-3}$, about an order of magnitude smaller than the calculated de Broglie density (ρ_0) at room temperatures. This supports the validity of the classical treatments to the adsorbed hydrogen under these conditions.

To provide some idea on the conditions where the quantum effects will be important based on a de Broglie density analysis, we calculated the hydrogen density as a function of temperature and internal pressure by Mills EOS in its validity region (200<P<2000 MPa and 75<T<307 K). Compared with the de Broglie densities (ρ_0) at the corresponding temperatures, the hydrogen densities are found always less than the de Broglie densities, indicating that the hydrogen liquid may be treated classically in the validity region of Mills EOS. Note that in hydrogen adsorption, the internal pressure on the adsorbed hydrogen can be much higher than 2000 MPa due to the attractive force field of the adsorbents. Due to the lack of a valid EOS for higher pressures, we cannot provide an accurate estimate beyond 2000 MPa. We also show the density contour for several fractions of $\rho_0 \equiv 1/\Lambda^3$ in Figure 3.10. For example, for any (T,P) below the red curve, the corresponding Mills density is less than 0.1 ρ_0 at the same temperature. This

figure demonstrates that at room temperatures the quantum effects can be neglected for internal pressures up to 2000 MPa since the hydrogen density is one order of magnitude less than the de Broglie density.

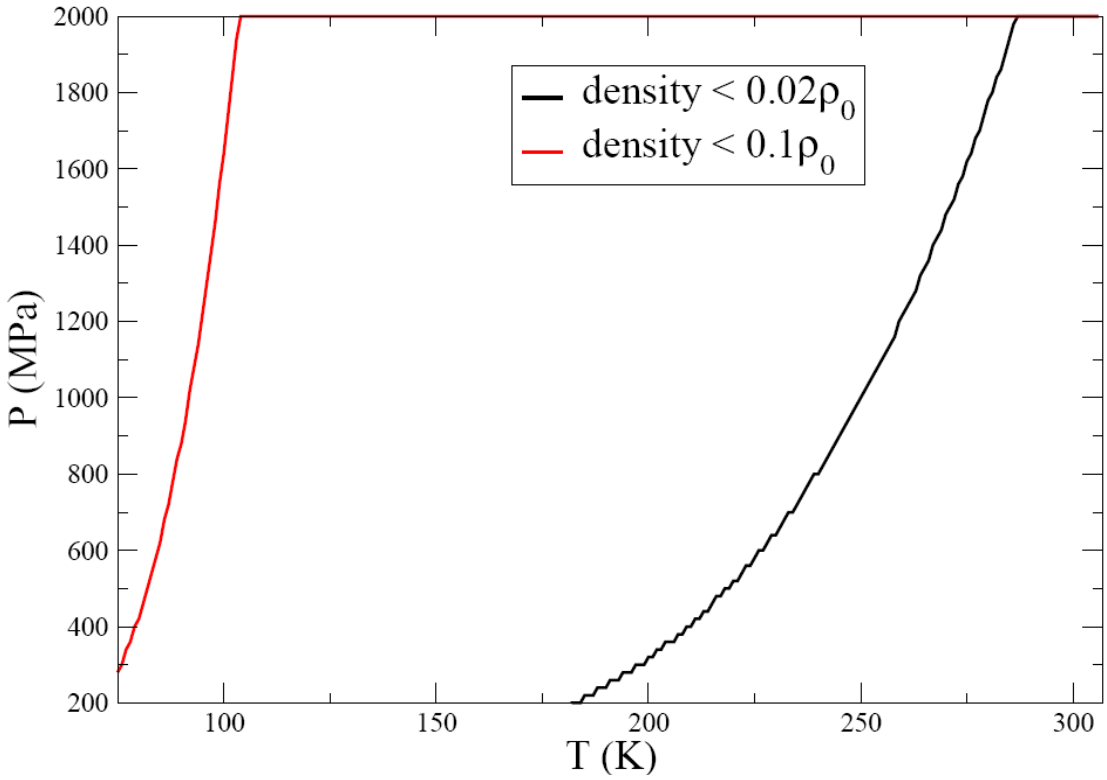

Figure 3.10 The density contours for several fractions of the de Broglie density ρ0≡1/Λ3 (which sets the density scale at which quantum effects are expected to become important). For any (*T,P*) below the red curve, the predicted density is less than 0.1 ρ_0 at the same temperature. For any (*T,P*) below the black curve, the predicted density is less than 0.02 ρ_0 at the same temperature.

To better demonstrate that the current method approaches Patchkovskii's method in the classical limit, we discuss the adsorption problem in a cubic box, as a simple model of adsorption in a pore. By comparing the results calculated by Patchkovskii's method and our method, we quantitatively show the upper limits of quantum effects in our method. Patchkovskii *et al.* used the ideal gas approximation to calculate the free energies of adsorption, which already assumes that the gas density is less than the thermal de Broglie density ($\rho_0 \equiv 1/\Lambda^3$). Equivalently, the assumption is that the occupancy of any quantum state is much less than one. Similarly, we considered a single molecule in the box of volume $V=L^3$. The potential energy is defined as E_{ads} inside the box and positive infinite outside the box, modeling a pore with some average adsorption energy. Following the Patchkovskii *et al.* method, the canonical partition function for adsorbed gas q_{ads} is

$$q_{ads} = \exp(-\frac{E_{ads}}{k_B T}) \sum_{n_x} \sum_{n_y} \sum_{n_z} \exp\left(-\frac{\hbar^2 \pi^2}{2mL^2 k_B T} \left(n_x^2 + n_y^2 + n_z^2 \right) \right) \tag{3.21}$$

where n_x, n_y, n_z can be any positive integers. The canonical partition function for free gas q_{free} is

$$q_{free} = \frac{V}{\left(2\pi\hbar^2 / mk_B T \right)^{3/2}} = \frac{V}{(\Lambda)^3} \tag{3.22}$$

The effective internal pressure P_{int} is given by

$$P_{\text{int}} = K_{eq} P_{free} \tag{3.23}$$

where $K_{eq} = \frac{q_{ads}}{q_{free}}$. Comparing with equation (3.4), K_{eq} equals $\exp(-\frac{E_{ads}}{k_B T})$ in our method. Assuming $E_{ads} = -0.10\,eV$, Table 3.2 lists the values of K_{eq} as a function of box size (L) and compares K_{eq} with $\exp(-\frac{E_{ads}}{k_B T})$. In this simple cubic box model, our method consistently overestimates the internal pressure and thus the gas adsorption compared to Patchkovskii method. At large box size (or equivalently small particle density $\frac{1}{V}$) limit, our method approaches the results using the Patchkovskii method. However, the small density limit and the ratio of $K_{eq} / \exp(-\frac{E_{ads}}{k_B T})$ may vary in different geometries.

Table 3.2 The values of K_{eq} as a function of box size, calculated using the approach of Patchkovskii, and the comparisons between K_{eq} and $\exp(-\frac{E_{ads}}{k_B T})$ at T=298K. E_{ads} is set as -0.10 eV. The de Broglie wavelength is 0.7 Å.

$\rho = \frac{1}{V}$ (Å^{-3})	K_{eq}	$\exp(-\frac{E_{ads}}{k_B T})$	$K_{eq} / \exp(-\frac{E_{ads}}{k_B T})$
1.0	104.83	49.0544	2.1370
0.037	68.1365	49.0544	1.3890
0.001	54.525	49.0544	1.1115
1×10^{-6}	49.6185	49.0544	1.0115

3.5 Conclusion

In this chapter, we introduced an effective method to calculate the hydrogen storage capacities in expanded graphite and amorphous carbons at room temperature and moderate external pressures. The key of this method is to treat the adsorbed gas classically and calculate the adsorbed gas density by the empirical equation of state. This method reproduces the equilibrium hydrogen uptake in expanded graphite of GCMC and Patchkovskii *et al.* calculations. The hydrogen uptake is shown to be sensitive to the selected empirical C-H_2 potential. The expanded graphite with width of 6.5 Å could reach a gravimetric capacity of 2 wt% at room temperature and 5 MPa. Carbon materials with nanopores of an average width of 6.5 Å may be promising for hydrogen storage applications. The calculations demonstrate that optimizing the material to maximize the energy of adsorption does not necessarily optimize uptake: the volume available for uptake with low energies of adsorption must also be considered. The calculations of the isosteric heat for hydrogen adsorption, derived from a virial equation analysis, are consistent with numerical calculations based on the thermodynamical analysis. This model predicts that hydrogen uptake is close to 0.5 wt% in amorphous carbons (1.25 g/cm^3) at room temperature and 5 MPa. While not reaching Department of Energy goals, this is a significant value at these temperatures, particularly considering that the structure has not been adjusted in any way to improve the uptake. Over the density ranges examined, total hydrogen adsorption can be improved by increasing the volume available

for adsorption. With the cooperation with Si et al., we also predict the hydrogen adsorption on both side of ZnO sheet. The binding energy of H_2 with ZnO sheet is calculated by the density functional theory by Si et al. Our work predicts that the excess uptake as 1.5 -2.1 wt% at 298K, 5 MPa on ZnO sheet. We also carefully discuss the limitations of this method and find at room temperatures, quantum effects can be neglected for internal pressures up to 2000 MPa. It is shown that our method approaches Patchkovskii method in the classical limit.

CHAPTER IV

AMORPHOUS CARBON BY TIGHT BINDING SIMULATION

The purpose of this chapter is to generate and characterize accurate amorphous carbon structures using tight binding molecular dynamics simulations. Even though increasing computational capacities encourage simulation investigations, the requirements on a physically reasonable atomic-scale simulation of activated carbon produced from raw materials are still enormous. In this study, we generate amorphous carbons by quenching molten carbon to room temperature. Our method does not intend to mimic the production of such materials, but to generate amorphous structures in order to study their topological and gas adsorption properties. We hope to establish the relationship between gas adsorption and carbon microstructure in atomic level. By tracing the atom trajectories driven by the inter-atomic forces, molecular dynamics simulation can provide information on kinetic and structural properties of system. The atomic interaction potential is critical for this method. Many different methods have been used to describe the interaction between carbon atoms, from first principle calculation, through tight binding approximation, to classical potential methods. As the most accurate and reliable method, first principle calculations have been used to investigate the structures and electronic properties of liquid carbon as well as quenched amorphous carbon.[111-113] Due

to the heavy computational demand of first principle calculations, the system size and the simulation time are limited. Empirical potentials such as Tersoff, Brenner and the reaction state summation scheme (RSS)[92, 114-115] have been widely applied in various carbon simulations. They provide fast description of structure energy by using fitted functional forms and parameters. However, the accuracy is limited due to the classical nature of empirical potentials and the lack of quantum effects in bonding. An alternative approach for evaluating C-C bonding energy is the tight binding approximation. A tight binding potential uses a linear combination of atomic orbitals to approximate the electronic structures, thus is more accurate than empirical potentials. As it does not consider the full set of wave functions, it is also faster than the first principle calculations. In the first section of this chapter, we describe the molecular dynamics simulation program based on a tight binding model. The detailed analysis of the simulation results are presented in the second part.

4.1 Tight Binding Simulation Program Development

We use the transferable tight-binding potential developed by Xu et. al.[116] for carbon systems. It represents the quantum mechanical nature of the covalent bonding by considering the *s* and *p* orbital hybridization. By directly incorporating bonding information, tight binding provides a better description of structural, dynamical, and electronic properties of carbons then typical classical empirical potentials. This tight binding model has correctly predicted that the graphite energy is lower than that of

diamond, while the widely used empirical Tersoff potential predicts the opposite. The torsion effects in carbon bonding, which are missed in the Tersoff potential, are taken into account in tight binding energy calculation in a natural way through a correct description of orbital hybridization and double bond formation. The tight binding model by Xu et al. has been successfully applied to various carbon structures including buckyballs, amorphous carbon, and liquid carbon.[117-121]

In this model, the total potential of the system can be written as:

$$E_{tot} = E_{bs} + E_{rep} \tag{4.1}$$

where E_{bs} is the electronic band structure energy and E_{rep} is the repulsive energy between ions. E_{bs} can be expressed as,

$$E_{bs} = \sum_{n}^{occupied} \langle \psi_n \mid H(\{r_i\}) \mid \psi_n \rangle \tag{4.2}$$

where H is the empirical tight-binding Hamiltonian matrix, and ψ_n is the eigenvector for H. Only the energies of occupied states are counted in Eq. (4.2). The elements of the Hamiltonian matrix H can be described by a set of parameters, such as isolated atomic orbital energies (E_s, E_p) and two-centered hopping parameters ($V_{ss\sigma}, V_{sp\sigma}, V_{pp\sigma}, V_{pp\pi}$), that lead to hybridized electronic states. The two-centered hopping parameters ($V_{ss\sigma}$, $V_{sp\sigma}, V_{pp\sigma}, V_{pp\pi}$) are scaled by the distance between two atoms and primarily fitted through the first principle LDA results of different carbon polytypes. The parameters are

chosen as: $E_s = -2.99eV$, $E_p = 3.71eV$, $V_{ss\sigma} = -5.0eV$, $V_{sp\sigma} = 4.7eV$, $V_{pp\sigma} = 5.5eV$ and $V_{pp\pi} = -1.55eV$. The parameters $V_{ss\sigma}$, $V_{sp\sigma}$, $V_{pp\sigma}$, and $V_{pp\pi}$ are scaled by function *s(r)*.

$$s(r) = (r_0 / r)^n \exp\{n[-(r / r_c)^{n_c} + (r_0 / r_c)^{n_c}]\} \tag{4.3}$$

where *r* is the interatomic distance. n=2.0, n_c=*6.5,* r_c=*2.18* Å, r_0=*1.536329* Å, and r_1=2.45 Å. To make the scaling function *s(r)* go to zero smoothly at some designated cut-off distance, the tail of *s(r)* is replaced with a third-order polynomial $t_s(r - r_1)$. The coefficients of $t_s(r - r_1)$ are given in Table 4.1

In a system containing *N* atoms, the Hamiltonian matrix can be written as,

$$H = \begin{pmatrix} H_{00} & H_{01} & \dots & H_{oN-1} \\ H_{10} & H_{11} & \dots & H_{1N-1} \\ \dots & \dots & \dots & \dots \\ H_{N-10} & H_{N-11} & \dots & H_{N-1N-1} \end{pmatrix}_{4N \times 4N} \tag{4.4}$$

Each H_{ij} is a 4x4 matrix describing the *s* and *p* energies of an isolated atom or the overlap between these orbitals with those of different particles. Since the orbital overlap interaction length is on the order of angstroms, many elements in *H* will be zero. The eigenvalues and eigenstates are solved by diagonalizing the Hamiltonian matrix *H:*.

$$Hx = \lambda x \tag{4.5}$$

The repulsive energy E_{rep} is represented by the following form:

$$E_{rep} = \sum_i f\left(\sum_j \phi(r_{ij})\right) \tag{4.6}$$

where $\phi(r) = \phi_o (d_0 / r)^m \exp\{m[-(r/d_c)^{m_c} + (d_o/d_c)^{m_c}]\}$, $\phi(r_{ij})$ is a pairwise potential between atom *i* and *j*, r_{ij} is the distance between these two atoms. The parameters of $\phi(r_{ij})$ are: ϕ_o =8.18555eV, m=3.30304, m_c=8.6655, d_c=1.64Å, d_1=2.57Å. To make $\phi(r_{ij})$go to zero smoothly at some designated cut-off distance, the tail of $\phi(r_{ij})$is replaced by a third-order polynomial $t_\phi(r - d_1)$. Detailed parameters for $t_\phi(r - d_1)$ can be found in Table 4.1. $f(x) = \sum_{n=0}^{4} c_n x^n$ is a 4th order polynomial function with an argument of $x = \sum_j \phi(r_{ij})$. The coefficients of $f(x)$ can be also found in Table 4.1. Figure 4.2 shows our calculated potential energy vs. the nearest neighbor atomic distance for different carbon structures (linear chain, graphene, diamond, and simple cubic carbon), in good agreement with Xu *et al.*[116] results. Graphene is slightly energetic favorable than diamond (ΔE=0.0292 eV/atom) in the tight binding model, while the empirical Tersoff potential predicts that diamond is more stable by *-0.0623eV/atom*.

Table 4.1 Coefficients of the polynomial functions $t_s(r-r_1)$, $t_\phi(r-d_1)$, and $f(x)$ [116].

	$t_s(r-r_1)$	$t_\phi(r-d_1)$	$f(x)$
c_0	$6.7392620074314\times10^{-3}$	$2.2504290109\times10^{-8}$	-2.5909765118191
c_1	$-8.1885359517898\times10^{-2}$	$-1.4408640561\times10^{-6}$	0.5721151498619
c_2	0.1932365259144	$2.1043303374\times10^{-5}$	$-1.7896349903996\times10^{-3}$
c_3	0.3542874332380	$6.6024390226\times10^{-5}$	$2.3539221516757\times10^{-5}$
c_4			$-1.24251169551587\times10^{-7}$

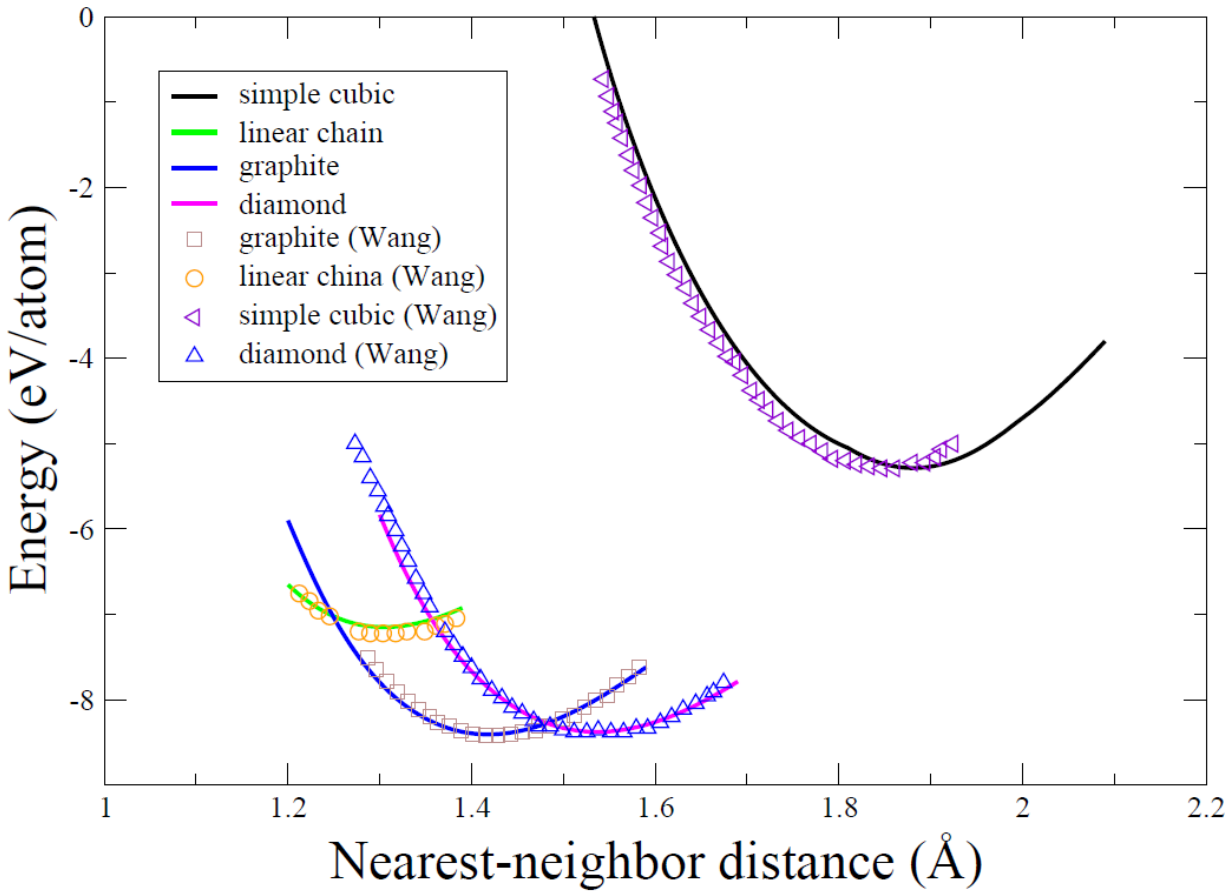

Figure 4.1 The potential energy per atom calculated as function of nearest neighbor distance in linear chain, graphite, diamond and simple cubic carbon. The solid curves are from our calculations. Wang *et al.* data are extracted from Figure 2 of reference[116].

The forces imposed on each atom arising from electronic band energy are calculated utilizing the Hellmann-Feynman theorem, by multiplying derivatives of the matrix *H* and its eigenvectors.

$$F_x^{\ i} = -\sum_{n \in occupied} \left\langle \Psi_n \left| \frac{\partial H}{\partial x_i} \right| \Psi_n \right\rangle$$
$$F_y^{\ i} = -\sum_{n \in occupied} \left\langle \Psi_n \left| \frac{\partial H}{\partial y_i} \right| \Psi_n \right\rangle$$
$$F_z^{\ i} = -\sum_{n \in occupied} \left\langle \Psi_n \left| \frac{\partial H}{\partial z_i} \right| \Psi_n \right\rangle \qquad (4.7)$$

F_x^i, F_y^i, F_z^i are the force components of atom *i* at x, y, z direction, respectively. At zero temperature, for carbon, only the lowest half of the energy states are occupied by the electrons. The forces arising from repulsive energy between ions are directly calculated by the negative gradient of E_{rep}.

Based on the above tight binding model, we have developed a large scale parallel program for molecular dynamics simulation. The temperature is simply controlled by rescaling the velocities of atoms. Since we focus on the structures of amorphous carbons at room temperature instead of the thermodynamics properties, this simple treatment of temperature is considered sufficient comparing to more careful methods (e.g. Nosé-

Hoover thermostat). The Leap Frog algorithm is used to integrate Newton's equation of motion. The new positions based on the old positions and velocities are:

$$r(r+\Delta t) = r(r) + v(t)\Delta t + \frac{f(t)}{2m}\Delta t^2 \tag{4.8}$$

and the updated velocities are:

$$v(t+\Delta t) = v(t) + \frac{f(t+\Delta t) + f(t)}{2m}\Delta t \tag{4.9}$$

where $r(t)$ and $v(t)$ are the position and velocity at time t, respectively. Δt is the time step, f is the force and m is the mass. This algorithm only allows calculating the velocities after the new positions are calculated.

The computational effort for diagonalizing the Hamiltonian matrix *H* scales as the cube of the system size, and the memory usage scales as the square of the system size. To improve the program performance, a high-performance linear algebra library ScaLAPACK was utilized for solving the eigenproblem of matrix *H*. A high performance scientific computer (Franklin) at National Energy Research Scientific Center (NERSC) was utilized for performing the simulations. ScaLAPACK is designed for distributed memory parallel computers and based on block-partitioned algorithms, in order to minimize the frequency of data movement between different levels of the memory hierarchy. In our codes, the matrix *H* is generated on the head node, and partitioned into blocks which are later mapped to the process grid. To achieve the best

performance for matrix with a given size, we have experimented with different ways to partition the matrix and create the process grid. Figure 4.2 shows the speed up utilizing ScaLAPACK comparing to LAPACK for calculating all eigenvalue-eigenvector pairs in a matrix with size of 8192x8192. ScaLAPACK is much faster than LAPACK since it uses more than one processor. Different ways of mapping the matrix have significant effects on the final performance. Using more processors will lower the work load of each processor but increase the communication between nodes, which eventually makes the performance drop. We also have to compromise between the competing needs of increasing program performance and reducing the computer resources usage.

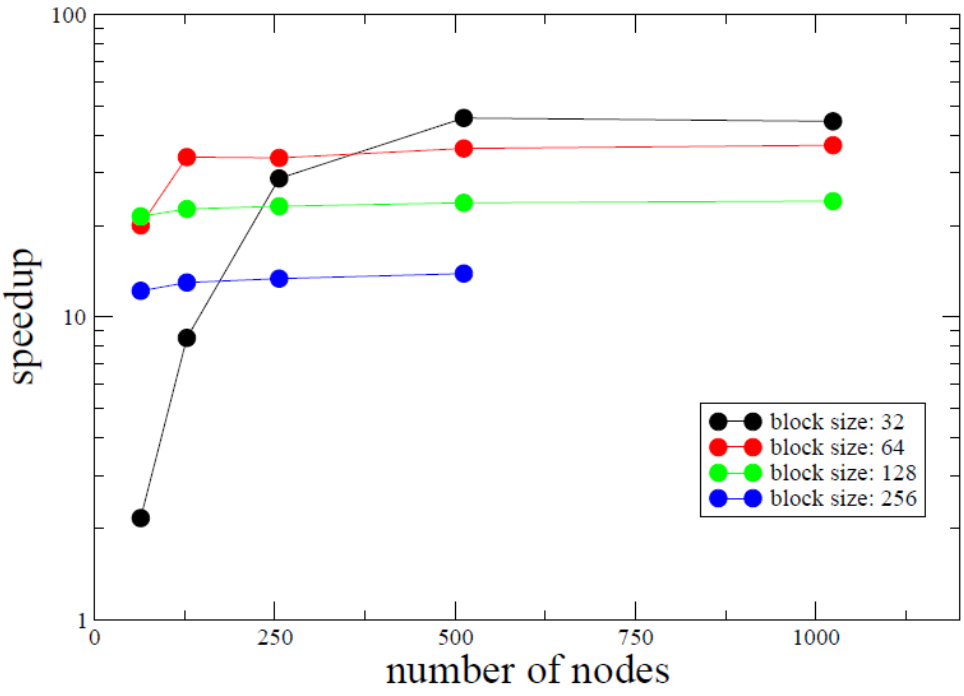

Figure 4.2 Performance speed up vs. number of processors in ScaLAPACK compared to LAPACK in matrix of size 8196x8196. Block sizes are 32x32, 64x64, 128x128, 256x256, respectively. Process grid is created as $\sqrt{N} \times \sqrt{N}$ where N is the total number of nodes. The calculations are performed at Franklin of NERSC.

4.2 Amorphous Carbon Structure Analysis

To generate amorphous carbon structures, we equilibrated various liquid carbon structures at 6000K and quenched them to 300K. The system volume was kept constant during the simulation. The temperature was simply controlled by rescaling the velocities of atoms. 500 atoms were used in a cubic cell and the periodic boundary condition is applied. The carbon "bulk" density was calculated by using the mass of the atoms and the volume of the unit cell. As will be explained later, this density is often not directly used by the carbon community. The bulk density ranges from 0.6 g/cm^3 (0.03 atom/Å^3) to 2.4 g/cm^3 (0.1204 atom/Å^3) in our studies. The MD time step was 1.0×10^{-15} s. Two different quenching rates (0.5 K/fs and 0.1 K/fs) were applied in simulations for comparison. These quenching rates are slower than, or comparable to, prior work utilizing similar potentials[94, 118, 122]. Further analysis (later in this chapter and in the subsequent chapter) shows that different simulation quenching rates can have distinct porous structures and gas uptake properties. After the quench, the samples were allowed to equilibrate with constant energy for 4000 time steps with a temperature near 300 K. The calculated structural properties were averaged over 2000 time steps, which were considered long enough for the (primarily structural) properties we are interested in. For better statistics, we have performed multiple independent simulations for each carbon density and quenching rate.

Figure 4.3 shows representative resultant amorphous carbon structures with different carbon bulk densities in the simulations. All of the structures shown in this figure are obtained from the simulations using lower quenching rate (0.1 K/fs). All carbon atoms and neighboring C-C bonds in the unit cell are shown in the figure. Graphitic segments are clearly observed for every density. At lower carbon densities, curved and twisted graphene sheets dominate the structures. At higher carbon densities, fragments of graphene sheets are roughly parallel to each other, forming networks with preferred orientations. High resolution microscopic images of UMC[123] revealed thin buckled graphene layers and crumpled graphene sheets on the edge of the samples, consistent with the simulation results. The atomic figures show that a large number of five-member rings and seven-member rings are formed to compensate the curvature of the graphene sheets in lower carbon density structures. High energy isolated atoms and linear chains are found due to the fast quenching and short equilibrium time in our simulations.

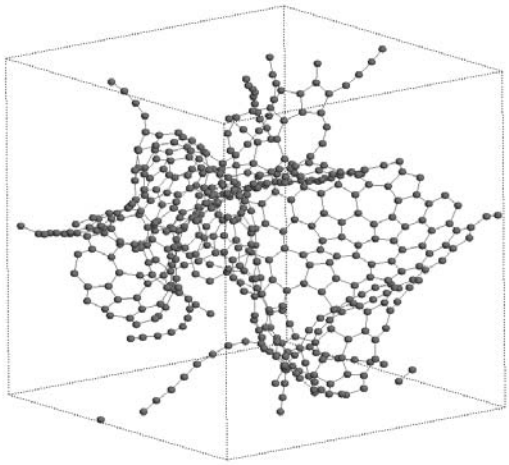

(a) 0.6 g/cm^3

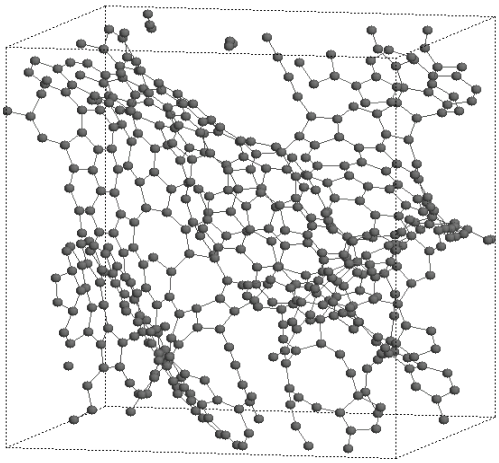

(b) 0.8 g/cm^3

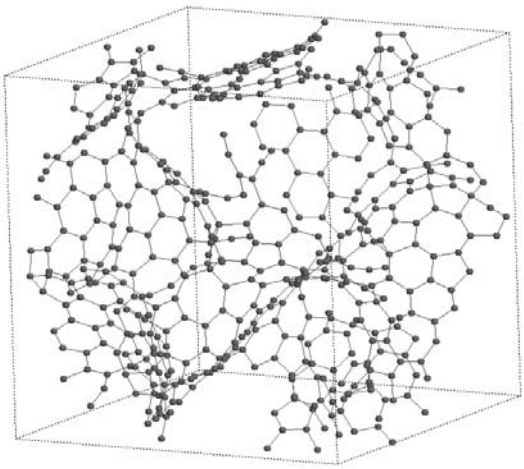

(c) 1.0 g/cm^3

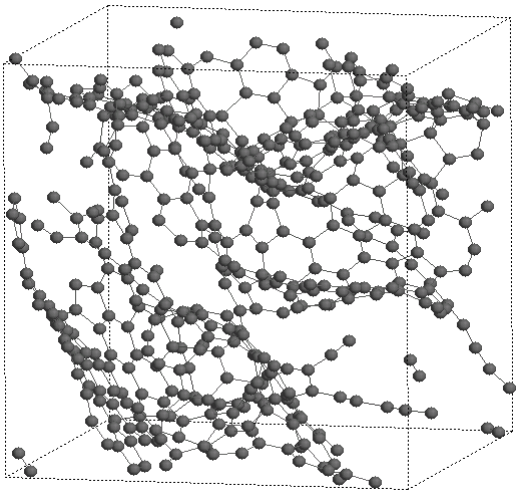

(d) 1.25 g/cm^3

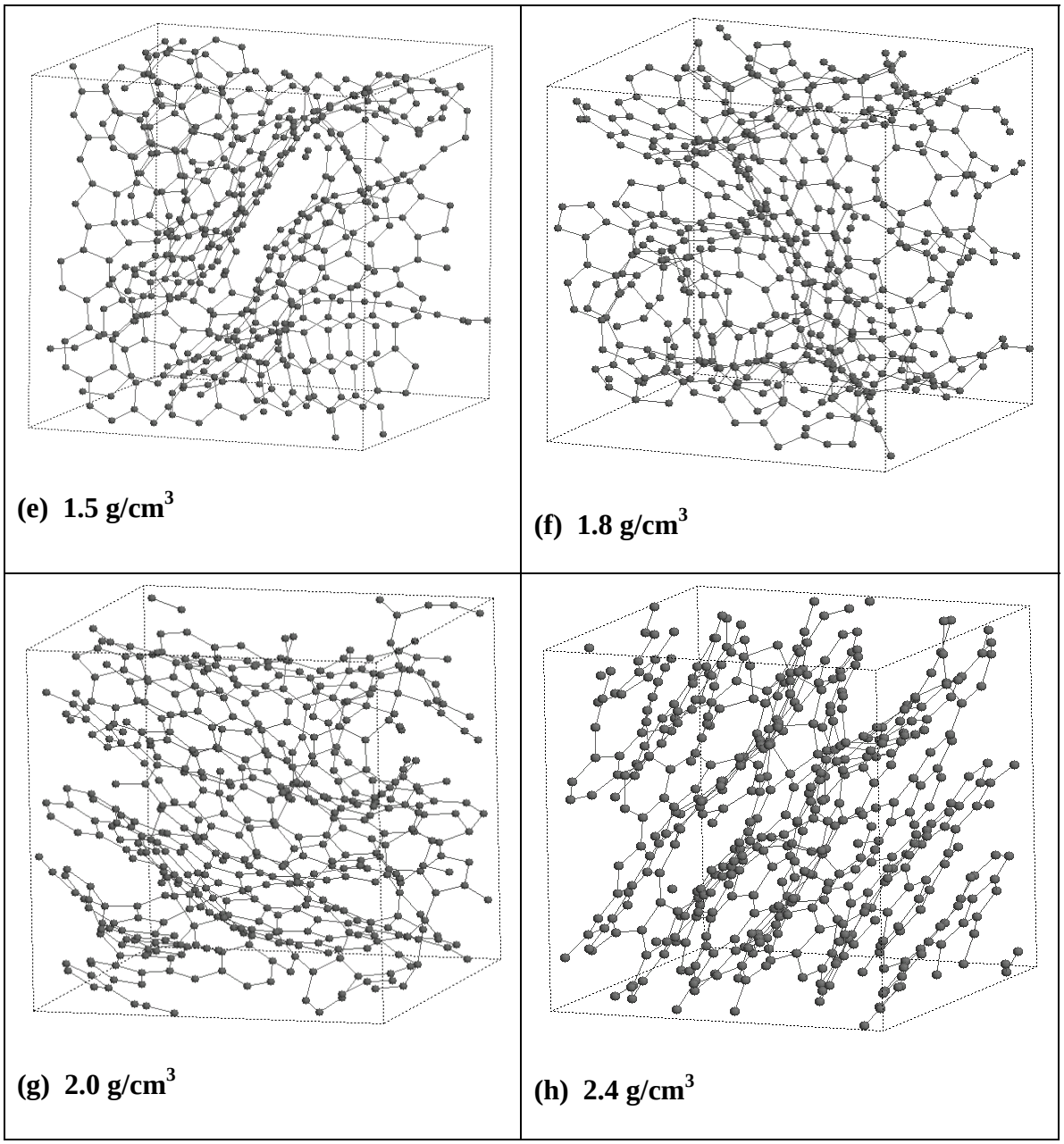

Figure 4.3 Atomistic pictures of the amorphous carbon structures with density of 0.6 - 2.4 g/cm3. All 500 atoms in the simulation unit cell are plotted. Structures are generated by quenching rate of 0.1 K/fs.

In Figure 4.4 we compare the pair distribution functions G(r) for amorphous carbon structures from Figure 4.3 with the experimental data from wood-based activated carbons.[123] The agreement is good, especially regarding the position of the first peak around 1.42 Å close to the graphite nearest neighbor distance. A sharp side peak at smaller distances, around 1.25 Å, is not observed in the experimental G(r) compared here. This is due to the presence of a significant number of one-fold and two-fold bonded atoms in the simulations. Comparing G(r) from different quenching rates (not shown in the figure), we find that the side peak around 1.25 Å is stronger in the structures generated by higher quenching rate, indicating more one-fold and two-fold bonded atoms. The second main peak around 2.44 Å in simulated G(r) is slightly shifted towards smaller distances compared to the experiment. There is a third main peak around 2.8 Å from experimental G(r) which is related[124] to the six-member ring in graphene sheets. This peak is also observed in our simulations but weaker for some simulated structures. This is due to the presence of large amount of five-member and seven-member rings in the structures. Galli et al.[111] using ab initio simulations quenched the systems with 54 carbon atoms and a density of 2.0 g/cm^3. They obtained the first peak at 1.44 Å and the second peak at 2.56 Å, close to our values. A hump between 2.6 and 3.2 Å was also shown in their g(r) function, indicating the evidence of the third peak. Shi[114] developed an empirical potential which eliminated sp^3 hybridization, making the formation of graphitic segments much more likely (at the expense of accurately modeling the energy of different structures). This potential was used to create quenched carbon systems with very low densities (0.038-0.058 atoms/Å^3). Some of his pair distribution functions for

the simulation structures were in good agreement with those from experiments of activated carbons (CS400, CS1000, CS1000a). The third peak was obvious in both simulations and experiments from Shi's paper. In contrast, previous tight binding studies[94, 122] for amorphous carbons with density between 1.20 g/cm^3 and 3.2 g/cm^3 have not shown evidence of the third peak. A detailed analysis shows that their structures have a smaller fraction of 3-folded atoms than ours, which means less graphitic fragments. Li and Lannin[125] obtained the radial distribution function by neutron diffraction on amorphous carbon film prepared by rf sputtering. Their sample density was estimated to be between 2.0 - 2.44 g/cm^3. However, their results did not show the third peak either. It suggests that the amorphous carbon structures with similar densities may be very different due to different preparation processes. In Figure 4.4, the positions of the fourth and fifth main peaks are slightly shifted towards to smaller distance compared to the experimental results, suggesting that the graphene sheets from our simulations have higher curvatures than those from experiments.

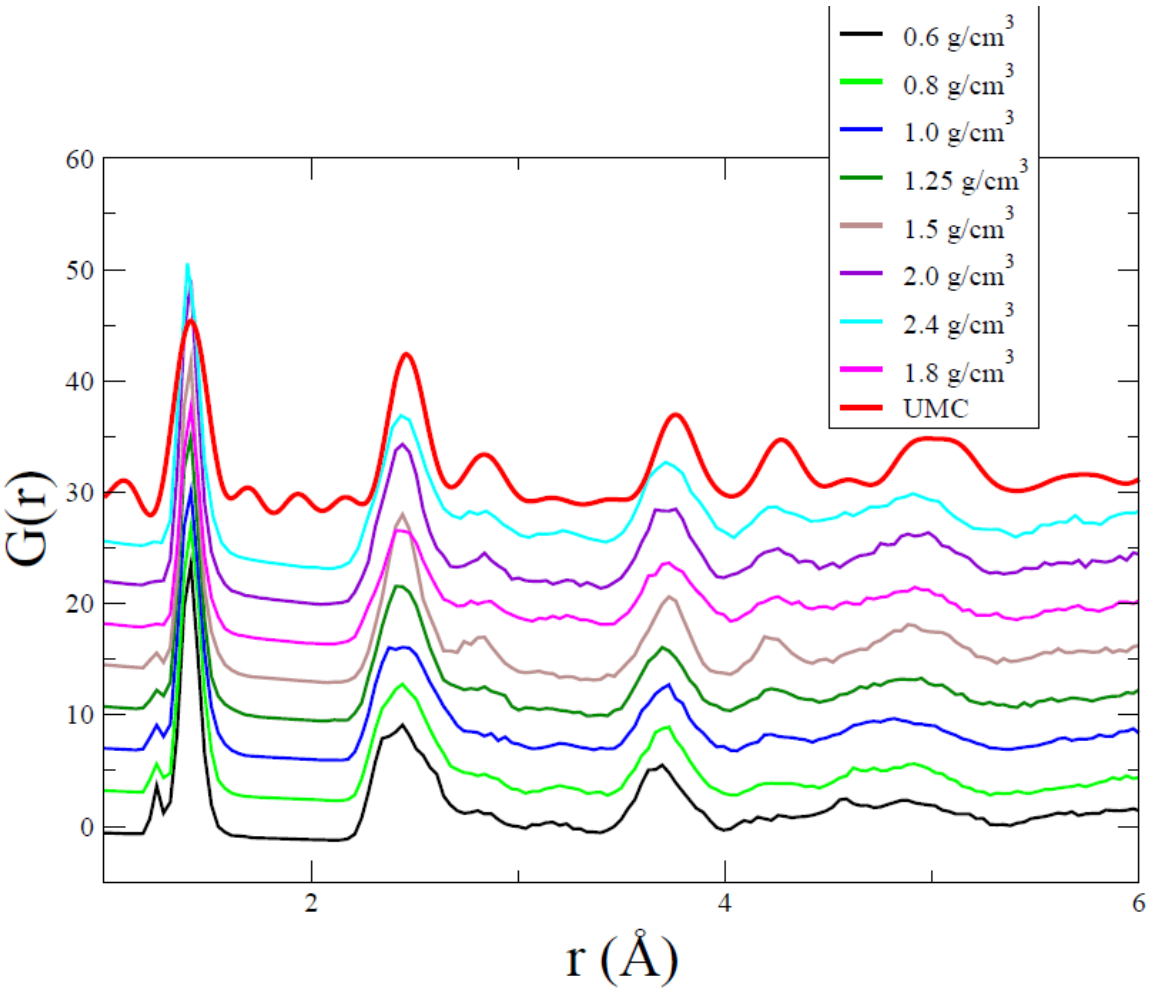

Figure 4.4 The pair distribution functions of simulations (a)-(f) included in Figure 4.3. The experimental data (red) is from the X-ray diffraction of UMC.[126]

For carbon structures, the description of the coordination (or, alternatively, sp^2 and sp^3 fraction) is a useful characterization of the structure. The cutoff distance used to define the coordination of atoms is determined in each case by the first minimum in the pair distribution function G(r) in Figure 4.4. Figure 4.5 shows that the numbers of three-fold and four-fold bonded atoms increase with increasing carbon bulk density. The population of three-fold bonded atoms changes from an average of 66% (carbon bulk density of 0.6 g/cm^3) to 92% (carbon bulk density of 2.4 g/cm^3) in Figure 4.5 (a). In contrast, the number of one-fold and two-fold bonded atoms decreases rapidly as the carbon bulk density increases. Comparing Figure 4.5 (a) with (b), it is clear that lower quenching rate generates fewer one-fold and two-fold bonded atoms, lowering the system energy, which will be demonstrated in Figure 4.6. A crossover between two-fold and three-fold bonding is found around 1.0 g/cm^3 with quenching rate of 0.5 K/fs, but absent in quenching rate of 0.1 K/fs. In contrast, Mathioudakis et al.[94] used two different quenching rates (0.226 K/fs and 0.500 K/fs) but did not find noticeable quenching rate effects in systems with 216 atoms. The mean coordination (N) as function of carbon bulk density is listed in Table 4.2. These results agree well with previous work on amorphous carbons by Wang et al.,[122] using the same tight binding model. However, compared to their results, our fraction of 3-folded atoms are slightly higher than their values and the values of 2-folded atoms are slightly lower. The difference can be explained by a much higher quenching rate (1 K/fs) used in Wang et al.'s simulations.

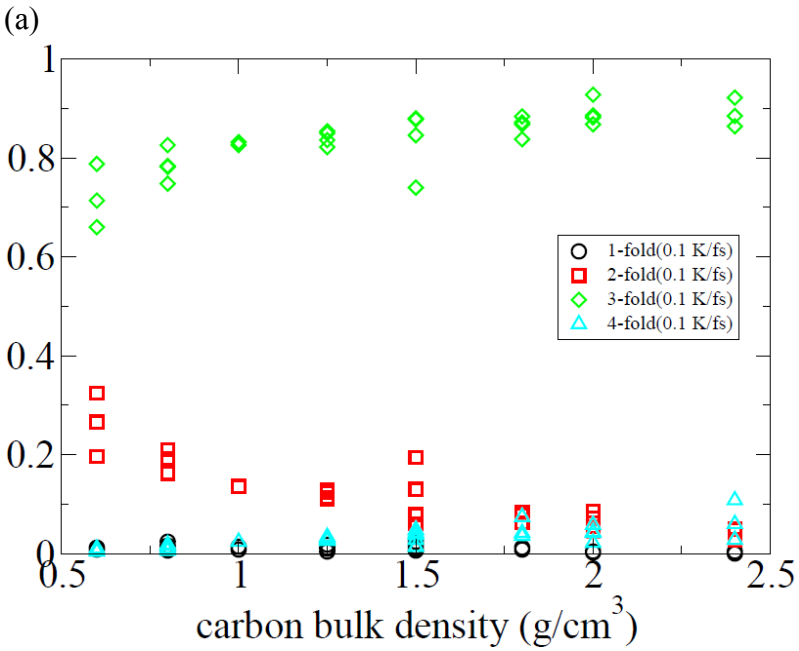

Figure 4.5 The portion of 1-fold, 2-fold, 3-fold, and 4-fold bonded atoms as a function of bulk density for temperatures near T =300K with (a) quenching rate of 0.1 K/fs and (b) quenching rate of 0.5 K/fs.

(b)

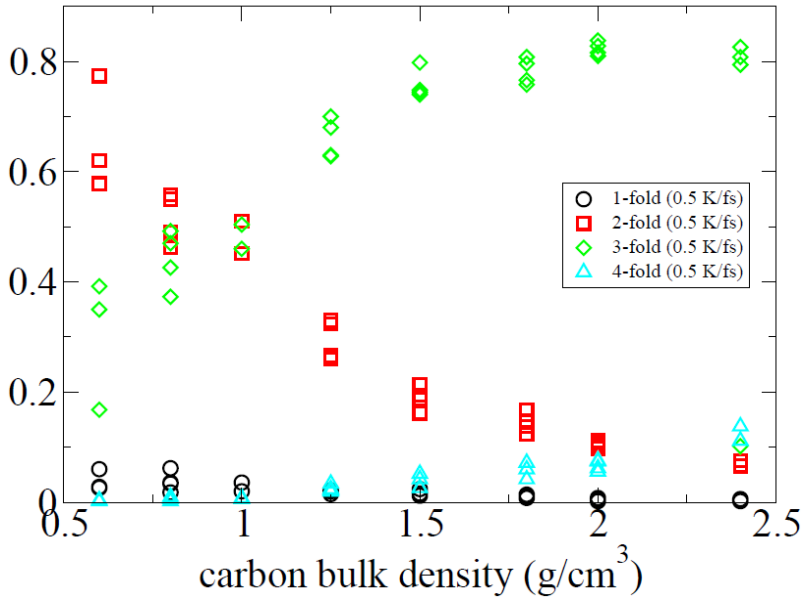

Figure 4.5 (continued)

Table 4.2: The mean coordination *N* as a function of carbon bulk density for different quenching rate (0.1 and 0.5 K/fs).

Bulk density (g/cm^3)	0.6	0.8	1.0	1.25	1.5	1.8	2.0	2.4
N (0.5K/fs)	2.3	2.4	2.5	2.7	2.8	2.9	3.0	3.0
N (0.1K/fs)	2.7	2.8	2.9	2.9	2.9	3.0	3.0	3.0

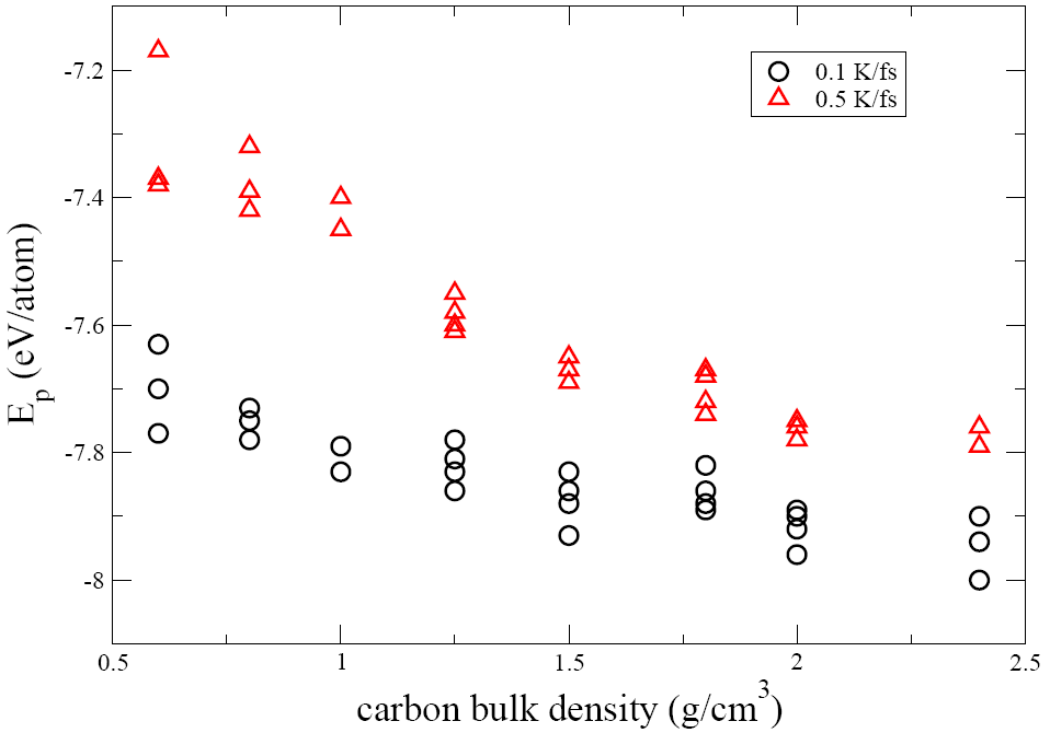

Figure 4.6 The averaged potential energy as a function of bulk density for temperatures near T=300K. Results with different quenching rates of 0.1 K/fs (black circles) and 0.5 K/fs (red triangles) are compared.

Figure 4.6 plots the carbon structure potential energy, averaged over 2000 time steps for each simulation, as a function of carbon bulk density at temperatures close to 300 K. Figure 4.6 indicates that lower quenching rate generates structures with lower potential energy. Figure 4.7 further demonstrates that the potential energy is correlated with the number of three-fold bonded atoms, independent of the quenching rate. The potential energy of the ground state graphene structure is -8.404 eV/atom. From Figure 4.6, there are only small energy differences among the carbon structures with densities between 1.5 g/cm^3 and 2.4 g/cm^3, suggesting that in larger amorphous structures, local density fluctuations are easy to achieve with little energy cost. For the bulk densities below 1.5 g/cm^3, large voids along with condensed regions are observed in the systems. This suggests that in these structures, the increase of potential energy can be understood by the energy of forming an interface between voids and the condensed areas. In larger amorphous carbon structures with similar densities, the systems will tend to form several large voids instead of many small voids, in order to decrease the area of interface. Therefore, the simulation size effects are expected to be more significant at lower bulk densities.

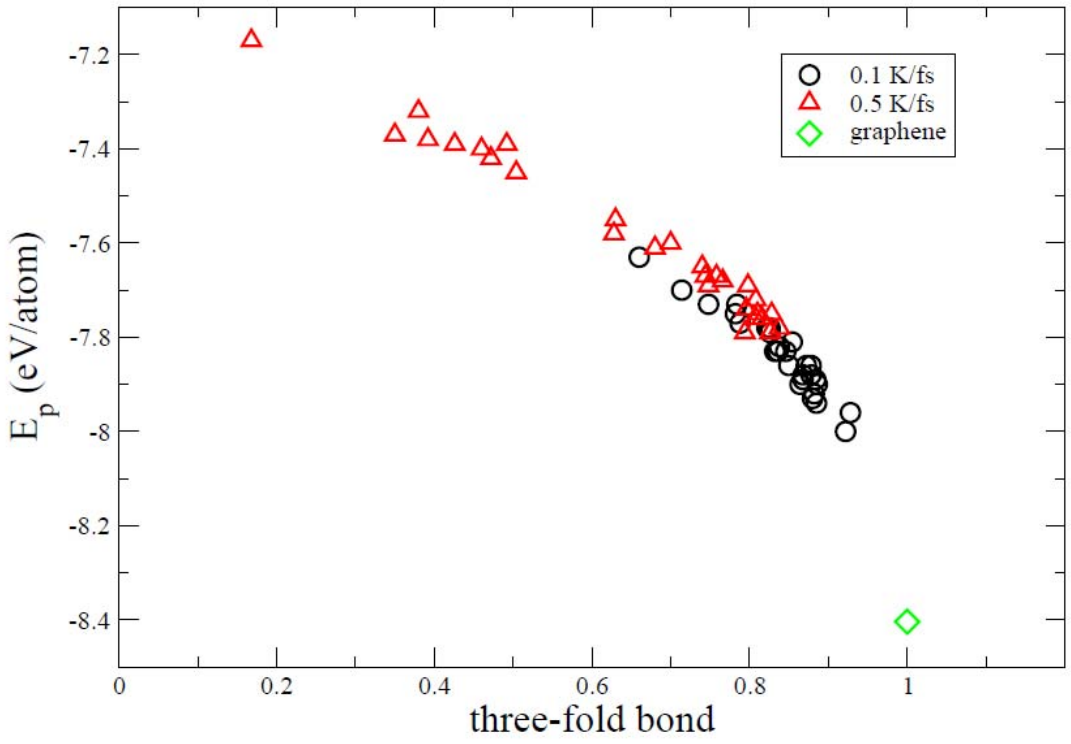

Figure 4.7 The potential energy as a function of fraction of three-fold bonded atoms in the simulations. Results with different quenching rates of 0.1 K/fs (black circles) and 0.5 K/fs (red triangles) are compared. Potential energy of graphene (green diamond) is plotted as reference.

To better characterize the amorphous carbon structures and compare with experiments, we analyzed the pore size distribution function as well as pore connectivity. The pore size distribution functions were calculated following the definition of Gelb and Gubbins.[61] The simulation box was divided into a 50×50×50 grid and a hydrogen molecule was used as a "test particle". For each grid element, the potential energy between hydrogen molecule and carbon atom was calculated using equation (3.7). The volume of grid elements with negative potential energies was attributed to the largest spherical pore that contains the grid elements. Our work on the expanded graphite model (Figure 3.1 in Chapter III) indicates that the effective distance between the position of zero adsorption potential and the center of carbon atom on the pore wall is approximately 2.5 Å. Therefore, in the current calculation of pore size distribution, the radius of a spherical pore was accordingly extended by 2.5 Å after counting the volume of the grid elements. We have plotted the average pore size distribution function for carbon structures with bulk density of 1.8 g/cm^3 in Figure 4.8. For pores smaller than 10 Å, the calculated pore size distribution function is reasonably consistent with that obtained from UMC by N_2 and CO_2 adsorption. Due to the fact that the simulation unit cell is less than 20 Å, pores with radii larger than 10 Å are not observed in our simulations.

(a)

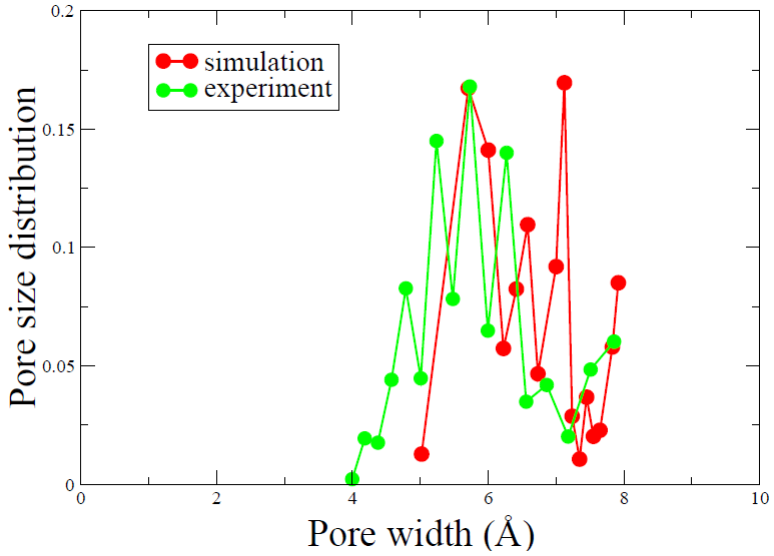

(b)

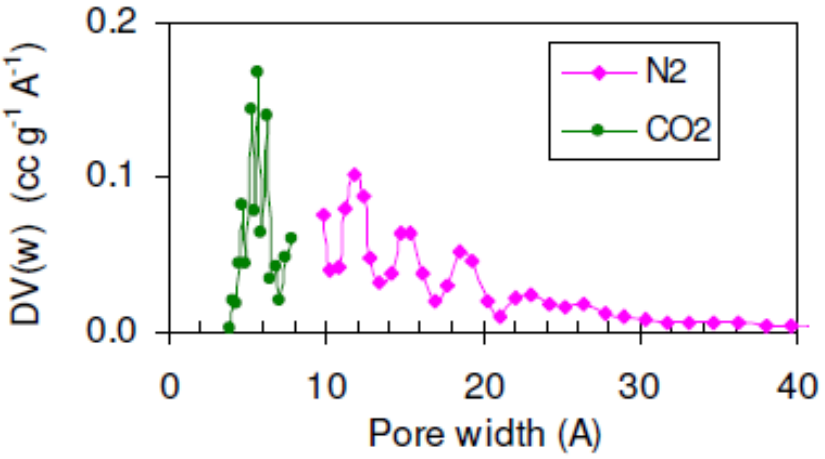

Figure 4.8 (a) Pore size distribution function of simulated structures with bulk density of 1.8g/cm3(red) compared experimental measurement of UMC [53]. (b) Full data set of pore size distribution function of UMC from CO_2 and N_2 adsorption. [53]

The pore connectivity is very important to the kinetics of gas adsorption and desorption. It is analyzed by calculating the number of isolated pores in the structures. Simply: if two grid elements are nearest neighbors, they are considered to belong to the same pore. Figure 4.9 (a) illustrates isolated pores in a simulated carbon network by different colors. The carbon atoms and C-C bonds are also shown. Figure 4.9 (b) plots the average number of isolated pores as a function of carbon bulk density for two different quench rates. A lower quenching rate creates more connected pore structures. For the lower carbon bulk densities, there is only one large pore in the simulated system, indicating possible fast kinetics of gas adsorption/desorption. More isolated pores appear at higher carbon bulk densities. Eventually, the number of isolated pores decreases at high bulk density since the amount of available adsorption volume decreases quickly. It should be noted that our simulations size is limited to 500 atoms. More isolated pores are expected in larger simulation systems.

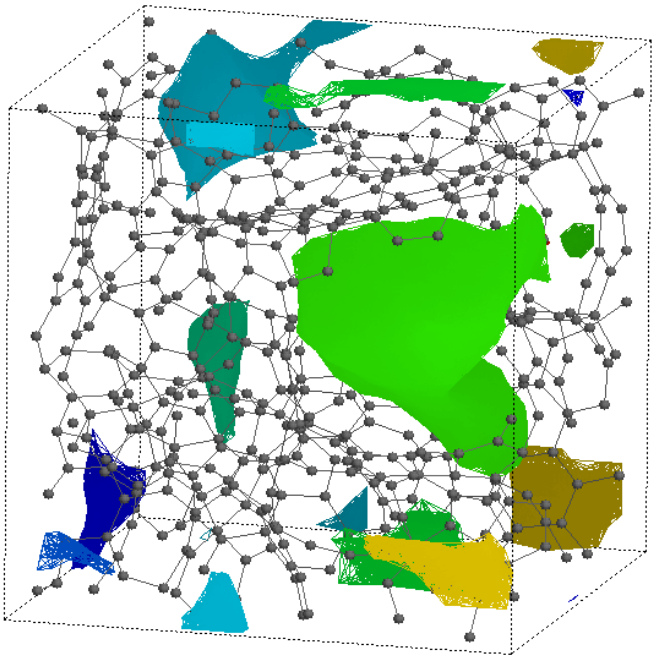

(a)

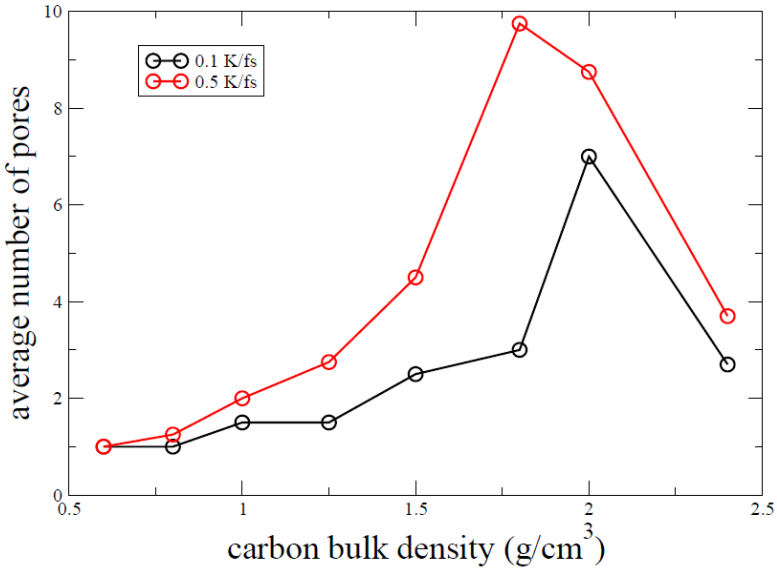

(b)

Figure 4.9 (a) Illustration of isolated pores in amorphous carbon structures. (b) Average number of isolated pores as a function of carbon bulk density with different quenching rates (black: 0.1K/fs; red: 0.5 K/fs).

Finally, we discuss the skeletal density of amorphous carbons. This concept is important for linking experiments with theoretical calculations, but has been ignored by most previous simulation studies. This is also useful for examining the volume available for adsorption. In most simulation studies, the carbon density is simply calculated by the atomic mass and the volume of the unit cell, and referred as bulk density in our paper. In experiments, the density of samples is typically measured utilizing helium adsorption and only refers to the solid volume that is not accessible by helium gas. This experimental density is usually referred as skeletal density. For a close comparison with experimental data, the difference between bulk density and skeletal density should be considered, especially for low density amorphous carbons with large voids and pores. Again, we have used hydrogen molecule to estimate the skeletal density for the simulated nanoporous carbon structures. We define the volume inaccessible to hydrogen gas as the volume with positive (unfavorable) adsorption energies. Thus, the total mass of carbon atoms and the volume inaccessible to hydrogen are used for skeletal density calculations. Figure 4.10 shows that the corresponding skeletal density deviates from the bulk density below 1.8 g/cm^3. Lower quenching rates tend to generate more available adsorption volume, and thus higher skeletal density. The skeletal densities are close to 1.0 g/cm^3 in the low bulk density limit. This is consistent with experimental results since amorphous carbons with skeletal density lower than 1.0 g/cm^3 are rarely reported in experiments. Our earlier discussion of potential energy (Figure 4.6) implies that the stable structure for low density carbons tends to form dense areas and voids. Figure 4.10 further supports this argument.

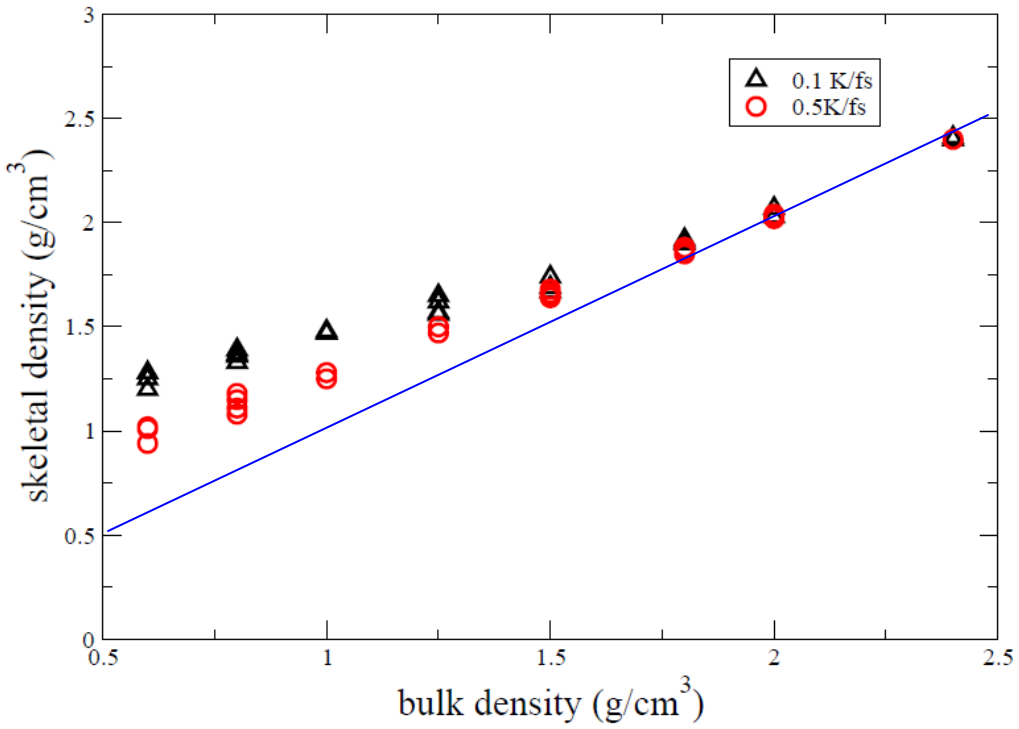

Figure 4.10 Skeletal density as a function of bulk density with different quenching rates (black triangles: 0.1K/fs; red circles: 0.5K/fs). The straight line indicates the relationship if the two densities were identical.

4.3 Conclusion

In summary, we have 1) developed high performance tight binding molecular dynamics simulation program for pure carbon system; 2) systematically studied the structures of amorphous carbons with low densities by using tight binding molecular dynamics simulations. Fragments of graphene sheets are found in the amorphous carbon structures. In particular, parallel graphene sheets are observed higher bulk densities, consistent with the microstructures of activated carbons. The simulations are reasonably consistent with both the experimental pore size distribution and pair distribution function. We also characterize the simulated amorphous carbons by bonding distribution, pore connectivity, potential energy, and skeletal density.

CHAPTER V

HYDROGEN ADSORPTION IN AMORPHOUS CARBONS

Hydrogen adsorption in carbon materials has been widely investigated by simulations and theoretical calculations. Most of the studies are limited to simple carbon structures such as the expanded graphite model,[45, 74, 127] single and multiple walls carbon nanotubes,[91, 128] and doped graphene sheets.[39, 129] Direct simulation or calculation of hydrogen adsorption in realistic amorphous carbon structures is difficult due to the lack of a realistic carbon model and the computational challenge of adsorption calculations in complex geometries. Our work in Chapter III constructs amorphous carbon structures using the empirical Tersoff potential and predicted the hydrogen uptake close to 0.5 wt% at 298K and 5 MPa. The Tersoff potential is convenient for modeling covalently bonded systems due to its simple, analytical forms and short range of atomic interactions. Two- and three-body interactions are considered for the local environment dependency of bond strength. However, as shown in Chapter IV, the Tersoff potential has some unrealistic aspects. For example, it slightly favors diamond structure over graphite structure. Moreover, due to the lack of higher-order interactions, Tersoff potential can not identify the energy difference between structures with the same amount of three folded bonds and different topologies. For example, our previous calculations showed that Tersoff potential tended

to predict more three dimensional amorphous networks rather than flat graphene sheets in low density carbons, due to the lack of torsional effects in the potential (but present in double-bonded carbon). As a result, it is not particularly accurate for modeling amorphous carbon in the low density regime. In this chapter, the theoretical maximum hydrogen uptake is calculated by the continuum adsorption method in the more realistic amorphous carbon models developed by tight binding molecular simulations in Chapter IV. To our knowledge, this is the first work to predict hydrogen adsorption in realistic amorphous carbon at room temperature.

Figure 5.1 shows the simulated carbon structure (gray) with a density of 1.25 g/cm^3. The positions with local adsorption energies lower than -0.1 eV/molecule are shown in the same figure and colored by the adsorption energy from red (low value, most favorable adsorption sites) to blue (high value). The adsorption energy is calculated using the Patchkovskii potential (Eq. 3.6). Figure 5.1 demonstrates that hydrogen molecules are likely to aggregate in narrow pores. This is consistent with the recent small angle neutron scattering (SANS) results on hydrogen adsorption in activated carbons.[130] The density of adsorbed hydrogen, measured by SANS in activated carbons, was much higher than the bulk-phase density, approaching the density of liquid H_2. The gas densification was larger in narrower pores than in larger pores.

Figure 5.2 summarizes the hydrogen adsorption results in simulated carbons at 298K and 5 MPa showing the total uptake, available adsorption volume, excess uptake, and the isosteric heat of adsorption at zero uptake limit as functions of the carbon bulk density.

The available adsorption volume is defined as the total volume of grid elements with a negative adsorption energy for H_2. Similar to our previous results in Tersoff generated carbons (Chapter III), the total hydrogen mass uptake and the available adsorption volume decrease as the carbon bulk density increases. The average total gas uptake ranges from 1.42 wt% in carbon density of 0.6 g/cm^3 to 0.006 wt% in 2.4 g/cm^3, much higher than our previous results for Tersoff generated carbon structures. Figure 5.2 (c) shows the that hydrogen total uptake is correlated with the available adsorption volume, consistent with previous theoretical calculations.[33] Note that all pores in the simulated structures are micropores, in which the adsorption energy is strong throughout each pore. Thus, increasing the volume of *micropores* increases the total gas uptake. The carbon structures generated with a lower quenching rate have higher available volume, thus better hydrogen uptake capacities. Experimentally, larger pores may form, and much larger forms will not significantly increase the adsorption due to weak adsorption away from the pore walls.

Figure 5.2 (d) plots the excess uptake, the difference between the total H_2 in the system minus the amount that would occupy the same available volume without considering the adsorption energy. The peak excess uptake (1.33 wt%) appears at the bulk density of 0.8 g/cm^3. Unlike the total gas uptake, the excess uptake has a maximum for carbon densities near 0.8 g/cm^3, for the lower quenching rate. Very large voids that form in low density carbon structures (Figure 4.1) do not contribute significantly to the excess uptake because the hydrogen molecules in the center of large pores are mainly compressed by high external pressure instead of adsorbed by the potential energy of the pore walls. Thus,

the peak excess adsorption is determined by a balance between having large available volumes and maintaining a significant heat of adsorption. The isosteric heat of adsorption (q_{st}) in the zero uptake limit is calculated by the Clausius-Clapeyron equation (Eq. 3.9) using the Mills EOS (Eq. 3.5). Figure 5.2 (e) shows that the average magnitude of isosteric heat of adsorption ranges from 12 kJ/mol to 22 kJ/mol. This range overlaps the suitable adsorption energy range for hydrogen storage (15-40 kJ/mol). Error bars in Figure 5.2(e) indicate the data spread between different simulations. No significant quenching rate effects on the isosteric heat of adsorption are observed. The value of average isosteric heat of adsorption is shown to increase as carbon bulk density increases. Comparing the excess uptake (Figure 5.2 (d)) with the isosteric heat of adsorption (Figure 5.2(e)), it is clear that increasing the isosteric heat of adsorption does not necessarily increase the hydrogen excess uptake at room temperature, which contradicts normal assumptions. It further reveals the competition between optimizing the available adsorption volume and optimizing the adsorption potential for high gas uptake.

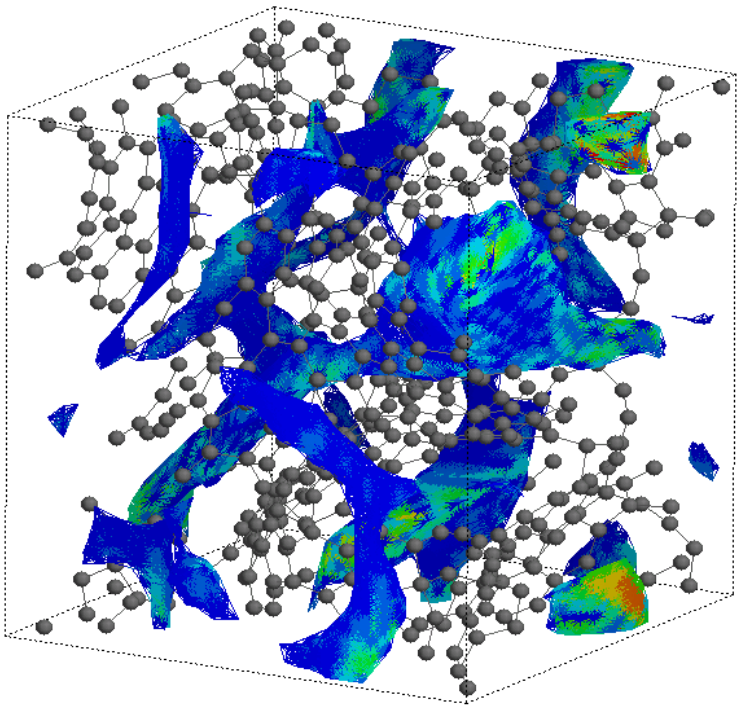

Figure 5.1 Demonstration of adsorption sites in amorphous carbon structures. The gray dots are carbon atoms. The colored areas are the positions with adsorption energy less than 0 eV/H_2. Blue color means weaker adsorption, red color means stronger adsorption.

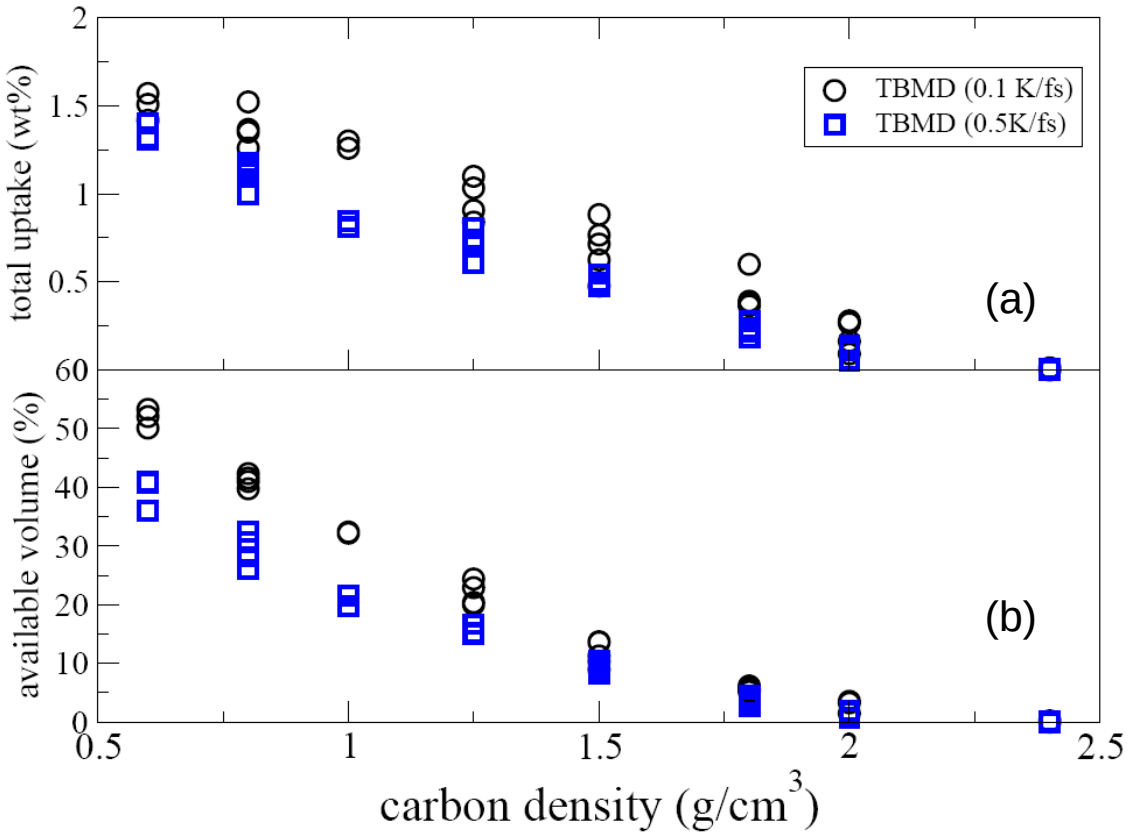

Figure 5.2 (a) Total hydrogen uptake, (b) available adsorption volume, and (d) excess adsorption as a function of carbon bulk density at T=298K and P=5MPa. (c) Total hydrogen uptake as function of available adsorption volume. (e) Average isosteric heat of adsorption at zero adsorption limit as a function of carbon bulk density. The error bar indicates the spread of data in different simulations.

(c)

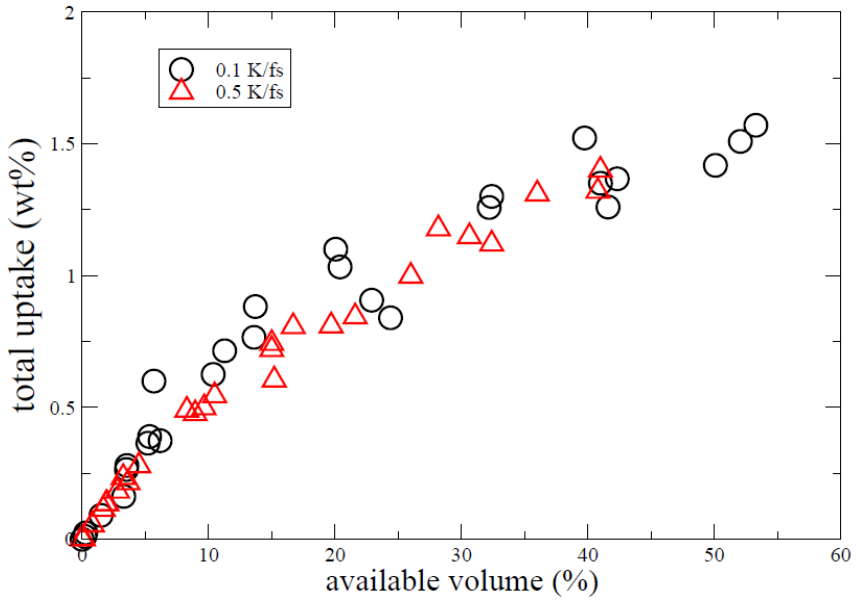

(d)

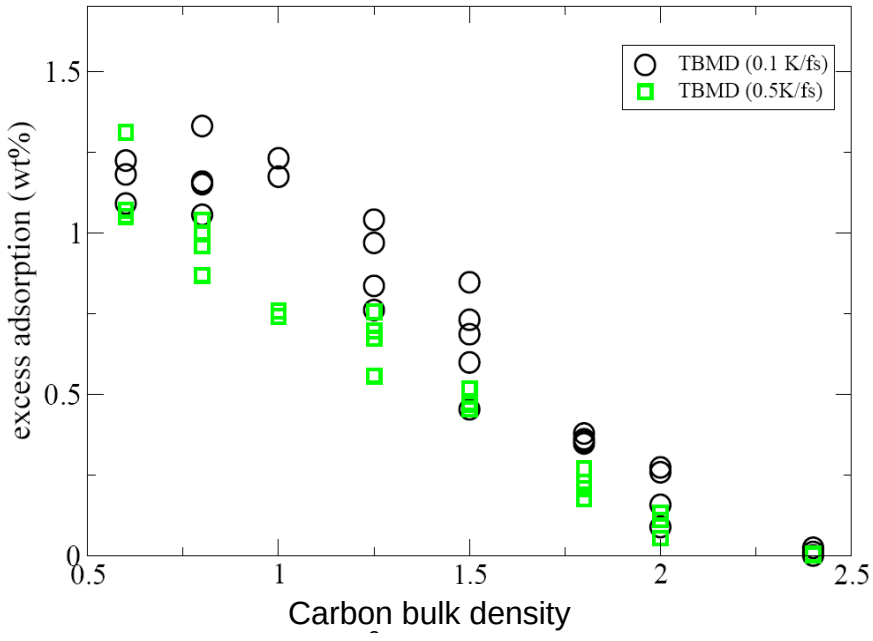

Figure 5.2 (continued)

(e)

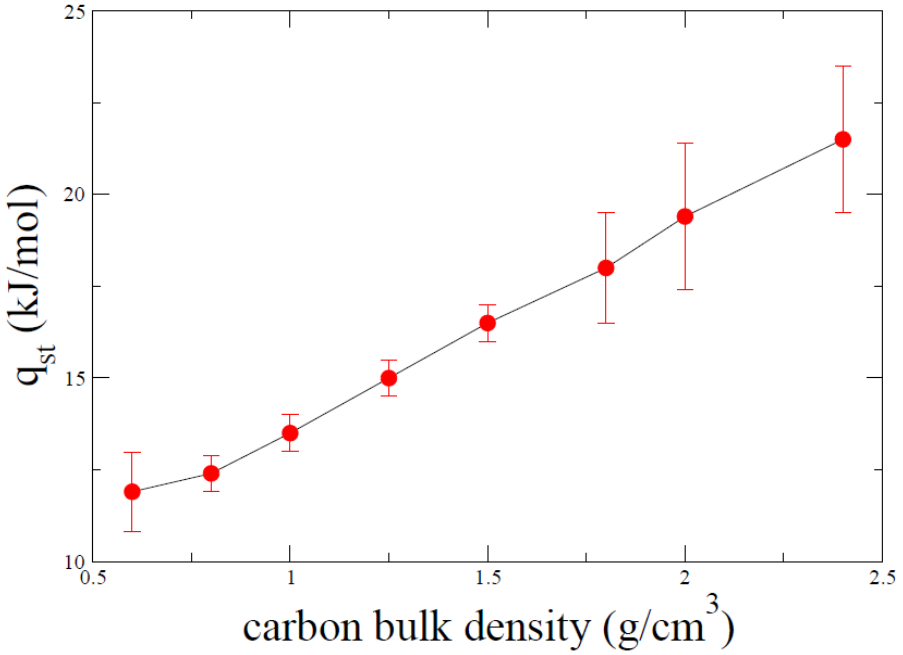

Figure 5.2 (continued)

As discussed in Chapter III, the validity range for the Mills EOS is 2<P<20 kbar and 75<T<307 K. Beyond this validity range, a better EOS should be applied. In Chapter III, we have discussed that the Mills EOS merges into the Kammerlingh-Onnes empirical EOS below 1000 bar and the ideal gas EOS at much lower pressures. Therefore, it is reasonable to extend the usage of the Mills EOS below 2000 bar at room temperature. For internal pressures higher than 20 kbar, the Mills EOS is still used in our current calculations but the uncertainty in adsorbed gas amount must be carefully estimated. On the other hand, quantum effects will be significant at low temperature, and should not be ignored in small confined space where the adsorption energy is usually strong. To take quantum effects into account, Wang and Johnson[73] used a path integral hybrid Monte Carlo method to calculate hydrogen adsorption at low temperature. They attributed the difference between quantum and classical calculations to the larger effective diameter of quantum molecules, similar to arguments presented here and summarized in Figure 3.10. Further investigations in single wall carbon nanotubes[74] demonstrate that the quantum effects were important even at 298K for hydrogen adsorption in nanotube interstices where the adsorption energy is strong. To estimate the error due to the quantum effects in our classical treatment, the thermal de Broglie density was considered in Chapter III. If the adsorbed density is much lower than the thermal de Broglie density, and the pore size much larger than the thermal de Broglie length, then quantum effects are not significant. Especially, for internal pressures less than 20 kbar, the quantum effects can be ignored at room temperature.

Thus, the simplest way to estimate the error bound of adsorption calculations is to calculate the amount of hydrogen gas adsorbed by the internal pressures higher than 20 kbar. This amount of hydrogen is inaccurate due to the invalid range of EOS and the quantum effects. The ratio of this "inaccurate" amount of gas to the total amount of hydrogen adsorbed is referred as the uncertainty in the adsorption calculation. According to the analysis, the uncertainty is less than 10% for carbon structures with density lower than 1.5 g/cm^3. At the optimal carbon density for adsorption, the resulting excess uptake in amorphous carbon is therefore in the range of 1.2 wt% to 1.46 wt%. For a carbon density of 1.5 g/cm^3, the uncertainty is about 15% since the adsorption energy is stronger and internal pressure is much higher in these structures. The uncertainty can be over 50% for carbon densities larger than 1.5 g/cm^3, where the excess uptakes are essentially low (<0.3 wt%) and most of the uptake is in small, concentrated volumes. Another method is to calculate the density of H_2 gas equal to the value at 20 kbar, whenever the internal pressure is over 20 kbar. This is essentially a lower bound to the adsorption. Compared to the first method, this method provides narrower error bars, especially for the structures with very high internal pressures. The lower limit of uptake for carbon structures with density of 0.6 -1.5 g/cm^3 is higher than 95% of the total uptake. For structures with densities between 1.8 and 2.0 g/cm^3, the lower limit is higher than 85% of the total uptake. For carbon structures with densities of 2.4 g/cm^3, the internal pressure is much higher than 20 kbar, thus the error is still large. Its lower bound is less than 80% of the total uptake. Also, bear in mind that the above estimations are based on the assumption that the adsorption energy is accurate. As seen from Chapter III, changes in the adsorption energy dramatically affect the gas uptake (particularly the excess uptake) and

errors in the H_2-C interaction will likely cause much larger errors in the gas adsorption than those due to ignoring quantum effects or inaccuracies in the EOS.

In summary, this chapter examines the hydrogen adsorption in tight-binding generated amorphous carbon structures at room temperature. The theoretical excess hydrogen uptake is found to reach 1.33 wt% in carbon structures with bulk densities of 0.8 g/cm^3 at 298K and 5 MPa. The isosteric heat of adsorption is calculated to be between 12.5 kJ/mol and 21 kJ/mol, suggesting that amorphous carbon is promising for hydrogen storage. Hydrogen uptake is determined by both the micropore volume as well as the isosteric heat of adsorption. Especially, increasing the isosteric heat of adsorption does not necessary increases the hydrogen uptake. In this chapter, we utilized the Patchkovskii et al. C-H_2 interaction potential, based on their fitting of quantum chemical calculations of the H_2-coronene interactions. The hydrogen uptake and isosteric heat of adsorption are very sensitive to C-H_2 interaction potential. More accurate interaction models, containing long distance dispersion forces, will be considered in further research. The simulations show that a lower quenching rate generates lower energy carbons with more graphite-like structures, which favors higher hydrogen adsorption.

CHAPTER VI

SUMMARY AND FUTURE WORK

In this dissertation, we have investigated the structural and gas adsorption properties of amorphous carbons, in order to theoretically probe the hydrogen storage capacity of nanoporous carbon materials. The amorphous carbon structures are prepared by quenching molecular dynamics simulations, primarily using a semiempirical tight binding model. To simulate the activated carbons which are widely used in hydrogen adsorption experiments, low carbon densities ranging from 0.6 – 2.4 g/cm^3 have been studied in the simulations. Careful analyses have been carried on the pair distribution function G(r), bonding distribution, pore size distribution function, pore connectivity, skeletal density, and microstructure at atomic level. The resulting structures compare well with experiments on wood-based activated carbons and with previous simulation results from more accurate *ab inito* calculations. It is shown that low density amorphous carbons consist of curved, defective graphene sheets. Especially, parallel graphene sheets are observed in our simulations, consistent with the high resolution microscopic images of activated carbons. We have also seen the third peak in G(r) which is a common feature observed in activated carbons but was absent in most previous tight binding calculations.

To estimate the hydrogen adsorption at room temperature, we introduce an efficient numerical method capable of rapidly treating complex adsorbent structures. We demonstrate the accuracy of this method in an expanded graphite model, and further apply it to the amorphous carbon structures. The theoretical optimum excess adsorption of amorphous carbon is calculated to be close to 1.33 wt% at room temperature and 5 MPa. Pore sizes close to 7 Å are considered best for hydrogen storage in carbon materials at room temperature, which suggests a direction of future materials design. The calculated isosteric heat of adsorption in amorphous carbon is between 12-21 kJ/mol, overlapping with the required energy range for hydrogen storage (15-40 kJ/mol). Our results reveal that increasing the heat of adsorption does not necessarily increase the hydrogen uptake. In fact, the available adsorption volume is as important as the isosteric heat of adsorption for hydrogen storage in microporous carbons. Our work, for the first time, predicts the hydrogen adsorption capacity in amorphous carbon, and reveals the potential of carbon materials for hydrogen storage.

There are still many interesting challenges and opportunities for the future research. One of the initial goals of this project is to establish realistic atomic models for amorphous carbon materials. The current state of simulation studies is still limited due to the computational power, such as small simulation size scale, short simulation time scale, simple quenching model, and the lack of hydrocarbon precursors. High resolution transmission electron microscopy (HRTEM) revealed that the basic structural unit of activated carbons consisted of stacked parallel graphene sheets with length scale close to 1 nm in planar direction.[51] Our current simulations have observed similar graphene

sheets in amorphous carbons. However, to study the correlation between the basic structural units at intermediate range, the simulation length scale should be much larger than 1 nm, which is still a large computational challenge for current tight binding molecular simulations. Simulations containing thousands of atoms with the unit box size up to several nanometers have only been performed by the empirical potentials with less accuracy.[29, 60, 114] Modeling the wide range of pore size distribution in the activated carbons is difficult by using small simulation sizes. Another challenge for mimicking activated carbon production is the short time scale (~ 10^{-10} s) affordable to current computational capacities. The simulation quenching rate, which usually ranges between 10^{12} to10^{15} K/s due to the short simulation time scale, is impossibly high for experiments. As shown in this dissertation, the quenching rate has significant effects on many aspects of amorphous carbon ranging from energy, bonding structures, pore size distribution and adsorption properties. Moreover, the quenching molecular dynamics method used in the dissertation is the simplest method to generate amorphous configurations. It ignores the importance of organic precursors in the activated carbon productions, and the various synthesis methods used in preparing activated carbons. Instead, it uses the highly random structures from liquid carbon as the initial structure of the simulations. In fact, the microstructures of activated carbon have been shown heavily related to the heat treatment temperature and the nature of precursors.[51, 131-133] Therefore, future research will focus on building further optimized simulation programs and utilizing the advanced computer facilities (Franklin at NERSC and Kraken at ORNL) to provide larger size simulations which contain hydrocarbon reactions with lower quenching rates. Other than molecular dynamics simulation, there are still many different methods to generate amorphous

carbons which have been reviewed in Chapter II. Reverse Monte Carlo (RMC) simulation is another important method for constructing amorphous carbon structures. However, by fitting the experimental structure factor, reverse Monte Carlo methods largely depend on the experimental input, initial simulation structures and the system density. Despite the wide use of RMC in low density amorphous carbons, a large portion of 2-fold bonded atoms were reported in the simulated structures, indicating very high structural energies.

Small angle neutron scattering (SANS) is a powerful technique to study the pore structure and pore size distribution of amorphous carbons. The behaviors of confined fluids in variable pore sizes including the density and volume can be also revealed by SANS. Recent high pressure in-situ SANS experiments[123] reported the hydrogen densification as a function of pore size in nanoporous carbons at room temperature. The adsorbed hydrogen phase density was reported to be about 30-60 times higher than the bulk phase density at relatively low laboratory pressures, indicating the carbon material acts as an efficient gas pump in the adsorption process. Our theoretical work on hydrogen adsorption in nanoporous carbons will provide a natural comparison and support for the SANS experiments. Direct information of pore size distribution and hydrogen density profile can be obtained from our simulations. In contrast, the scattering experiments obtain the real space information by Fourier transformation of Q space, and might lack important information. For example, the pore size is roughly estimated by $2\pi/q$ in SANS experiments, where q is the scattering vector. This is a rough estimate, and a direct comparison with a real space hydrogen profile would be useful. Our simulation results

can also be directly compared with scattering data by using the real space carbon and hydrogen positions to calculate the scattering intensity. The future work on the comparison with SANS will be a great test for our current carbon structure and gas adsorption models.

Another challenge for the material design for hydrogen storage is the accuracy of the interaction potential between hydrogen and carbon materials. An accurate description of van der Waals interaction between hydrogen and carbon is very important for a good estimation of adsorption. Most empirical potentials are fitted to quantum chemistry calculations or to experimental results. Despite many successful applications in solid state physics and chemistry, density functional theory (DFT) still has difficulties to properly describe dispersive, nonlocal correlation effects. The results from DFT are not reliable for systems where van der Waals interactions are important. For example, the generalized density-gradient approximation (GGA) calculations fail to predict the interlayer distance of graphite.[134] The local density approximation (LDA) calculations provide the right interlayer distance but largely underestimate the interlayer cohesive energy.[135] Recently, methods have been developed to include long-range dispersive van der Waals interaction into density function theory. Cooper has proposed an exchange functional for vdW-DF which offers better agreement on the graphite interlayer distance and cohesive energy with experiments compared to other methods.[136] This work provides a more accurate first principle calculation of the van der Waals interaction between carbon and hydrogen molecule. We have initiated collaboration with Cooper to

provide more accurate evaluation of the hydrogen adsorption in carbon materials, and to develop more accurate descriptions of interactions.

Hydrogen applications in automobiles require not only high hydrogen adsorption capacity but also good reversibility with quick kinetics. The reversible adsorption in carbon nanoporous materials may be much lower than the theoretical maximum uptake due to the existence of isolated pores and slow diffusion rate of hydrogen molecules. In future studies, we will probe the kinetics of hydrogen in nanoporous carbons, with the goal of aiding the design of materials with high uptake and good adsorption/desorption rate. Diffusion occurs in order to lower the free energy. Accordingly, the diffusion equations must predict a static density when conditions satisfy thermodynamic equilibrium: the chemical potential must be the same through the system. The flux of the particles transported across unit area per second thus is related to the gradient of chemical potential, the atomic concentration, and the atomic mobility (or diffusion coefficient). The chemical potential of adsorbed hydrogen can be mapped out through the adsorption potential energies and the densities of the adsorbed hydrogen molecules. With the diffusion rate, we can predict the flux of hydrogen and relate this to the kinetics of adsorption (uptake vs. time) for specific carbon structures at constant T and P. Important parameters determining the adsorption rate include the pore connectivity and energy barriers between pores. We will characterize the effects of nanostructures to adsorption kinetics.

Gas adsorption/desorption not only can be controlled by changing temperature and pressure but also by other factors such as external electric field. Zhou et al.[137] proposed to tune the hydrogen adsorption energy on a graphene-like hexagonal BN sheet by changing the electric field. The induced dipole moment of hydrogen molecule was changed linearly with the electric field and the binding energy was reported up to 0.14 eV/H_2. Even though the electric field required in their calculations is very high, the same idea can be applied to graphene sheet and other carbon materials to improve the kinetic and uptake of hydrogen storage. Future cooperation with the authors in Ref.[137] will pay special attention on functionalized carbon materials which might couple the structural curvature with lower electric field to greatly enhance the binding energy between H_2 and carbon.

LIST OF REFERENCES

[1] S. Patchkovskii, J. S. Tse, S. N. Yurchenko, L. Zhechkov, T. Heine, and G. Seifert, *P Natl Acad Sci USA* **102**, 10439 (2005).
[2] B. Bogdanovic and M. Schwickardi, *J Alloy Compd* **253**, 1 (1997).
[3] S.-i. Orimo, Y. Nakamori, J. R. Eliseo, A. Züttel, and C. M. Jensen, *Chemical Reviews* **107**, 4111 (2007).
[4] B. Bogdanovic and G. Sandrock, *Mrs Bulletin* **27**, 712 (2002).
[5] C. P. Baldé, B. P. C. Hereijgers, J. H. Bitter, and K. P. de Jong, *J Am Chem Soc* **130**, 6761 (2008).
[6] D. Fraenkel and J. Shabtai, *J Am Chem Soc* **99**, 7074 (1977).
[7] J. Dong, X. Wang, H. Xu, Q. Zhao, and J. Li, *Int J Hydrogen Energ* **32**, 4998 (2007).
[8] K.-H. Chung, *Energy* **35**, 2235 (2010).
[9] C. Otero Areán, G. Turnes Palomino, and M. R. Llop Carayol, *Appl Surf Sci* **253**, 5701 (2007).
[10] M. Eddaoudi, J. Kim, N. Rosi, D. Vodak, J. Wachter, M. O'Keeffe, and O. M. Yaghi, *Science* **295**, 469 (2002).
[11] H. Furukawa, et al., *Science* **329**, 424 (2010).
[12] N. L. Rosi, J. Eckert, M. Eddaoudi, D. T. Vodak, J. Kim, M. O'Keeffe, and O. M. Yaghi, *Science* **300**, 1127 (2003).
[13] S. S. Kaye, A. Dailly, O. M. Yaghi, and J. R. Long, *J Am Chem Soc* **129**, 14176 (2007).
[14] Q. Yang and C. Zhong, *The Journal of Physical Chemistry B* **109**, 11862 (2005).
[15] T. Sagara, J. Klassen, and E. Ganz, *Journal of Chemical Physics* **121**, 12543 (2004).
[16] T. Yildirim and M. R. Hartman, *Physical Review Letters* **95**, 215504 (2005).
[17] M. Dincă and J. R. Long, *Angewandte Chemie International Edition* **47**, 6766 (2008).
[18] T. Sagara, J. Klassen, J. Ortony, and E. Ganz, *Journal of Chemical Physics* **123** (2005).
[19] M. Dincă, A. Dailly, Y. Liu, C. M. Brown, D. A. Neumann, and J. R. Long, *J Am Chem Soc* **128**, 16876 (2006).
[20] B. Chen, X. Zhao, A. Putkham, K. Hong, E. B. Lobkovsky, E. J. Hurtado, A. J. Fletcher, and K. M. Thomas, *J Am Chem Soc* **130**, 6411 (2008).
[21] L. J. Murray, M. Dinca, and J. R. Long, *Chem Soc Rev* **38**, 1294 (2009).
[22] A. Chambers, C. Park, R. T. K. Baker, and N. M. Rodriguez, *J Phys Chem B* **102**, 4253 (1998).
[23] P. Chen, X. Wu, J. Lin, and K. L. Tan, *Science* **285**, 91 (1999).
[24] C. Liu, Y. Y. Fan, M. Liu, H. T. Cong, H. M. Cheng, and M. S. Dresselhaus, *Science* **286**, 1127 (1999).
[25] A. C. Dillon, K. M. Jones, T. A. Bekkedahl, C. H. Kiang, D. S. Bethune, and M. J. Heben, *Nature* **386**, 377 (1997).
[26] A. C. Dillon and M. J. Heben, *Appl Phys a-Mater* **72**, 133 (2001).
[27] W. C. Xu, K. Takahashi, Y. Matsuo, Y. Hattori, M. Kumagai, S. Ishiyama, K. Kaneko, and S. Iijima, *Int J Hydrogen Energ* **32**, 2504 (2007).

[28] R. S. Aga, C. L. Fu, M. Krcmar, and J. R. Morris, *Phys Rev B* **76**, 165404 (2007).
[29] L. J. Peng and J. R. Morris, *J Phys Chem C* **114**, 15522 (2010).
[30] Q. Wang and J. K. Johnson, *Journal of Chemical Physics* **110**, 577 (1999).
[31] A. Zuttel, P. Sudan, P. Mauron, T. Kiyobayashi, C. Emmenegger, and L. Schlapbach, *International Journal of Hydrogen Energy* **27**, 203 (2002).
[32] G. Stan and M. W. Cole, *Journal of Low Temperature Physics* **110**, 539 (1998).
[33] R. Strobel, J. Garche, P. T. Moseley, L. Jorissen, and G. Wolf, *J Power Sources* **159**, 781 (2006).
[34] A. Cao, H. Zhu, X. Zhang, X. Li, D. Ruan, C. Xu, B. Wei, J. Liang, and D. Wu, *Chem Phys Lett* **342**, 510 (2001).
[35] W. C. Xu, K. Takahashi, Y. Matsuo, Y. Hattori, M. Kumagai, S. Ishiyama, K. Kaneko, and S. Iijima, *Int J Hydrogen Energ* **32**, 2504 (2007).
[36] Y. Ye, C. C. Ahn, C. Witham, B. Fultz, J. Liu, A. G. Rinzler, D. Colbert, K. A. Smith, and R. E. Smalley, *Appl Phys Lett* **74**, 2307 (1999).
[37] G. Q. Ning, F. Wei, G. H. Luo, Q. X. Wang, Y. L. Wu, and H. Yu, *Applied Physics A: Materials Science & Processing* **78**, 955 (2004).
[38] P. Kowalczyk, R. Holyst, M. Terrones, and H. Terrones, *Phys Chem Chem Phys* **9**, 1786 (2007).
[39] W. Q. Deng, X. Xu, and W. A. Goddard, *Physical Review Letters* **92**, 166103 (2004).
[40] G. K. Dimitrakakis, E. Tylianakis, and G. E. Froudakis, *Nano Lett* **8**, 3166 (2008).
[41] A. A. Peera, L. B. Alemany, and W. E. Billups, *Appl Phys a-Mater* **78**, 995 (2004).
[42] K. Komatsu, M. Murata, and Y. Murata, *Science* **307**, 238 (2005).
[43] N. Texier-Mandoki, J. Dentzer, T. Piquero, S. Saadallah, P. David, and C. Vix-Guterl, *Carbon* **42**, 2744 (2004).
[44] L. Zhou, Y. P. Zhou, and Y. Sun, *Int J Hydrogen Energ* **29**, 319 (2004).
[45] M. Rzepka, P. Lamp, and M. A. de la Casa-Lillo, *The Journal of Physical Chemistry B* **102**, 10894 (1998).
[46] M. Jorda-Beneyto, F. Suarez-Garcia, D. Lozano-Castello, D. Cazorla-Amoros, and A. Linares-Solano, *Carbon* **45**, 293 (2007).
[47] J. Burress, M. Kraus, M. Beckner, R. Cepel, G. Suppes, C. Wexler, and P. Pfeifer, *Nanotechnology* **20** (2009).
[48] V. V. Bhat, C. I. Contescu, N. C. Gallego, and F. S. Baker, *Carbon* **48**, 1331 (2010).
[49] P. J. F. Harris and et al., *Journal of Physics: Condensed Matter* **20**, 362201 (2008).
[50] R. Dash, J. Chmiola, G. Yushin, Y. Gogotsi, G. Laudisio, J. Singer, J. Fischer, and S. Kucheyev, *Carbon* **44**, 2489 (2006).
[51] T. Hayashi, M. Endo, and M. S. Dresselhaus, *Appl Phys Lett* **77**, 1141 (2000).
[52] U. M. Franklin and W. A. Miller, *Can. Met. Q.* **8**, 145 (1969).
[53] V.V. Bhat, C.I. Contescu, N. C. Gallego, and F. S. Baker, *Carbon* **48**, 1331 (2010).
[54] P. J. F. Harris, *International Materials Reviews* **42**, 206 (1997).
[55] M. A. Smith, H. C. Foley, and R. F. Lobo, *Carbon* **42**, 2041 (2004).

[56] L. N. Bourgeois and L. A. Bursill, *Chem Phys Lett* **277**, 571 (1997).
[57] K. T. Thomson and K. E. Gubbins, *Langmuir* **16**, 5761 (2000).
[58] J. Pikunic, C. Clinard, N. Cohaut, K. E. Gubbins, J. M. Guet, R. J. M. Pellenq, I. Rannou, and J. N. Rouzaud, *Langmuir* **19**, 8565 (2003).
[59] S. K. Jain, R. J. M. Pellenq, J. P. Pikunic, and K. E. Gubbins, *Langmuir* **22**, 9942 (2006).
[60] J. C. Palmer, J. K. Brennan, M. M. Hurley, A. Balboa, and K. E. Gubbins, *Carbon* **47**, 2904 (2009).
[61] L. D. Gelb and K. E. Gubbins, *Langmuir* **15**, 305 (1999).
[62] S. Bhattacharya and K. E. Gubbins, *Journal of Chemical Physics* **123** (2005).
[63] A. Kumar, R. F. Lobo, and N. J. Wagner, *Carbon* **43**, 3099 (2005).
[64] A. P. Horsfield, P. D. Godwin, D. G. Pettifor, and A. P. Sutton, *Phys Rev B* **54**, 15773 (1996).
[65] S. Iarlori, G. Galli, and O. Martini, *Phys Rev B* **49**, 7060 (1994).
[66] J. Houska, J. E. Klemberg-Sapieha, and L. Martinu, *Surface and Coatings Technology* **203**, 3770 (2009).
[67] N. A. Seaton, J. Walton, and N. Quirke, *Carbon* **27**, 853 (1989).
[68] Z. M. Tan and K. E. Gubbins, *Journal of Physical Chemistry* **94**, 6061 (1990).
[69] Z. Tan and K. E. Gubbins, *The Journal of Physical Chemistry* **96**, 845 (1992).
[70] P. Rocken and P. Tarazona, *Journal of Chemical Physics* **105**, 2034 (1996).
[71] M. W. Maddox and K. E. Gubbins, *Langmuir* **11**, 3988 (1995).
[72] A. Gigras, S. K. Bhatia, A. V. A. Kumar, and A. L. Myers, *Carbon* **45**, 1043 (2007).
[73] Q. WANG and J. K. JOHNSON, *Molecular Physics: An International Journal at the Interface Between Chemistry and Physics* **95**, 299 (1998).
[74] J. K. J. Q. Wang, *Journal of Chemical Physics* **110**, 577 (1999).
[75] C. Gu and G.-H. Gao, *Phys Chem Chem Phys* **4**, 4700 (2002).
[76] S. K. Kumar, G. Szamel, and J. F. Douglas, *Journal of Chemical Physics* **124** (2006).
[77] S. Maruyama and T. Kimura, *ASME Internaltional Mechanical Engineering Congress and Exhibit, Orland* (2000).
[78] H. S. Cheng, A. C. Cooper, G. P. Pez, M. K. Kostov, P. Piotrowski, and S. J. Stuart, *J Phys Chem B* **109**, 3780 (2005).
[79] H. Cheng, G. P. Pez, and A. C. Cooper, *J Am Chem Soc* **123**, 5845 (2001).
[80] G. Canto and et al., *New J Phys* **5**, 124 (2003).
[81] H. Cheng, G. Pez, G. Kern, G. Kresse, and J. Hafner, *The Journal of Physical Chemistry B* **105**, 736 (2000).
[82] I. Cabria, M. J. Lopez, and J. A. Alonso, *Carbon* **45**, 2649 (2007).
[83] J. D. Ramshaw, *Journal of Chemical Education* **72**, 601 (1995).
[84] L. Zhou and Y. P. Zhou, *Int J Hydrogen Energ* **26**, 597 (2001).
[85] R. L. Mills, D. H. Liebenberg, J. C. Bronson, and L. C. Schmidt, *J. Chem. Phys.* **66**, 3078 (1977).
[86] M. Benedict, *J Am Chem Soc* **59**, 2233 (1937).
[87] S. C. Wang, L. Senbetu, and C. W. Woo, *Journal of Low Temperature Physics* **41**, 611 (1980).

[88] J. Alcaniz-Monge and M. C. Roman-Martinez, *Micropor Mesopor Mat* **112**, 510 (2008).
[89] S. Beyaz, F. D. Lamari, B. Weinberger, and P. Langlois, *Int J Hydrogen Energ* **35**, 217 (2010).
[90] X. B. Zhao, B. Xiao, A. J. Fletcher, and K. M. Thomas, *J. Phys. Chem. B* **109**, 8880 (2005).
[91] P. Guay, B. L. Stansfield, and A. Rochefort, *Carbon* **42**, 2187 (2004).
[92] J. Tersoff, *Physical Review Letters* **61** (1988).
[93] J. Tersoff, *Phys Rev B* **37**, 6991 (1988).
[94] C. Mathioudakis, G. Kopidakis, P. C. Kelires, C. Z. Wang, and K. M. Ho, *Phys Rev B* **70** (2004).
[95] J. H. Konnert and P. Dantonio, *Carbon* **21**, 193 (1983).
[96] K. Kaneko, C. Ishii, M. Ruike, and H. Kuwabara, *Carbon* **30**, 1075 (1992).
[97] Z. C. Tu and X. Hu, *Phys Rev B* **74**, 035434 (2006).
[98] C. Tusche, H. L. Meyerheim, and J. Kirschner, *Physical Review Letters* **99**, 026102 (2007).
[99] H. Si, L. J. Peng, J. R. Morris, and B. C. Pan, *accepted by the Journal of Chemical Physics* (2011).
[100] P. Ordejon, E. Artacho, and J. M. Soler, *Phys Rev B* **53**, 10441 (1996).
[101] D. SanchezPortal, P. Ordejon, E. Artacho, and J. M. Soler, *Int J Quantum Chem* **65**, 453 (1997).
[102] J. M. Soler, E. Artacho, J. D. Gale, A. Garcia, J. Junquera, P. Ordejan, and D. Sanchez-Portal, *Journal of Physics: Condensed Matter* **14**, 2745 (2002).
[103] N. Troullier and J. L. Martins, *Phys Rev B* **43**, 1993 (1991).
[104] L. Kleinman and D. M. Bylander, *Physical Review Letters* **48**, 1425 (1982).
[105] D. M. Bylander and L. Kleinman, *Phys Rev B* **41**, 907 (1990).
[106] J. P. Perdew and A. Zunger, *Phys Rev B* **23**, 5048 (1981).
[107] J. Albertsson, S. C. Abrahams, and A. Kvick, *Acta Crystallographica Section B-Structural Science* **45**, 34 (1989).
[108] L. Zhechkov, T. Heine, S. Patchkovskii, G. Seifert, and H. A. Duarte, *Journal of Chemical Theory and Computation* **1**, 841 (2005).
[109] A. N. Kolmogorov and V. H. Crespi, *Phys Rev B* **71** (2005).
[110] C. F. Prutton and S. H. Maron, *Fundamental Principles of Physical Chemistry* (1949).
[111] G. Galli, R. M. Martin, R. Car, and M. Parrinello, *Phys Rev B* **42**, 7470 (1990).
[112] D. G. McCulloch, D. R. McKenzie, and C. M. Goringe, *Phys Rev B* **61**, 2349 (2000).
[113] N. A. Marks, D. R. McKenzie, B. A. Pailthorpe, M. Bernasconi, and M. Parrinello, *Phys Rev B* **54**, 9703 (1996).
[114] Y. F. Shi, *Journal of Chemical Physics* **128** (2008).
[115] D. W. Brenner, *Phys Rev B* **42**, 9458 (1990).
[116] C. H. Xu, C. Z. Wang, C. T. Chan, and K. M. Ho, *J Phys-Condens Mat* **4**, 6047 (1992).
[117] B. L. Zhang, C. Z. Wang, C. T. Chan, and K. M. Ho, *Phys Rev B* **48**, 11381 (1993).

[118] C. Z. Wang, K. M. Ho, and C. T. Chan, *Physical Review Letters* **70**, 611 (1993).
[119] C. Z. Wang and K. M. Ho, *Physical Review Letters* **71**, 1184 (1993).
[120] C. Z. Wang, K. M. Ho, and C. T. Chan, *Phys Rev B* **47**, 14835 (1993).
[121] J. R. Morris, C. Z. Wang, and K. M. Ho, *Phys Rev B* **52**, 4138 (1995).
[122] C. Z. Wang, S. Y. Qiu, and K. M. Ho, *Comp Mater Sci* **7**, 315 (1997).
[123] M. Chisholm, C. Contescu, and N. Gallego, *private communication*.
[124] A. Claye and J. E. Fischer, *Electrochim Acta* **45**, 107 (1999).
[125] F. Li and J. S. Lannin, *Physical Review Letters* **65**, 1905 (1990).
[126] W. Dmowski, *Private communication*.
[127] R. F. Cracknell, *Phys Chem Chem Phys* **3**, 2091 (2001).
[128] I. Efremenko and M. Sheintuch, *Langmuir* **21**, 6282 (2005).
[129] Z. M. Ao, Q. Jiang, R. Q. Zhang, T. T. Tan, and S. Li, *J Appl Phys* **105** (2009).
[130] Dipendu Saha, Lilin He, Cristian I. Contescu, Nidia C. Gallego, and Y. B. Melnichenko, *to be submitted to Journal of the American Chemical Society*.
[131] G. Comelli, J. Stohr, C. J. Robinson, and W. Jark, *Phys Rev B* **38**, 7511 (1988).
[132] P. J. F. Harris and et al., *Journal of Physics Conference Series* **241**, 012050 (2010).
[133] S. Urbonaite, S. Wachtmeister, C. Mirguet, E. Coronel, W. Y. Zou, S. Csillag, and G. Svensson, *Carbon* **45**, 2047 (2007).
[134] N. Mounet and N. Marzari, *Phys Rev B* **71**, 205214 (2005).
[135] M. Hasegawa, K. Nishidate, and H. Iyetomi, *Phys Rev B* **76**, 115424 (2007).
[136] V. R. Cooper, *Phys Rev B* **81**, 161104 (2010).
[137] J. Zhou, Q. Wang, Q. Sun, P. Jena, and X. S. Chen, *P Natl Acad Sci USA* **107**, 2801 (2010).

VITA

Lujian Peng was born in Guangxi, China in 1983. She got her Bachelor's degree in 2006, majoring in Applied Physics, from the University of Science and Technology of China, Hefei, China. She enrolled in the graduate program in the Department of Materials Science and Engineering at the University of Tennessee, Knoxville in 2006. She worked on crystal nucleation theory and received her Mater's degree in May 2009. She further received the Doctor of Philosophy degree in Materials Science and Engineering with a minor in Computational Science in May 2011, focusing on hydrogen storage modeling in nanoporous carbons.